Two-way coupled Eulerian-Eulerian finite volume simulation of drifting snow

Ziad, Boutanios

Doctoral thesis / Disertacija

2018

Degree Grantor / Ustanova koja je dodijelila akademski / stručni stupanj: **University of Zagreb, Faculty of Mechanical Engineering and Naval Architecture / Sveučilište u Zagrebu, Fakultet strojarstva i brodogradnje**

Permanent link / Trajna poveznica: https://urn.nsk.hr/urn:nbn:hr:235:198563

Rights / Prava: In copyright/Zaštićeno autorskim pravom.

Download date / Datum preuzimanja: **2025-04-01**

Repository / Repozitorij:

Repository of Faculty of Mechanical Engineering and Naval Architecture University of Zagreb

University of Zagreb

Faculty of Mechanical Engineering and Naval Architecture

Ziad Boutanios

Two-way Coupled Eulerian-Eulerian Finite Volume Simulation of Drifting Snow

DOCTORAL THESIS

Zagreb, 2018.

University of Zagreb

Faculty of Mechanical Engineering and Naval Architecture

Ziad Boutanios

Two-way Coupled Eulerian-Eulerian Finite Volume Simulation of Drifting Snow

DOCTORAL THESIS

Supervisor: prof. Hrvoje Jasak, PhD

Zagreb, 2018.

Sveučilište u Zagrebu

Fakultet strojarstva i brodogradnje

Ziad Boutanios

Dvosmjerno spregnuta Euler-Eulerova simulacija nošenja snijega metodom Kontrolnih Volumena

DOKTORSKI RAD

Mentor: prof. dr. sc. Hrvoje Jasak

Zagreb, 2018.

Acknowledgements

It took a substantial degree of sustained perseverance over three years to bring this academic effort to fruition, all while juggling with an engineering consulting career, and family life, across two continents. My sincere gratitude goes to my supervisor, Prof. Hrvoje Jasak, who welcomed me in his group at the Faculty of Mechanical Engineering and Naval Architecture in Zagreb, allowed me all the latitude needed, and was always available for questions and discussions about the highly unusual CFD and physical aspects of the topic dealt with. I am also very grateful to the members of our group, Prof. Željko Tuković, Gregor Cvijetić, Inno Gatin, Robert Keser, Tessa Uroić, Vanja Škurić, and Vuko Vukčević, who made me feel at home in Zagreb, and provided a wonderful working environment.

Special thanks go to Ms. Izidora Herold, Ms. Matea Klanac, Ms. Zvonka Fofić, and Ms. Nevena Grubelić for providing invaluable administrative support during my studies, without which I would have surely gotten lost in the labyrinthine Croatian bureaucracy.

Last but not least, my utmost love and gratitude go to my family for their unconditional love and support: my father and mother, Menaime and Mary, my sisters, Rita, Ghada, and Majida, my brother in law Charbel, and our youngest, Maya, Yasmine, and Dany. You did not merely hold the fort, you are the fort!

Abstract

An Eulerian-Eulerian two-way coupled model for simulating drifting snow, and solid particle-laden flows, is presented. Turbulent drag is used to account for particles turbulent dispersion. A new solid particle phase viscosity model is also developed from first principles. The present transport model resolves the saltation layer, instead of modelling it with equilibrium formulations as in one-way coupled models. Implementation is done in `foam-extend`, a community-driven fork of OpenFOAM® .

Validation in saltation is done against measurements from a controlled drifting snow experiment using real snow particles. The present model accurately predicts snow flux and airflow velocity in equilibrium and non-equilibrium regimes, when particle size polydispersity is considered. The model overestimates experimental measurements of turbulent kinetic energy, with concerns over the completeness of the measurements. Validation in suspension is done against measurements from a controlled sediment suspension experiment. The present model accurately predicts sediment concentration profiles, water velocity profiles, and sediment fall velocity. The present model is also shown to be superior to a one-way coupled convection-diffusion model based on an equilibrium formulation. Finally, a non-perforated boundary condition used to represent perforated bottoms is found to have a localized effect for the present model, and unsuitable for one-way coupled models. Using wall functions in such situations is also discouraged since it would produce turbulence structures very different from what is observed on perforated bottoms. A resolved low Reynolds number approach is recommended instead.

The present viscosity model predicts mixture viscosity accurately, and more physically than published mixture viscosity models. In the dense drifting snow regime, a volume fraction correction and multiplicative constant of 0.1 are suggested to improve the Kazhikov-Smagulov particle viscosity model, and a variable constant equal to the local phase density ratio for the Carrier-Cashwell particle viscosity model. Particle turbulent viscosity modelled with the C_t model is found negligible for drifting snow, and comparable to water turbulent viscosity for sediment, due to phase density ratio.

Keywords:
Eulerian-Eulerian, drifting snow, sediment transport, saltation, suspension, two-way coupling, turbulent drag, particle-laden flow, solid particle phase viscosity

Abstract

U ovom radu prikazan je Euler–Euler dvostrano spregnut model za simuliranje nošenja snijega i strujanja s česticama niske koncentracije. Turbulentna disprezija čestica modelirana je pomoću turbulentne viskoznosti, te je razvijen novi model viskoznosti nošenih čestica. Umjesto korištenja ravnotežne formulacije koju koriste jednostrano spregnuti modeli, u ovom radu koristi se transportni model koji razrješava saltacijski sloj. Implementacija je provedena u programu `foam-extend`, grani programa otvorenog koda OpenFOAM® .

Validacija saltacije je provedena uspoređujući rezultate s eksperimentalnim mjerenjima kontroliranog nosećeg snijega s pravim česticama snijega. Predstavljani model točno predviđa protok snijega i brzinu protoka zraka u ravnotežnim i neravnotežnim režimima u slučaju kada je raznovrsnost veličina čestica uzet u obzir. Model precjenjuje količinu turbulentne kinetičke energije u odnosu na eksperimentalna ispitivanja, međutim eksperimentalni podatci ne sadrže sve energetske frekvencije. Validacija suspenzije je provedena usporedbom s mjerenjima gdje je provedena kontrolirana suspenzija sedimenta. Razvijeni model točno procjenjuje kontrakciju sedimenta i profil brzine vode uzduž eksperimentalnog bazena, kao i brzinu padanja sedimenta. Osim toga, razvijeni model se pokazao boljim od jednostrano spregnutog modela baziranog na ravnotežnoj formulaciji. Nadalje, razvijeni model može koristiti nepropusni rubni uvjet umjesto perforiranog dna, što ima samo lokalni utjecaj na rezultat. Jednostruko spregnuti modeli nisu u mogućnosti koristiti nepropustan rubni uvjet. Korištene zidnih funkcija također nije preporučljivo koristiti u takvim slučajevima, jer dolazi do proizvodnje vrtložnih struktura koje su različite od onih koje se mogu naći na perforiranom dnu.

Razvijeni model viskoznosti točno predviđa viskoznog smjese u usporedbi s modelima u literaturi, te pokazuje fizikalnije rezultate. Prilikom gustog nošenog snijega, predlaže se korekcija udjela volumena snijega i konstantan koeficijent od 0.1 kako bi se poboljšao Kazhikov-Smagulov model viskoznosti čestica, te promjenjiva konstanta jednaka lokalnom udjelu volumena za Carrier-Cashwell model viskoznosti. Zbog odnosa gustoće čestica i fluida, turbulencija čestica modelirana pomoću C_t modela je zanemariva i usporediva turbulenciji vode prilikom sedimentacije.

Ključne riječi:
Euler-Euler, noseći snijeg, transport sedimenta, saltacija, suspenzija, dvostrana sprega, turbulentni otpor, strujanja s česticama niske koncentracije, viskoznost krutih čestica

Contents

List of Figures

List of Tables

Acronyms

AIAA American Institute of Aeronautics and Astronautics. 104

ASCE American Society of Civil Engineers. 2, 92, 95, 96, 98

BC Boundary Condition. 62, 64, 66, 67, 74, 76

CC Carrier-Cashwell. xv, xxii, xxv, 26, 28, 79, 81, 83, 84, 86

CFD Computational Fluid Dynamics. 1, 106

CICSAM Compressive Interface Capturing Scheme for Arbitrary Meshes. 22

CNBC Canadian National Building Code. 2

E-E Eulerian-Eulerian. xiv–xvi, 3, 14, 27, 39, 44, 60, 62, 64–75, 78–86

E-L Eulerian-Lagrangian. 3

FDM Finite Difference Method. 17

FEM Finite Element Method. 17

FVM Finite Volume Method. 17, 43

HPC High Performance Computing. 106

ID Inner Diameter. 40

KS Kazhikov-Smagulov. xv, xix, xx, xxii, xxvii, 26, 28, 78, 79, 81, 83, 84

MULES Multidimensional Universal Limiter with Explicit Solution. 22

OD Outer Diameter. 40

ODE Ordinary Differential Equation. 18

PDE Partial Differential Equation. 3

PDF Probability Distribution Function. 46

PGM Particle Group Model. 16

RANS Reynolds Averaged Navier-Stokes. 3

RHS Right Hand Side. 16, 68, 75

SANAE IV South African National Antarctic Expedition IV. 10

SPC Snow Particle Counter. 40

SS Steady-State. 12–14, 17, 18, 20, 64, 65

TSD Transport of Snow Density. 3, 4, 8, 27

USA United States of America. 2, 98, 101, 104

VOF Volume of Fluid. xiv, xv, 3, 7–9, 22, 27, 28, 60, 62, 64–75

Nomenclature

Greek symbols

α_1 volume fraction of snow phase, see equation (2.4), page 31

α_2 volume fraction of air phase, see equation (2.4), page 31

α_i volume fraction of phase i, see equation (2.2), page 30

α_w volume fraction of water, see equation (1.76), page 23

$\alpha_{1,max}$ maximum packing volume fraction of particles, see equation (1.90), page 25

α_4 calibration constant, see equation (1.65), page 18

α_5 calibration constant, see equation (1.65), page 18

α_a volume fraction of air, see equation (1.24), page 7

α_s volume fraction of snow/sediment, see equation (1.24), page 7

α_{sa} sediment volume fraction at level a, see equation (1.42), page 12

β exponential factor of KS particle viscosity model, see equation (1.97), page 27

β turbulence response function parameter, see equation (2.18), page 34

β bed slope, see equation (1.83), page 24

β experimental data fit constant, see equation (1.44), page 12

Δt time step, see equation (1.77), page 23

Δx computational cell size, see equation (1.77), page 23

Δz_s change in snow depth, see equation (1.12), page 5

Δ bed-form height, see equation (1.69), page 19

δ_{ij} Kronecker delta, see equation (1.1), page 3

ϵ_2 turbulent kinetic energy dissipation rate of air phase 2, see equation (2.16), page 33

ϵ turbulent kinetic energy dissipation rate, see equation (1.12), page 5

η non-dimensional height in channel, see equation (1.42), page 12

η_a non-dimensional height at level a in channel, see equation (1.42), page 12

ε bed porosity, see equation (1.66), page 18

Γ Γ function, see equation (3.3), page 48

$\dot{\gamma}_1$ particle phase rate of strain, see equation (2.32), page 36

γ_c coefficient accounting for crossing trajectory effects, see equation (1.55), page 15

κ von Kármán constant, see equation (1.36), page 9

μ_0 multiplicative constant of KS particle viscosity model, see equation (1.97), page 27

μ_1 dynamic viscosity of particle phase, see equation (2.25), page 35

μ_2 continuous phase dynamic viscosity, see equation (1.87), page 25

μ_a dynamic viscosity of air, see equation (1.20), page 6

μ_{eff} effective dynamic viscosity from turbulence modelling, see equation (1.76), page 23

$\mu_{m,\alpha}$ mixture viscosity based on volume fraction weighting, page 78

$\mu_{m,U}$ mixture viscosity based on mixture velocity gradient, see equation (5.1), page 78

μ_m mixture dynamic viscosity, see equation (1.24), page 7

μ_s friction coefficient, see equation (1.85), page 24

μ_s snow dynamic viscosity, see equation (1.27), page 8

μ_t air turbulent viscosity, see equation (1.3), page 4

ν_1 kinematic viscosity of particle phase, page 79

ν_a air kinematic viscosity, see equation (1.36), page 9

ν_{eff1} effective viscosity of the snow/sediment phase, page 81

ν_{eff2} effective viscosity of the air/water phase, page 81

$\nu_{t,max}^e$ maximum turbulent viscosity at equilibrium, see equation (1.65), page 18

ν_2 air kinematic viscosity, see equation (2.7), page 31

ν_i kinematic viscosity of phase i, see equation (2.14), page 32

ν_w water kinematic viscosity, see equation (1.70), page 19

ν_{eff_i} effective kinematic viscosity of phase i, see equation (2.13), page 32

$\nu_{t,max}$ maximum turbulent viscosity, see equation (1.63), page 18

ν_{t1} turbulen kinematic viscosity of snow, phase 1, see equation (2.23), page 34

ν_{t2} turbulent kinematic viscosity of air, phase 2, see equation (2.11), page 32

ν_{ti} turbulent kinematic viscosity of phase i, see equation (2.14), page 32

ν_{ts} sediment turbulent diffusivity, see equation (1.62), page 18

ω_0 settling velocity of a single particle, see equation (1.44), page 12

ω_s snowfall settling velocity, see equation (1.1), page 3

ψ particle packing parameter, see equation (1.92), page 26

ϕ angle between the velocity vector and bed steepest slope direction, see equation (1.85), page 24

$\phi_{s,sal}^{in}$ horizontal saltation drift densities entering the cell, see equation (1.7), page 5

$\phi_{s,sal}^{out}$ horizontal saltation drift densities leaving the cell, see equation (1.7), page 5

ϕ_s snowdrift density, see equation (1.1), page 3

$\phi_{s,g}$ snowdrift density in the grid cell on the surface, see equation (1.14), page 6

$\phi_{s,top}$ snowdrift density at the top of the grid cell, see equation (1.11), page 5

ρ_1 density of phase 1, see equation (2.4), page 31

ρ_2 density of phase 2, see equation (2.4), page 31

ρ_i density of phase i, see equation (2.2), page 30

ρ_a air density, see equation (1.2), page 3

ρ_m mixture density, see equation (1.24), page 7

ρ_s snow density, see equation (1.2), page 3

ρ_w water density, see equation (1.60), page 16

ρ_{ice} density of ice, see equation (1.15), page 6

σ_k turbulent kinetic energy Schmidt number, see equation (2.15), page 33

σ_ϵ turbulent kinetic energy dissipation rate Schmidt number, see equation (2.16), page 33

σ_c turbulent Schmidt number of sediment mass transport, see equation (1.38), page 11

σ_t snowdrift density Schmidt number, see equation (1.3), page 4

σ_α turbulent Schmidt number of air, phase 2, see equation (2.11), page 32

θ Shields number, see equation (1.83), page 24

τ_1 shear stress in the particle phase, page 78

τ_2 shear stress in the fluid phase, page 78

τ_b bed surface shear stress vector, see equation (1.82), page 23

τ_p particle response time, see equation (1.55), page 15

τ_t threshold shear stress, see equation (2.28), page 36

τ_{fb} bulk measure of the fluid's turbulent integral time scale, see equation (1.55), page 15

θ particle incidence angle with the snow bed, see equation (1.34), page 9

θ_t^* threshold Shields number adjusted to bed slope, see equation (1.83), page 24

θ_t threshold Shields number, see equation (1.83), page 24

Latin symbols

$P_{E,v}$ Eulerian linear momentum per unit volume, see equation (2.31), page 36

A proportionality constant related to snow particle shape for threshold shear stress calculation, see equation (3.1), page 45

a shape parameter of the two-parameter Γ PDF, see equation (3.3), page 48

a_0 exponential factor of KS particle viscosity model, see equation (1.97), page 27

A_{cc} multiplicative constant for CC particle phase viscosity model, see equation (1.94), page 26

A_{ks} multiplicative constant for KS particle phase viscosity model, see equation (5.2), page 78

A proportionality constant representing the snow pack bonding strength, see equation (1.34), page 9

a arbitrary reference height, see equation (1.40), page 12

a non-dimensional constant, see equation (1.19), page 6

A_s non-dimensional constant, see equation (1.19), page 6

A_{hol} horizontal surface area of the top of the cell, see equation (1.11), page 5

A_{side} surface area at the vertical side face, see equation (1.7), page 5

B non-dimensional constant, see equation (1.36), page 9

b scale parameter of the two-parameter Γ PDF, see equation (3.3), page 48

B empirical constant a, see equation (1.47), page 13

b flow width, see equation (1.66), page 18

C_1 $k - \epsilon$ model constant, see equation (2.16), page 33

C_2 $k - \epsilon$ model constant, see equation (2.16), page 33

$\overline{c}_s$ depth-averaged sediment concentration, see equation (1.66), page 18

C constant accounting for the bed slope effect, see equation (1.82), page 23

c dimensionless saltation velocity proportionality constant, see equation (1.5), page 4

c_0 dimensionless empirical constant, see equation (1.9), page 5

c_1 non-dimensional constant, see equation (1.36), page 9

c_b^* sediment equilibrium concentration, see equation (1.79), page 23

C_d drag coefficient, see equation (1.2), page 3

c_p pollutant concentration, see equation (1.72), page 20

c_s sediment mass fraction, see equation (1.38), page 11

C_t turbulence response function, see equation (2.17), page 33

C_v constant related to the vertical turbulent intensity, see equation (1.55), page 15

C_α target compressive surface Courant number, see equation (1.77), page 23

$C_{\epsilon s}$ non-dimensional particle damping constant for ϵ equation source term, see equation (1.18), page 6

$C_{\mu r}$ $k - \epsilon$ constant with curvature effect, see equation (1.73), page 20

C_{μ} non-dimensional $k - \epsilon$ model constant, see equation (1.22), page 7

C_{ks} particle damping constant for k equation source term, see equation (1.17), page 6

C_{l1} lift coefficient of phase 1, see equation (2.4), page 31

C_{l2} lift coefficient of phase 2, see equation (2.4), page 31

c_{s0} sediment mass fraction at height y_0, see equation (1.53), page 14

c_{sa} sediment mass fraction at height a, see equation (1.40), page 12

C_{vm1} virtual mass coefficient of snow, phase 1, see equation (2.9), page 32

C_{vm2} virtual mass coefficient of air, phase 2, see equation (2.9), page 32

d_i particle size of class i in two-parameter Γ distribution, see equation (3.5), page 48

D_{16} 16 % diameter of a size distribution, page 61

D_{84} 84 % diameter of a size distribution, page 61

d_{avg} average diameter of the two-parameter Γ PDF, see equation (3.4), page 48

D_* non-dimensional sediment particle diameter, see equation (1.69), page 19

D_b sediment deposition rate, see equation (1.78), page 23

D_f inverse drag function, see equation (1.30), page 8

d_p snow particle diameter, see equation (1.2), page 3

D_s sediment damping coefficient, see equation (1.60), page 16

D_w water damping coefficient, see equation (1.60), page 16

D_{50} median diameter of sediment size distribution, see equation (1.69), page 19

E non-dimensional height transformation, see equation (1.47), page 13

e dimensionless saltation efficiency, see equation (1.5), page 4

E_a non-dimensional height transformation at level a, see equation (1.47), page 13

E_b sediment entrainement rate, see equation (1.78), page 23

$f(x)$ two-parameter Γ PDF, see equation (3.3), page 48

$\mathbf{F}_d$ drag force vector, see equation (2.3), page 30

$\mathbf{F}_l$ lift force vector, see equation (2.3), page 30

$\mathbf{F}_t$ turbulent drag force vector, see equation (2.3), page 30

$\mathbf{F}_{vm}$ virtual mass force vector, see equation (2.3), page 30

F_D drag force, see equation (1.58), page 15

f_s non-dimensional damping function, see equation (1.17), page 6

$\mathbf{g}$ gravitational acceleration vector, see equation (2.2), page 30

g gravitational acceleration, see equation (1.2), page 3

h shortest distance between the outer circumferences of neighbouring particles in CC particle phase viscosity model, see equation (1.94), page 26

h channel water level, see equation (1.42), page 12

h_{sal} saltation height, see equation (1.8), page 5

$\mathbf{I}$ identity matrix, see equation (2.13), page 32

k_2 turbulent kinetic energy of air phase 2, see equation (2.15), page 33

K drag function, see equation (2.5), page 31

K proportionality constant accounting for particles and snow pack material properties, see equation (1.34), page 9

k turbulent kinetic energy, see equation (1.12), page 5

k_i turbulent kinetic energy of phase i, see equation (2.13), page 32

K_s aerodynamic surface roughness, see equation (1.36), page 9

K_s^+ non-dimensional aerodynamic surface roughness, see equation (1.36), page 9

l turbulent mixing length, see equation (1.40), page 12

L_e characteristic length of energy containing eddies, see equation (2.19), page 34

$\mathbf{M}_i$ inter-phase momentum exchange term of phase i, see equation (2.2), page 30

m empirical exponent, see equation (1.44), page 12

z Rouse number corrected for crossing trajectory effects, see equation (1.54), page 15

Z_0 Rouse number of a single particle, see equation (1.44), page 12

z_b sediment bed level, see equation (1.66), page 18

Miscellaneous

$\langle . \rangle$ ensemble average operator

∇_s surface gradient

Subscripts

$*$ friction parameter

$+$ wall coordinate

eff effective parameter

t threshold parameter

Superscripts

$'$ turbulent fluctuation

T transpose

Chapter 1

Introduction

This thesis is concerned with the numerical simulation of falling and drifting snow. Its objective is to present a viable Computational Fluid Dynamics (CFD) model to assess loads due to snowdrifts as well as snowfall on and around buildings and structures of arbitrary shapes. In this chapter, the general context of the problem will be discussed and the state-of-the-art in CFD simulation of drifting snow is reviewed with a discussion of the advantages and disadvantages of the presented methods. Sediment transport by water is also discussed, since its governing physics are quite similar to those of drifting snow, with similar CFD methods used for simulations of sediment transport. This discussion is complementary to that of drifting snow since sediment transport by water occurs under a solid to fluid phase density ratio of order $O(1)$, while drifting snow occurs under a solid to fluid phase density ratio of order $O(100)$, similar to the aeolian transport of sand. Based on these two discussions a new CFD model will be proposed which is believed to be an improvement on existing models.

1.1   Drifting Snow

Drifting snow results from the aeolian motion of individual snow particles deposited on the ground. Such motion is possible when the drag force induced by the wind exceeds the opposing actions of inter-particle cohesive bonding, particle weight and surface friction. The corresponding surface shear stress is called the *threshold shear stress* with its shear velocity termed the *threshold shear velocity*. Bagnold [1] classified the aeolian motion of particles under three modes, shown in Figure 1.1:

- *Surface creep*, where particles move in contact with the surface for a few centimetres or in very short hops after being dislodged by saltating particles.

- *Saltation*, where the particles bounce off the surface in a thin layer approximately 10 cm thick and for relatively long hops leeward; this mode is dominant in snow-storms [2].

- *Suspension,* where the lightest particles are lifted by the airflow to great heights that could reach 100 m above the ground, depending on the level of turbulence in the airflow, and deposited further downstream.

In the creep and saltation layers, where the heaviest particles are transported, the airflow velocity is affected by the particles; this is a two-way coupling effect. In contrast, in the suspension layer where the smallest particles evolve the airflow velocity is not affected and the particles follow the streamlines; this is a one-way coupling effect.
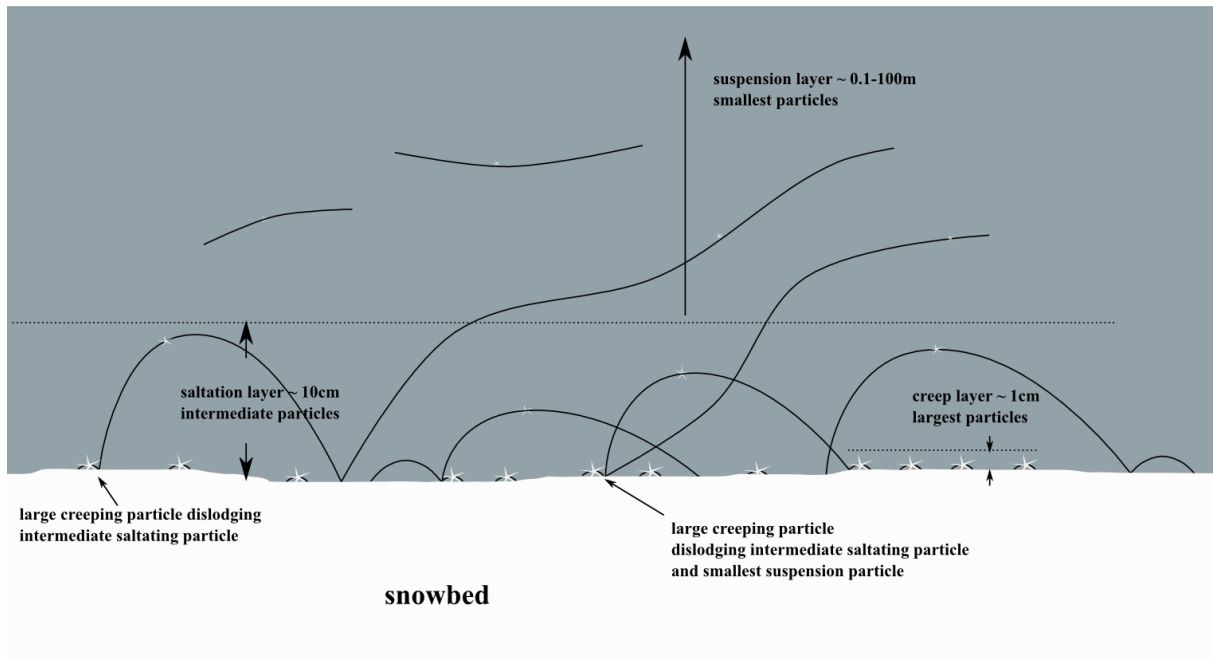
Figure 1.1: Aeolian transport modes during drifting snow.

Loads resulting from snow accumulation can lead to disastrous consequences on building roof structures if not properly accounted for in the structural design. The Canadian National Building Code (CNBC) [3] and its United States of America (USA) counterpart by the American Society of Civil Engineers (ASCE) [4] address snow loads by using the 50-year ground snow load corrected with a host of load factors to try to account for building type, roof shape and slope, wind exposure, and importance based on the general characteristic dimensions of the structure. In sections 7-10 of the ASCE code drifting snow is only accounted for around rectangular roof structures and lower roofs forming step configurations, by estimating the drift width and height based on empirical factors derived from a number of cases recorded by insurance companies. It is not clear how to assess other snow drift loads due to arbitrary structures of unusual shape using building code procedures.

Snow particles are also subject to sublimation and melting under the right conditions, sublimation being phase conversion from solid to gaseous (water vapour) without the intermediate melting step. Sublimation is shown to reduce the snow cover by about 10 %

on long terrain fetches over $1000\,\text{m}$ such as prairie, tundra, and arctic catchments [5–8]. Otherwise, sublimation effects are generally smaller than the experimental error so they will be neglected in the present context.

Melting causes the snow particles to change from a solid granular phase to a liquid one. This is likely to lead to even less snow on the ground, or a much heavier and more viscous snow, reducing the snow propensity to drift. Therefore, neglecting melting is most likely to produce conservative drifting snow loads. Moreover, estimating snowmelt will require solving an additional energy equation with short wave solar radiation effects. This is beyond the scope of the present study.

Several aeolian snow transport models are available in the literature. Most of these models are based on E-E [9–17] and Eulerian-Lagrangian (E-L) [18–20] Reynolds Averaged Navier-Stokes (RANS) formulations, where the two phases are air and snow. Both models can yield reasonable results for particulate flows as compared to experiments but the E-E model requires much less computational resources since Lagrangian particle tracking requires a great deal of particles to yield statistically meaningful results and is usually restricted to small areas of about a couple of square metres [21, 22]. E-E modelling can result in a much more practical engineering tool than E-L. Therefore, this discussion will be limited to the state of the art in E-E modelling. Namely, the discussion will focus on the Transport of Snow Density (TSD) and VOF models.

1.1.1   The Transport of Snow Density Model

The TSD model relies on solving a one-way coupled convection-diffusion transport Partial Differential Equation (PDE) for the drifting snow density in the suspension layer (equation 1.1), in addition to the airflow continuity and momentum equations. It was originally introduced by Uematsu *et al.* [9] with subsequent improvements [23], and later adopted by several groups [10, 11, 24, 25] with different refinements in the physical modelling.

$$\frac{\partial \phi_s}{\partial t} + \nabla \cdot (\mathbf{u}_a - \omega_s \delta_{j3})\phi_s = \nabla \cdot (-\overline{\mathbf{u}'_a \phi'_s}). \tag{1.1}$$

Here, ϕ_s is the snowdrift density, $\mathbf{u}_a$ is the airflow velocity vector, and δ_{j3} is the Kronecker delta with $j = 3$ being the vertical gravity direction. The snowfall settling velocity ω_s can be calculated using expressions based on buoyancy and drag considerations such as the one adopted by Tominaga *et al.* [11],

$$\omega_s = -\sqrt{\frac{8}{3}\left(\frac{\rho_a}{\rho_s} - 1\right)\frac{d_p}{C_d}g}, \tag{1.2}$$

Here, ρ_a and ρ_s are respectively the air and snow density, d_p the snow particle diameter, C_d the snow particle drag coefficient and g the gravitational acceleration. In practice, the different adepts of the TSD method mentioned above set ω_s to a constant value ($0.1\,\text{m}\cdot\text{s}^{-1}$

to $0.5\,\mathrm{m} \cdot \mathrm{s}^{-1}$) based on observations or experimental measurements. The third term on the left accounts for gravitational sedimentation of the falling snow and the right hand side accounts for turbulent diffusion modelled with a gradient diffusion hypothesis,

$$-\overline{\mathbf{u}_a' \phi_s'} = \frac{\mu_t}{\sigma_t} \nabla \phi_s. \tag{1.3}$$

Here, μ_t is the turbulent viscosity of air and σ_t is the snowdrift density Schmidt number normally set to 1. For incompressible flow $\nabla \cdot \mathbf{u}_a = 0$, so equation 1.1 becomes,

$$\frac{\partial}{\partial t}\phi_s + \mathbf{u}_a \cdot \nabla \phi_s - \nabla \left(\phi_s \omega_s \delta_{j3} \right) = \nabla \cdot \left(\frac{\mu_t}{\sigma_t} \nabla \phi_s \right). \tag{1.4}$$

The most recent evolution of the TSD model by Tominaga *et al.* [26] uses equation 1.5 as boundary condition at the ground. This is a steady-state empirical formulation of the *saturated* transport rate of drifting snow in the saltation layer for equilibrium conditions over natural flat terrain, with zero streamwise gradients of snow transport and wind velocity [27].

$$Q_{sal} = \frac{0.68 \rho_a u_{*t}}{u_* g}(u_*^2 - u_{*t}^2). \tag{1.5}$$

Here, u_{*t} the surface threshold velocity and u_* the surface shear velocity. It should be noted that [27] state the 0.68 factor to be dimensionless. However, based on their definition of said factor $c \cdot e = 0.68/u_*$, where c is a dimensionless saltation velocity proportionality constant and e is a dimensionless saltation efficiency, the 0.68 factor should clearly have dimensions of velocity. This is also required for dimensional consistency of equation 1.5 so that Q_{sal} would have the correct dimensions of $\mathrm{kg} \cdot \mathrm{m}^{-1} \cdot \mathrm{s}^{-1}$. Okaze *et al.* [28] experimentally study the saltation of loose snow in accelerating and decelerating flows and find equation 1.5 to overestimate the transport rate of drifting snow under such conditions. The boundary condition at the top of the suspension layer is given from the snowfall precipitation rate, which can be set constant or obtained from mesoscale simulations or meteorological data [29]. Determining the snowdepth starts with a mass balance of the snow phase in the first grid cell above the ground or the snowbed [26], expressed as,

$$M_{total} = M_{side} + M_{top}. \tag{1.6}$$

Here, M_{total}, M_{side} and M_{top} are respectively the total snow mass transport, snow mass transport at the side and the top of the cell. The snow mass transport at the side is calculated as,

$$M_{side} = V_{side} A_{side} (\phi_{s,sal}^{in} - \phi_{s,sal}^{out}). \tag{1.7}$$

Here, V_{side} and A_{side} are the horizontal velocity at the vertical side face and its surface area respectively. $\phi_{s,sal}^{in}$ and $\phi_{s,sal}^{out}$ are respectively the horizontal saltation drift densities entering and leaving the cell. The drift density $\phi_{s,sal}$ is estimated using the empirical equation 1.8 [9, 30].

$$\phi_{s,sal} = \frac{Q_{sal}}{U_{sal}h_{sal}}. \tag{1.8}$$

Here Q_{sal} is obtained from equation 1.5. The saltation velocity U_{sal} is calculated using another equilibrium empirical relationship by Pomeroy *et al.* [27],

$$U_{sal} = c_0 u_{*t}. \tag{1.9}$$

Here, $c_0 = 2.8$ is an empirical constant relating to the mean velocity of saltating particles [31]. The saltation height h_{sal} can be calculated using a steady-state empirical relationship to the friction velocity by Pomeroy and Malé [32],

$$h_{sal} = 0.0843u_*^{1.27}. \tag{1.10}$$

However, in practice the height of the grid cell is also used [26]. The snow mass transport at the top of the cell is calculated using the following relationship,

$$M_{top} = -\phi_{s,top}(w + \omega_s)A_{hol}. \tag{1.11}$$

Here, $\phi_{s,top}$ is the snowdrift density at the top of the grid cell, w and ω_s are the airflow vertical velocity and the snowfall velocity respectively, and A_{hol} is the horizontal surface area of the top of the cell. The change in snow depth Δz_s is calculated using ρ_s as follows,

$$\Delta z_s = \frac{M_{total}}{\rho_s A_{hol}}. \tag{1.12}$$

A grid cell at the surface is arbitrarily closed when the snow depth in it becomes equal to the grid height. However, when $M_{total} < 0$, it is included as a sink term in equation 1.1. In the above model turbulence is modelled with the $k - \epsilon$ model applied to the airflow.

Tominaga *et al.* [11] use a modified version of the above model, where the saltation snowdrift density at the ground is not calculated using equation 1.5. Instead, ground saltation is included into a variable inlet boundary profile for the snowdrift density and the saltation effect is computed with equation 1.1. The snow layer height is computed using the net deposition rate,

$$M_{net} = M_{dep} + M_{ero}. \tag{1.13}$$

Here, M_{dep} is the deposition rate on the ground given by,

$$M_{dep} = -\phi_{s,g}\omega_s A_{hol}. \tag{1.14}$$

Here, $\phi_{s,g}$ is the snowdrift density in the grid cell on the surface. M_{ero} is the erosion rate on the ground and is computed with the following empirical expression for steady-state equilibrium saltation of sand particles [33],

$$M_{ero} = -5.0\text{x}10^{-4}\rho_{ice}u_* \left(1 - \frac{(u_{*t})^2}{(u_*)^2}\right) A_{hol}. \tag{1.15}$$

Here, ρ_{ice} is the density of ice. Snow depth change is calculated similarly to the initial model [26]. When $u_* > u_{*t}$ and the snowbed is eroding the following surface boundary condition is used,

$$-\frac{\nu_t}{\sigma_t}\nabla \cdot \left(\delta_{j3}\phi_s\right) = \frac{|M_{ero}|}{A_{hol}} \tag{1.16}$$

Source terms are added to the right-hand side of the turbulence equations to account for the damping of turbulent kinetic energy k and dissipation rate ϵ by snow particles, as done originally by Naaim *et al.* [10]. These terms are,

$$S_k = -C_{ks}f_s\frac{k}{\rho_s t_r}\phi_s, \tag{1.17}$$

$$S_\epsilon = -C_{\epsilon s}f_s\frac{\epsilon}{\rho_s t_r}\phi_s. \tag{1.18}$$

Here, f_s is the damping function given by,

$$f_s = 1 - exp\left\{\left(-\frac{t_r}{A_s(k/\epsilon)}\right)^a\right\}, \tag{1.19}$$

and t_r is a damping time scale given by,

$$t_r = \frac{d_p^2\rho_s}{18\mu_a}. \tag{1.20}$$

Here, C_{ks}, $C_{\epsilon s}$, A_s and a are model constants optimized respectively to 2×10^4, 0.0, 10.0 and 1.0 [28]. The turbulent kinematic viscosity is calculated using a turbulent time scale correction to account for the excess production of turbulent kinetic energy typical of the standard $k - \epsilon$ model [34], as it was previously found to agree best with experimental results [35]. This correction is implemented as follows,

$$\nu_t = C_\mu kT, \tag{1.21}$$

$$T = min(\frac{k}{\epsilon}, \frac{1}{C_\mu S \sqrt{6}}). \tag{1.22}$$

Here, $C_\mu = 0.09$ is the familiar $k - \epsilon$ model constant and S is the rate of strain given by,

$$S = \sqrt{\left(\frac{\partial u_x}{\partial y} + \frac{\partial u_y}{\partial z} + \frac{\partial u_z}{\partial x}\right)^2}. \tag{1.23}$$

Both models were validated against detailed measurements of snowdrift around a surface mounted cube with a height of 1 m, taken during an outdoors snowdrift event [36]. The outdoors measurements were also successfully reproduced in a controlled wind tunnel experiment using artificial snow [37]. The simulation results of the initial model based on equation 1.5 showed a general order of magnitude agreement in snowdrift levels and limits with the experimental measurements. In particular, the snowdrift limits were seen to correspond closely to the friction velocity levels. Profiles of snowdrift height in vertical plane cuts along the centre of the cube and parallel to the cube's lateral and longitudinal axes showed very large and non-physical oscillations. The improved treatment without 1.5 mitigated the oscillations to a large degree, but did not remove them altogether. The simulated snowdrift height and limits agreed better with the experimental measurements but still in order of magnitude only. This was especially true on the lateral sides of the cube where shear dominates. The simulations overestimate the snow deposition windward and leeward of the cube, which is arguably due to the lack of impingement erosion in both simulation models.

1.1.2 The Volume of Fluid Model

The VOF model is a one-way coupling interface tracking method that treats the snow phase as a fluid and relies on the assumption that the fluids are not interpenetrating. It consists of mixture transport equations with the addition of a scalar transport equation for the volume fraction of either phase [38]. The volume fraction equation is equivalent to a mass continuity equation, and takes the following general form for drifting snow,

$$\frac{\partial \alpha_a}{\partial t} + \mathbf{u}_m \cdot \nabla \alpha_a + \nabla \cdot (\alpha_a \mathbf{u}_r) = \nabla \cdot \left(\nu_t \nabla \alpha_a\right). \tag{1.24}$$

Here α_a is the volume fraction of air, $\mathbf{u}_m$ is the mixture velocity vector, and $\mathbf{u}_r$ is the relative velocity vector between the two phases. The system is closed with the mixture relationship for density,

$$\rho_m = \alpha_a \rho_a + \alpha_s \rho_s. \tag{1.25}$$

Here, $\alpha_s = 1 - \alpha_a$ is the volume fraction of snow which can be used to calculate the drifting density of snow in 1.1 with the following relationship,

$$\phi_s = \alpha_s \rho_s. \tag{1.26}$$

A similar relationship can be used for the mixture viscosity,

$$\mu_m = \alpha_a \mu_a + \alpha_s \mu_s. \tag{1.27}$$

However, there are no known relationships or values for the snow viscosity. Most authors neglect the mixture molecular viscosity with respect to the eddy viscosity. This model is justified in the turbulence production layers where the eddy viscosity can be several orders of magnitude larger than the air molecular viscosity, and such regions are typically close to the snowbed for drifting snow. In the suspension layer, the flow is so dilute that an inviscid treatment of the snow phase can be justified, and one can use the air viscosity alone. However, there might exist transitional layers between the snowbed turbulence generation layers and the suspension layer where the snow phase is dense enough to justify viscous treatment, which could affect the mixture viscosity. Other authors do not neglect the snow viscosity and use different models to address this issue. Thiis [17] uses an assumed logarithmic velocity profile with roughness for the airflow in combination with the threshold shear stress calculated from the known threshold friction velocity to estimate the mixture vicosity. For antarctic wind-hardened snow with $u_* = 0.6 \, \mathrm{m \cdot s^{-1}}$, he arrives at a mixture viscosity value of $\mu_m = 2.7 \times 10^{-4} \, \mathrm{N \cdot m^{-2}}$.

The VOF and TSD equations are equivalent. Should we replace α_a by $(1 - \alpha_s)$ in equation 1.24, multiply both sides by ρ_s and rearrange, we get the following transport equation for the drifting snow density,

$$\frac{\partial \phi_s}{\partial t} + \mathbf{u}_m \cdot \nabla \phi_s + \nabla \cdot (\phi_s \mathbf{u}_r) = \nabla \cdot \left(\nu_t \nabla \phi_s \right). \tag{1.28}$$

Equation 1.24 is exactly similar to equation 1.4 with ω_s replaced by $\mathbf{u}_r$. The phase relative velocity $\mathbf{u}_r$ is calculated with the following expression according to the drift flux theory [12],

$$\mathbf{u}_r = \alpha_a \alpha_s D_f \left(\frac{\rho_s - \rho_a}{\rho_a} \right) \frac{1}{\rho_m} \nabla p, \tag{1.29}$$

$$D_f = \frac{9 \mu_a}{2 d_p^2}. \tag{1.30}$$

Here, p is the static air pressure, and D_f is an inverse drag function assuming Stokes flow between a spherical particle and the air phase. The relative velocity expression is based on a balance between a driving body force, the pressure gradient and the drag force and assumes low relative velocities. In comparison, ω_s as calculated by expression 1.2 is based on body and drag forces without the pressure gradient which can be negligible in low speed incompressible boundary layer flows. Equations 1.24 and 1.4 are therefore equivalent. The snow mass transport information used to track the free interface between the phases allows blocking or releasing cells as they fill up with snow or gradually empty.

Several authors have adopted the VOF model [12–17], all using erosion and deposition mechanisms based on equation 1.5, which as discussed previously applies to steady-state equilibrium conditions. However, Beyers *et al.* [13] use the following expressions for the net erosion/deposition flux $q_{ero/dep}$ which accounts for erosion by particle impingement as well,

$$q_{ero/dep} = q_{depshear} + q_{eroshear} + q_{eroimp} \tag{1.31}$$

Here, $q_{depshear}$, $q_{eroshear}$ and q_{eroimp} are the fluxes of deposition by shear, erosion by shear and erosion by impingement, respectively. They are calculated as follows,

$$q_{depshear} = \begin{cases} \rho_s \omega_s \dfrac{u_{*t}^2 - u_*^2}{u_{*t}^2} & \text{if } u_{*t} > u_*, \\[2ex] 0 & \text{if } u_{*t} \leq u_*. \end{cases} \tag{1.32}$$

$$q_{eroshear} = \begin{cases} A\left(u_*^2 - u_{*t}^2\right) & \text{if } u_* > u_{*t}, \\[2ex] 0 & \text{if } u_* \leq u_{*t}. \end{cases} \tag{1.33}$$

$$q_{eroimp} = KV^n \rho_s f(\theta). \tag{1.34}$$

Here, $A = 7 \times 10^{-4}\,\text{kg} \cdot \text{m}^{-3}$ is a proportionality constant representing the snow pack bonding strength [10], K is a proportionality constant accounting for particles and snow pack material properties, V is the near-surface impinging airflow velocity, n is an index expressing the characteristics of a snow surface and is in the range $2 < n < 4$ for erosion of brittle material, as reported by Humphrey [39] for Adler [40]. θ is the particle incidence angle with the snow bed.

$$f(\theta) = \frac{16}{\pi^2}\theta^2 - \frac{8}{\pi}\theta + 1.0. \tag{1.35}$$

The function $f(\theta)$ is not physically based and merely allows maximum erosion by particle impingement normal to the surface, while tending to zero for $\theta = 45°$.

Turbulence is modelled with the standard $k-\epsilon$ model. The particle effect on turbulence was indirectly addressed by the following flow velocity wall function modified to account for increased surface roughness and saltating particles,

$$u(z) = \frac{u_*}{\kappa}ln\left(\frac{zu_*}{\nu_a}\right) + B - \Delta B(K_s^+, s^+). \tag{1.36}$$

Here, ν_a is the air kinematic viscosity, $B = 5.5$ and,

$$\Delta B(K_s^+, s^+) = \frac{1}{\kappa}ln(1 + 0.3K_s^+ + 9.53s^+). \tag{1.37}$$

Here, z is the coordinate normal to the surface, κ is the von Kármán constant, $K_s^+ = K_s u_*/\nu_a$ is the non-dimensional aerodynamic surface roughness and $s^+ = c_1 u_*/2g\nu_a$ is a parameter meant to represent two-way coupling effects of saltating particles on the airflow. This model is based on findings that the saltation layer behaves as an increased aerodynamic roughness to the flow above it [41]. This applies to well-developed boundary layers and would be uncertain for flow around a bluff body. The roughness modifications were based on measurements made during the experiment being simulated and specific to the experimental conditions [42].

Beyers *et al.* [13] present simulation results of an outdoors snowdrift experiment carried out at the South African National Antarctic Expedition IV (SANAE IV) antarctic research station [42]. The simulation captures the general accumulation locations and scales, an order of magnitude agreement with notable inaccuracies possibly due to the $k - \epsilon$ model, according to the simulation authors. Simulated snowdrifts are found to correlate well with friction velocities, in agreement with findings of other authors [11, 17]. Observations of leeward accumulation are not reproduced raising the question of unaccounted precipitation during the experiment. Impingement erosion as implemented in equation 1.31 is found too small in the leeward bubble, and wind velocity profiles results are not reported. Therefore, it is not possible to assess the validity of the wall function treatment.

Beyers *et al.* [14] implement the above model in Fluent 6.2 with the addition of mesh adaptation. The change in height of the cell vertices is computed using a balance of the convected horizontal snow flux based on flow divergence at the ground [15, 43]. However, there is no decisive improvement over the original model.

1.2   Sediment Transport by Water

Sediment transport in bodies of water is an important phenomena for hydraulic engineering applications. It governs bed response around structures such as dikes, weirs, and submerged bridge components, to name only a few. The transported sediment load is generally classified in three categories: the bed load, the suspended load, and the wash load, shown in Figure 1.2. The bed load moves closest to the sediment bed by rolling, sliding, or saltation, and consists of the heaviest constituents that often stop and move again under the action of water and other colliding constituents. As the flow gets stronger, parts of the bed load are carried upwards by turbulence to the middle part of the flow. This is the suspended load and it consists of lighter constituents than the bed load that move longer distances as well. The wash load consists of the smallest and lightest sediment constituents, with sizes all the way down to fractions of a micrometer. These constituents are light enough to stay suspended and are never represented in the bed even when present in large quantities. The physics governing sediment transport by water are quite similar to

those of aeolian transport of snow and sand, discussed at length in the previous section. The main difference between hydro and aeolian transport of solid particles is the solid to fluid phase density ratio which is of order $O(100)$ for the former, and $O(1)$ for the latter.

Several models are available to simulate sediment concentration transport, and they can be classified in two broad categories: analytical and numerical models. In what follows the most representative methods of both models are concisely reviewed.
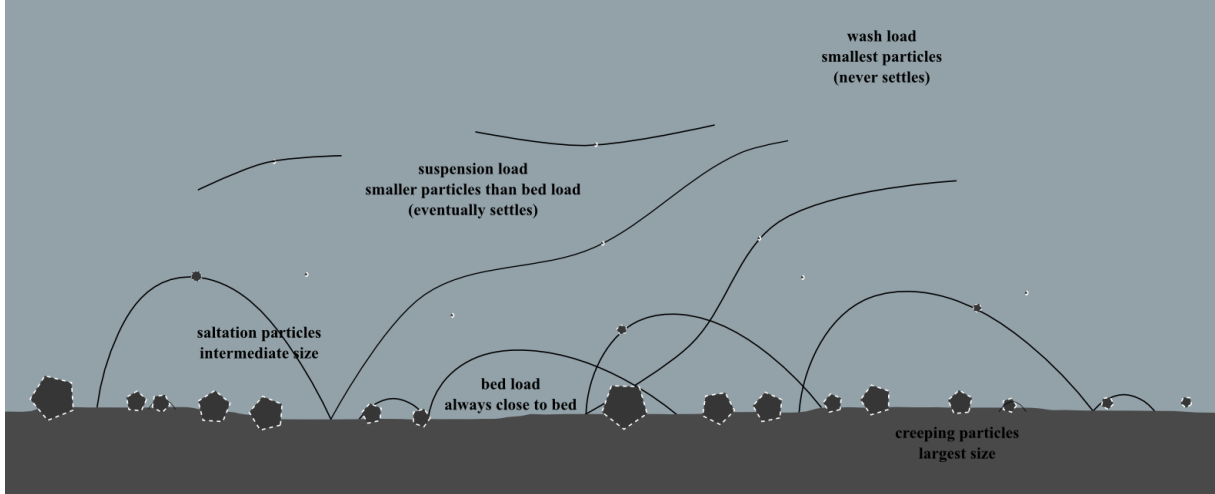
Figure 1.2: Sediment transport modes.

1.2.1 Analytical Models of Sediment Concentration Transport

Analytical models of sediment concentration transport are usually derived from the conservation equation of the sediment mass fraction c,

$$\frac{\partial c_s}{\partial t} + \nabla \cdot (\mathbf{u}_w - \omega_s \delta_{j3}) c_s = \nabla \cdot \left(\frac{\nu_t}{\sigma_c} \nabla c_s \right). \tag{1.38}$$

Here, $\mathbf{u}_w$ is the water velocity vector, c_s is the sediment concentration, ω_s is the sediment fall velocity, δ_{j3} is the Kronecker delta with $j = 3$ the vertical direction, σ_c is the turbulent Schmidt number typically taken as 1, and ν_t is the flow turbulent kinematic viscosity. It should be noted that equation 1.38 is similar to equations 1.4 and 1.24. For steady open-channel flow, equation 1.38 reduces to the following vertical equilibrium equation,

$$\omega_s c_s + \frac{\nu_t}{\sigma_c} \nabla \cdot \left(\delta_{j3} c_s \right) = 0. \tag{1.39}$$

Equation 1.39 is sometimes referred to as the Schmidt equation [44]. Assuming constant settling velocity and turbulent momentum and mass transfer coefficients, equation 1.39 can be integrated to yield the Schmidt concentration profile,

$$ln \frac{c_s}{c_{sa}} = -\frac{\omega_s \sigma_c}{\nu_t} (y - a). \tag{1.40}$$

Here, a is an arbitrary reference height. Schmidt derived equation 1.40 in the context of atmospheric dust transport. However, a similar procedure is used for sediment transport. Prandtl's mixing length model [45] allows one to write,

$$\nu_t = l^2 \left| \frac{\partial u}{\partial y} \right|.$$ (1.41)

Here, l is the turbulent mixing length. If one additionally assumes $\sigma_c = 1$ and derives the velocity gradient from a logarithmic profile, equation 1.39 can be integrated to yield,

$$\frac{c_s}{c_{sa}} = \left(\frac{\eta_a}{\eta} \cdot \frac{1 - \eta}{1 - \eta_a} \right)^Z.$$ (1.42)

Here, c_{sa} is the sediment mass concentration at the arbitrary reference height a, h is the water level in the channel, $\eta = y/h$, $\eta_a = a/h$, and $Z = \omega_s / \kappa u_*$ is the Rouse number. Equation 1.42 assumes negligible molecular viscosity and is based on the following parabolic turbulent viscosity profile,

$$\nu_t = \kappa u_* y \left(1 - y/h \right).$$ (1.43)

Equation 1.43 is obtained by integrating the flow momentum equations for a uniform Steady-State (SS) channel flow and a logarithmic velocity profile. The sediment settling velocity is usually calculated the same way for snow using equation 1.2. According to Toorman [46], Equation 1.42 was first derived by Ippen in 1936 at the suggestion of Von Kármán, but it was named after Rouse who published it the subsequent year [47]. For incompressible flows, the phase density ratio is constant and the treatment above can be extended to volume fractions by replacing c_s and c_{sa} by α_s and α_{sa}, respectively.

Equation 1.42 has been successfully validated for many flows satisfying the assumptions behind it [48, 49], but with some important deviations from experimental data in some cases. Many corrections to the Rouse profile have been proposed to account for deviations from experimental data. It is shown that the corrected profiles can be generalised by adopting a power profile of arbitrary exponent for the $(1 - y/h)$ term in equation 1.43, and using a concentration dependent settling velocity [50, 51]. Such a settling velocity relationship is the Richardson-Zaki relationship [52],

$$\omega_s = \omega_0 (1 - \alpha_s)^m.$$ (1.44)

Here, ω_0 is the settling velocity of a single particle, and m is an empirical exponent determined by fitting experimental data. The generalised Rouse profile becomes the solution of the following equation [51],

$$\int_{\alpha_{sa}}^{\alpha_s} \frac{d\alpha_s}{\alpha_s (1 - \alpha_s)^m} = - \int_{\eta_a}^{\eta} \frac{Z_0}{\eta (1 - \eta)^n} d\eta.$$ (1.45)

Here, α_{sa} is the sediment volume fraction at the arbitrary reference height a, $Z_0 = \omega_0 / \kappa u_*$. n is an index based on data analysis and been defined as [53],

$$n = 1 + \beta \frac{c_s}{c_{sa}}. \tag{1.46}$$

Here, β is a constant that is determined by fitting profiles to experimentally measured velocity distributions, with values that can go from 0.5 to 40. The index n reflects the effect of water and sediment properties on the characteristic length for sediment vertical motion, which is a Lagrangian motion scale different from the Prandtl mixing length that relates to inertial turbulent scales. Using equation 1.46, Umeyama [54] was able to match two different sets of experimental data [49, 55].

For dilute conditions where $m = 0$ in equation 1.44, using $n = 0$ results in the Laursen formula [56],

$$\frac{\alpha_s}{\alpha_{sa}} = \left(\frac{\eta_a}{\eta} \right)^{Z_0}. \tag{1.47}$$

Taking $n = 1$ results in the Rouse formula from equation 1.42. Taking $n = 0.5$ results in the Tanaka-Sugimoto formula [57],

$$\frac{\alpha_s}{\alpha_{sa}} = \left(\frac{1+E}{1+E_a} \cdot \frac{1-E_a}{1-E} \right)^{Z_0}. \tag{1.48}$$

Here, $E = \sqrt{1-\eta}$ and $E_a = \sqrt{1-\eta_a}$. With $n = 0.8$, the Barenblatt formula is obtained [58],

$$\frac{\alpha_s}{\alpha_{sa}} = \left(\frac{E}{E_a} \cdot \frac{1-E_a}{1-E} \right)^{Z_0}. \tag{1.49}$$

Taking $m = 1$ and $n = 0.8$, a few judicious substitutions allow one to recover the equivalent of Hunt's formula [59] which accounts for the volume of suspended particles,

$$\frac{\alpha_s}{\alpha_{sa}} \cdot \frac{1-\alpha_{sa}}{1-\alpha_s} = \left[\frac{E}{E_a} \cdot \frac{B-E_a}{B-E} \right]^{Z_0}. \tag{1.50}$$

Here, B is defined as $0.995 < B < 1$.

Besides its limitation to SS fully developed flow regimes, the Rouse profile exhibits a singularity at the bottom, since $c \to \infty$ when $\eta \to 0$. This singularity originates from the derivation of the velocity gradient in the mixing length model equation 1.41 from a logarithmic profile that results in η in the denominator. This can be avoided by using a modified logarithmic profile [60],

$$u = \frac{u_*}{\kappa} ln \left(1 + \frac{y}{y_0} \right). \tag{1.51}$$

Here, y_0 is a measure of the bed roughness height. The turbulent viscosity becomes,

$$\nu_t = \kappa u_*(y + y_0) \cdot \left(1 - \frac{y}{h}\right). \tag{1.52}$$

The Rouse profile then becomes,

$$\frac{c_s}{c_{s0}} = \left(\frac{1 - y/h}{1 + y/y_0}\right)^{Z/(1+y_0/h)}. \tag{1.53}$$

Here, c_{s0} is the sediment concentration at y_0, which is now taken as the reference level. This modified Rouse profile is equivalent to the original one, except near the bed. The roughness model is also equivalent to that of Willis [61] who modifies the Rouse profile to account for a viscous sublayer of thickness y_0, with two different profile expressions for above and within the viscous sublayer.

In spite of its popularity, the Rouse formula remains a one-dimensional expression for SS and fully developed flow, with an idealised logarithmic or power law velocity profile that will surely fail in the presence of flow obstacles, or for developing flows. In addressing these limitations, Vanoni [62] lately stated that the Rouse formula can only represent the shape of the concentration distribution, not the actual values in a predictive accuracy. The same has been observed to various degrees in the published validations of the models discussed above.

Greimann *et al.* [63] follow a markedly different approach in that they start with a full E-E two-phase system, consisting of ensemble-averaged conitnuity and momentum equations for the fluid and sediment phases. They assume dilute conditions with one-way coupling to the water flow, which is modelled with a logarithmic velocity profile, and proceed to derive a sediment concentration transport equation for steady developed flow. One of their key assumptions is that the turbulence fluid-sediment correlation is equal to the turbulence fluid correlation. This likely overestimates the turbulence fluid-sediment correlation since sediment particles do not respond instantaneously to the fluid velocity field, and their turbulence intensity is generally smaller than that of the fluid. They retain only the drag and added mass forces, and eliminate lift since it can only be important close to the bed where little experimental data is available. Their sediment transport equation allows them to show that the increased diffusion of large particles is due to the diffusive nature of the vertical turbulent intensities in the sediment momentum equation, a previously unexplained phenomenon. They derive the following analytical equation for the sediment volume fraction,

$$\frac{\alpha_s}{\alpha_{sa}} = \left[\frac{\eta - \frac{1}{2}(1 + S')}{\eta - \frac{1}{2}(1 - S')} \cdot \frac{\eta_a - \frac{1}{2}(1 - S')}{\eta_a - \frac{1}{2}(1 + S')}\right]^{\frac{z}{S'}}, \tag{1.54}$$

where,

$$S' = \sqrt{1 + \frac{4C_v St_b}{\gamma_c \kappa}}. \tag{1.55}$$

Here, α_s is the sediment volume fraction at the non-dimensional height η, α_{sa} is the sediment volume fraction at the reference non-dimensional height η_a from the bed, C_v is a constant related to the vertical turbulent intensity that is assumed constant, γ_c is a coefficient accounting for crossing trajectory effects, and $z = \omega_s/(\gamma_c \kappa u_*)$ is the Rouse number corrected for cross trajectory effects. $St_b = \tau_p/\tau_{fb}$ is the bulk Stokes number where τ_p is the particle response time, and $\tau_{fb} = h/u_*$ is a bulk measure of the fluid's turbulent integral time scale. When $St_b = 0$, equation 1.54 reduces to the Rouse profile, an indication that the latter does not account for particle response times which becomes important for large particles. This aspect is highlighted by validations against the data of Einstein and Chien [55], Wang and Qian [64], and Taggart *et al.* [65]. The validations also show that the Rouse profile greatly underestimates the diffusion of large particles for $St_b/(\kappa y_0) = O(1)$. When $St_b/(\kappa y_0) \ll 1$ it is possible to derive a simple analytical solution of their differential equation for the lag velocity, namely the difference between the fluid and sediment velocities. This solution allows them to show that the sediment lag velocity is of the same order as the fall velocity, and decreases towards the surface. It should be noted that Greimann *et al.* [63] use the following definition of the phase-weighted relative velocity U_r,

$$U_r = U_s - U_w - U_d. \tag{1.56}$$

Here, U_s and U_w are respectively the sediment and water phase-weighted average velocities, and U_d is the phase-weighted average drift velocity. U_d is due to the correlation between the particle distribution and the water turbulent velocity, and accounts for the dispersion effect due to particle transport by fluid turbulence.

$$U_d = \frac{1}{\alpha_s} \langle u'_w \rangle_s. \tag{1.57}$$

Here, $\langle . \rangle_s$ is the ensemble average operator for phase s. U_d can also be calculated using the particle turbulent time scale, gradients of volume fractions, and the turbulent dispersion tensor [66]. This model is based on the work of He and Simonin [67] who do not use other turbulent dispersion mechanisms, and define the drag force F_D as follows,

$$F_D = \frac{3}{4}\frac{C_d}{d_p}|u_r|. \tag{1.58}$$

Here, C_d is the drag coefficient, and u_r is the instantaneous relative velocity with its magnitude defined as,

$$|u_r| = \sqrt{U_r U_r + \langle u_r' u_r' \rangle_s}. \tag{1.59}$$

u_r' is the relative velocity fluctuation. Therefore, the drag turbulent fluctuations are implicitly included in equation 1.58. However, it should be noted that other formulations of sediment transport based on two-phase flow models similar to the Greimann model do not use the drift velocity in the determination of the relative velocity, even though they do not have any turbulent dispersion mechanisms either [68, 69].

Jiang *et al.* [70] use the Particle Group Model (PGM), which is a simplified set of two-phase flow equations that can be derived from the basic multiphase flow equations under the assumption of suspension conditions [71]. In the PGM the control volume is chosen such that its outer surfaces consist only of fluid. This restricts fluid-sediment interactions to inter-phase momentum exchange terms within the control volume, which consist of the molecular pressure, laminar drag, and turbulent drag forces. The drag forces are defined in relation to the velocity differences between the phases and the phases time scales, which they claim makes them better adapted to flow changes. This is in contrast to Greimann *et al.* [63] who use empirical coefficients that are subject to change in different parts of the flow [72]. They derive the following one-dimensional sediment concentration profile,

$$\begin{aligned}
\frac{\alpha_s}{\alpha_{sa}} = &\left(\frac{1-\eta}{\eta} \cdot \frac{\eta_a}{1-\eta_a} \right)^{\omega_s/(D_s \kappa u_*)} \\
&\times \exp\left[\frac{1.34(1-D_s)}{D_s} \cdot (\eta_a - \eta) \right] \\
&\times \exp\left[\frac{1.34 C_v St_b D_w}{D_s \kappa} \cdot \left(1 - \frac{\rho_w}{\rho_s} \right) \cdot (f(\eta_a) - f(\eta)) \right].
\end{aligned} \tag{1.60}$$

Here, D_s is the sediment damping coefficient, typically less than 1, $C_v = 1.51$ is an empirical parameter related to the distribution of fluid turbulence intensity in clear water open channel flows [73], D_w is the fluid damping coefficient that is close to unity for dilute flows, ρ_w and ρ_s are the water and sediment densities, respectively. The function $f(\eta)$ is given by,

$$\begin{aligned}
f(\eta) = &\exp(-1.34) \times \left[ln(1-\eta) + 1.34(1-\eta) \frac{(1.34(1-\eta))^2}{2 \times 2!} + \frac{(1.34(1-\eta))^3}{3 \times 3!} \right] \\
&- \left[ln(\eta) - 1.34\eta + \frac{(1.34\eta)^2}{2 \times 2!} - \frac{(1.34\eta)^3}{3 \times 3!} \right].
\end{aligned} \tag{1.61}$$

For small particles and dilute flows, particle inertia effects can be ignored ($D_s = 1$) and $St_b \ll 1$. In this case the two exponential terms on the Right Hand Side (RHS) of equation 1.60 can be ignored, leading to the Rouse profile. Jiang *et al.* [70] develop as well a

one-dimensional expression for the velocity lag, namely the difference between the water and sediment velocities. Validation of the above profile against experimental sediment concentration measurements in a uniform channel flow [74] show better agreement than the Rouse profile and the concentration profile model of Greimann above. Validation of the velocity lag against experimental measurements of velocity profiles in open-channel flow with suspended sediment [75] show better agreement in the trend than the Greimann velocity lag model.

1.2.2 Numerical Models of Sediment Concentration Transport

The analytical methods discussed above are restricted to simplified one-dimensional and SS fully-developed flows. They also use simple 0-equation turbulence models, such as the logarithmic velocity profile with mixing length hypothesis for the turbulent viscosity. As such, they cannot analyse two- and three-dimensional flows with strong curvature and substantial developing regions, as in meandering channels and around bridge components. In such situations, which are normally transient, one must resort to numerical models based on the Finite Difference Method (FDM), Finite Element Method (FEM), and Finite Volume Method (FVM). Numerical models also allow one to use more accurate turbulence models with transport equations for the relevant turbulence quantities, and two-phase formulations with better modelling of the interactions between the phases. The numerical models of sediment concentration transport are not unlike those used for drifting snow, discussed at length in section 1.1. The one salient difference is that modelling of sediment concentration transport is often concerned with tracking the free interface at the water surface, in addition to tracking the free interface at the sediment bed, which is similar to the snowbed interface tracking. Below, several numerical two- and three-dimensional models for simulating the transport of sediment concentration are discussed. The models are divided in two broad categories, those that do not track the free water surface and those that do.

1.2.2.1 Numerical Sediment Concentration Transport Without Free Water Surface Tracking

Van Rijn [76] presents a SS two-dimensional model (SUTRENCH-2D) for simulation of sediment concentration transport of suspended particles larger than about $50\,\mu\mathrm{m}$ in non-stratified free surface flows. The sediment concentration is assumed dilute enough to be one-way coupled to the water flow. The full details of the formulation are provided in [77], and a quick overview of it is given below. The starting sediment concentration transport equation is,

$$\nabla \cdot (\mathbf{u}_w - \delta_{j3}\omega_s)c_s = \nabla \cdot \left(\nu_{ts}\delta_{j3}\nabla c_s\right). \tag{1.62}$$

Here, ν_{ts} is the sediment turbulent diffusivity. Furthermore, the particle fall velocity is assumed constant. For reasons of computational efficiency, the water velocity calculations are done using a simplified profile formulation, which consists of a linear combination of a logarithmic velocity profile and a perturbation due to the pressure gradients [78]. Such a profile is derived by fitting experimental data specific to the flow and channel shape being analysed, and applies strictly to SS fully-developed flows. Assuming linear shear stress over depth the fluid turbulent viscosity can be defined using a parabolic-constant profile [79],

$$\begin{aligned} \nu_t &= \nu_{t,max}\left[1 - \left(1 - \frac{2z}{h}\right)^2\right] \qquad &&\text{for} \qquad \frac{z}{h} < 0.5, \\ \nu_t &= \nu_{t,max} &&\text{for} \qquad \frac{z}{h} \geq 0.5. \end{aligned} \tag{1.63}$$

Here, the maximum turbulent viscosity $\nu_{t,max}$ is calculated as,

$$\nu_{t,max} = \frac{\kappa u_* h}{4}. \tag{1.64}$$

The turbulent viscosity profile is not assumed fully-developed. Instead, its variation streamwise is indirectly computed using the following first order Ordinary Differential Equation (ODE) for $\nu_{t,max}$,

$$\frac{d\nu_{t,max}}{dx} = \left[\frac{\alpha_4}{h}\nu_{t,max}^e - \nu_{t,max} - \alpha_5 h\frac{d(u_{wh} - \overline{u}_w)}{dx}\right]e^{-15\frac{dh}{dx}}. \tag{1.65}$$

Here, $\alpha_4 = 0.05$ and $\alpha_5 = 0.015$ are calibration constants, $\nu_{t,max}^e$ is the maximum turbulent viscosity at equilibrium, u_{wh} is the water velocity at the free water surface, and $\overline{u}_w$ is the water velocity average over the cross-section at the streamwise distance x. The final piece of the model is the mass-balance equation used to calculate the bed-level changes,

$$b\frac{\partial z_b}{\partial t} + \frac{1}{1 - \varepsilon}\left(b\frac{\partial h\overline{c}_s}{\partial t} + \frac{\partial S}{\partial x}\right) = 0. \tag{1.66}$$

Here, $z_b(x)$ is the streamwise varying bed-level, ε is the bed porosity, and $\overline{c}_s$ is the depth-averaged sediment concentration calculated as,

$$\overline{c}_s = \frac{1}{h}\int_{z_b+a}^{z_b+h} c_s dz. \tag{1.67}$$

$S = S_s + S_b$ is the cross-section integrated total sediment load, calculated as the sum of the suspended and bed loads, respectively. S_s is calculated as,

$$S_s = b\int_{z_b+a}^{z_b+h} ucdz. \tag{1.68}$$

S_b is calculated as,

$$S_b = 0.1b(\Delta g)^{0.5} D_{50}^{1.5} \frac{\overline{T_m^{2.1}}}{D_*^{0.3}}. \tag{1.69}$$

Here, Δ is the bed-form height, D_{50} is the sediment size distribution median diameter, and D_* is a non-dimensional sediment particle diameter defined as,

$$D_* = D_{50} \left[\frac{(s-1)g}{\nu_w^2} \right]^{1/3}. \tag{1.70}$$

Here, ν_w is the water kinematic viscosity, and s is the sediment specific density with respect to water,

$$s = \frac{\rho_s - \rho_w}{\rho_w}. \tag{1.71}$$

In equation 1.69, $\overline{T_m^{2.1}}$ is calculated using a stochastic procedure described by Van Rijn [80].

The SUTRENCH-2D model is validated against four experimental cases. The first case consists of the transport of sediment concentration in a horizontally uniform fully-developed flow over a perforated bottom [81] (used for the validation of section 1.2 as well). Reasonably good agreement was obtained for comparisons of the computed and measured sediment concentration profiles over the entire flume length, with increasing deviations from experimental measurements in the downstream direction. The agreement was worst near the water surface and the bottom. The comparisons of depth-averaged sediment concentrations showed good agreement only at the flume inlet and outlet, with large deviations from measured measurements in between. No comparisons were made to the measured water velocity profiles.

The second experiment consists of the migration of a trench in a flume [82], with three different trench inlet and outlet slopes. The measurements taken were flow velocity and sediment concentration profiles, and bed level changes, all in the centre plane of the flume. The experimental inlet conditions were maintained at equilibrium, but in the flume the flow decelerated in the downstream direction. Computed and measured concentration and velocity profiles are compared for the trench with the steepest inlet and outlet slopes (1:3), and a downward sloping bed in the downstream direction. The reported computed values were section-averaged. The concentration profile comparisons are reasonably good for the equilibrium profiles in the outlet section out of the trench, and in the middle of the trench. Other locations show substantial deviations in concentration between measurements and numerical results. The velocity profile comparisons are good in the equilibrium inlet section, and right after the trench inlet. Reasonable agreement is noted in the other locations. Comparisons of computed and measured bed level show reasonably good agreement for all three trench slopes, with the best agreement observed for the shallower slopes. The best agreement for all three slopes is always observed in the

middle of the trenches.

The third experiment consists of sedimentation field verification in an uneven pipe-line trench dredged in a tidal estuary in The Netherlands [83]. This trial trench was dredged perpendicular to the tide in order to estimate the sedimentation rate. Flow velocity and sand concentration profiles were measured to determine the suspended load transport rates. Comparisons of computed and measured velocity profiles showed reasonable agreement with the trends well predicted.

The fourth experiment consists of sedimentation and erosion trials carried out in 1983 in a dredge channel in the Asan Bay, South Korea. Comparisons of computed and measured bed level changes over 100 days showed reasonable agreement over the width of the uneven channel, with the largest deviations in the central region where the current velocity is believed to have been underpredicted.

Demuren and Rodi [84] develop a fully three-dimensional SS method to simulate the transport of pollutant concentration in meandering channels. Their model consists of the incompressible Navier-Stokes equations, the pollutant concentration transport equation, and the $k - \epsilon$ turbulence model equations, all in cylindrical polar coordinates. Their pollutant concentration transport equation is,

$$\frac{1}{r}\frac{\partial rU_r c_p}{\partial r} + \frac{\partial U_y c_p}{\partial y} + \frac{1}{r}\frac{\partial U_\theta c_p}{\partial \theta} = \frac{1}{r}\frac{\partial}{\partial r}\left(\frac{\nu_t}{\sigma_c}r\frac{\partial c_p}{\partial r}\right) + \frac{\partial}{\partial y}\left(\frac{\nu_t}{\sigma_c}\frac{\partial c_p}{\partial y}\right). \qquad (1.72)$$

Here, r is the radial coordinate, y is the vertical coordinate, θ is the azimuthal angle coordinate, and σ_c is the turbulent Schmidt number for pollutant concentration. The authors use $\sigma_c = 0.5$ based on previous calculations of pollutant dispersion in open channels [85, 86]. It is not specified whether the pollutant concentration c_p is a mass or volume fraction, but this has little impact on the findings of the study. The reason is that Equation 1.72 has exactly the same form for either variable, and the concentration profile validations are done in terms of depth-averaged concentration ratio to the average concentration. The turbulence model used is the standard $k - \epsilon$ model in polar cylindrical coordinates, which does not account for streamline curvature effects. However, the authors claim that since pressure gradients are larger than Reynolds stresses gradients in meandering flows, and since the pressure gradient does not appear in the pollutant concentration transport equation, it is enough to account for curvature effects through a modified C_μ [87],

$$C_{\mu,r} = \frac{0.09}{1 + 0.57\dfrac{k^2}{\epsilon^2}\left(\dfrac{\partial U_{hol}}{\partial n} + \dfrac{U_{hol}}{R}\right)\dfrac{U_{hol}}{R}}. \qquad (1.73)$$

Here, U_{hol} is the water horizontal velocity, n is the distance in the direction normal to U_{hol}, and R is the streamline local radius of curvature. In this model, the water surface is treated as a symmetry plane, with velocity components normal to it and normal gradients

of all variables set to zero. Such a surface is also referred to as a "rigid lid".

The above model was used to simulate three meandering experiments with channel width-to-depth ratios of 4–20, smooth and rough beds, and different pollutant discharge locations [88, 89]. The velocity and concentration fields showed good agreement with the experimental measurements in general, with significant three-dimensional effects present. The effect of streamline curvature was found to be significant for narrow channels with smooth beds only. For wide channels with smooth beds, and narrow channels with rough beds, the curvature effect was counterbalanced by turbulence generated at the bed. Finally, the three-dimensional solutions showed the presence of a single large eddy at most cross-sections for the latter two channel configurations. As for the narrow channel with a smooth bed, the simulations showed the presence of more than one eddy at most cross-sections in general. This method was later extended to the calculation of suspended sediment transport in meandering channels [90]. A simple model for bed-load transport was later added [90] and validated against flow and sediment transport measurements in a 180° laboratory channel bend [91].

1.2.2.2 Numerical Sediment Concentration Transport With Free Water Surface Tracking

Apart from the water-sediment interface, sediment transport simulation is also concerned with capturing the free interface between water and air. The free air-water interface represents a physical barrier to sediment transport, and provides additional mechanisms for sediment transport and resuspension from the sediment bed through wind-induced wave formation. Such mechanisms are quite relevant for estuaries, lakes, and large bodies of water, with Green and Coco [92] providing a good review on the subject. At a wavy water surface, the water moves in a circular orbital motion when a wave passes. Orbital motions under even very small waves, less than 20 cm high, have been shown to resuspend sediments on intertidal flats, the area under tidal influence between open sea and land [93–96]. This is made possible through the increase in bed shear stress by the orbital motions. Episodic sediment resuspension by waves can even exceed periodic resuspension by currents up to a factor of 5 [97]. During storms, which are wave-dominated systems, an order of magnitude increase can be observed in suspended sediment concentration compared to during clement weather, a tide-dominated system [98]. In mesotidal situations where the tide range is 2 to 4 m, and tidal currents are incapable of resuspending sediments, resuspension can be completely controlled by episodic waves [99]. Conversely, Christie and Dyer (1998) wave transport of suspended sediment on intertidal flats can be about 2 orders of magnitude smaller than tidal transport for calm weather and small waves [100].

For water surfaces that are relatively gentle one can simply use a rigid moving wall approximation, the level of which can be calculated using 1D or 2D models. Otherwise,

surface tracking methods can be used, based on the free surface kinematic condition,
with adaptive mesh refinement to follow the free surface. The water level can also be
obtained from a 2D Poisson equation derived from the 2D depth-averaged momentum
equations, with a two-layer sediment transport model for the suspended load layer and
the bed load layer [101]. Transport in the bed load layer is represented with a sediment
mass balance equation based on steady-state equilibrium conditions. In the suspended
load layer, a transient convection-diffusion equation of the sediment concentration is used
that includes turbulent diffusion on the right hand side, akin to a classical scalar transport
equation. The net flux of sediment is imposed as a boundary condition between the two
layers, and is calculated as the difference between deposition rate due to settling velocity
and equilibrium entrainment rate. At the free surface a boundary condition of zero vertical
sediment flux is applied. Wu *et al.* [101] show their model to be at least as accurate as
other methods for simulations of net entrainment from a loose bed experiment [102], and
a suspended load experiment with zero entrainment at the bed [81]. Zeng *et al.* [103] use
a 3D turbulent hydrodynamic model with a convection-diffusion equation of the sediment
concentration, and a movable grid model to account for morphological bed changes. The
convection-diffusion equation model assumes low drift between the suspended sediment
phase and the water flow and is appropriate for small particles with negligible inertia
compared to the water phase. In general, they show order of magnitude agreement with
sediment suspension experimental results by Wang and Ribberink [81].

Volume tracking methods such as the VOF method are also used to track the free
surface in sediment scour simulations [104–106]. The VOF method allows tracking the
interface in a continuous manner but loses accuracy where sharp gradients of the volume
fraction exist, requiring special treatments such as adaptive mesh refinement [107], com-
pressive discretization schemes such as the Compressive Interface Capturing Scheme for
Arbitrary Meshes (CICSAM) [108], or the explicit Multidimensional Universal Limiter
with Explicit Solution (MULES) model [109]. Lately, Røenby *et al.* [110] introduced the
`isoAdvector` model which reconstructs the interface within cells geometrically using an
isosurface concept. Sediment transport by suspension is modelled in the VOF method
using the same type of transient convection-diffusion equation for sediment concentration
transport used by Wu *et al.* [101], Liu and [G]arcía [105], and Zeng *et al.* [103]. The for-
mulation used by Sattar *et al.* [106] is provided below since their results will be compared
to later. The air-water flow is accounted for by the hydrodynamic module of Jasak *et al.*
[111], consisting of the following balance equations,

$$\nabla \cdot \mathbf{u}_m = 0, \tag{1.74}$$

$$\frac{\partial \alpha_w}{\partial t} + \nabla \cdot (\mathbf{u}_m \alpha_w) + \nabla \cdot (\mathbf{u}_r \alpha_w (1 - \alpha_w)) = 0, \tag{1.75}$$

$$\frac{\partial(\rho_m \mathbf{u}_m)}{\partial t} + \nabla \cdot (\rho_m \mathbf{u}_m \mathbf{u}_m) = \nabla \cdot \mu_{eff} - \nabla p_d - (g \cdot \nabla \rho_m). \tag{1.76}$$

Here, α_w is the volume fraction of water, $\mathbf{u}_m = \alpha_w \mathbf{u}_w + \alpha_a \mathbf{u}_a$ is the mixture velocity, $\rho_m = \alpha_w \rho_w + \alpha_a \rho_a$ is the mixture density, p_d is the dynamic pressure, and μ_{eff} is the effective dynamic viscosity from turbulence modelling. The relative velocity $\mathbf{u}_r$ is given by,

$$\mathbf{u}_r = \frac{\nabla \alpha_w}{|\nabla \alpha_w|} \frac{C_\alpha}{\Delta x \Delta t}. \tag{1.77}$$

Here, C_α is a target compressive surface Courant number, Δx is the computational cell size, and Δt is the time step. This approach allows for interface compression independent of the flow Courant number and time step, with the implementation details available in [111].

The sediment transport module consists of the suspended sediment transport equation 1.38. Additionally, the change in bed height can be calculated from the following balance equation integrated over the water depth [101],

$$(1 - \varepsilon) \frac{\partial \eta}{\partial t} + \nabla_s \cdot \mathbf{q}_b + E_b - D_b = 0. \tag{1.78}$$

Here, ε is the bed porosity, and E_b is the entrainement rate calculated as,

$$E_b = \omega_s c_b^*. \tag{1.79}$$

Here, c_b^* is the equilibrium concentration that can be obtaind from the following relationship [112],

$$c_b^* = 0.015 \frac{v_w^2 \rho_w D_{50}^{0.6} \left(\frac{u_{*,eff}^2 - u_{*t}^2}{u_{*t}^2} \right)^{1.5}}{g(\rho_s - \rho_w) K_s}. \tag{1.80}$$

Here, $u_{*,eff}$ is the effective friction velocity, and K_s is the roughness height taken as $5\,\%$ of the water depth from the bed. In equation 1.78, D_b is the deposition of sediment flux calculated as,

$$D_b = \omega_s c_b. \tag{1.81}$$

Here, c_b is the sediment concentration just above the saltation layer, at the top of the roughness element [113]. $\mathbf{q}_b$ is the bed load transport rate given by [105],

$$\mathbf{q}_b = q_b \frac{\tau_b}{|\tau_b|} - C|q_b| \cdot \nabla_s \eta. \tag{1.82}$$

Here, τ_b is the bed surface shear stress vector calculated from the hydrodynamic module,

C is a constant accounting for the bed slope effect with an average value of 2.0 [114], ∇_s is the surface gradient, and η is the bed elevation. q_b is the flat bed scalar transport rate given by [115],

$$q_b = \begin{cases} 18.74\sqrt{sgD_{50}^3}(\theta - \theta_t^*)(\theta^{0.5} - 0.7\theta_t^{*0.5}) & \text{for } \theta > \theta_t^*, \\[2mm] 0 & \text{otherwise.} \end{cases} \tag{1.83}$$

Here, the Shields number θ is calculated as,

$$\theta = \frac{\tau_b}{sg\rho_w D_{50}}. \tag{1.84}$$

The threshold Shields number θ_t^*, adjusted to the bed slope β, is given by [105],

$$\theta_t^* = \theta_t\left(cos\beta\sqrt{1 - \frac{sin^2\phi tan^2\beta}{\mu_s^2}} - \frac{cos\phi sin\beta}{\mu_s}\right). \tag{1.85}$$

Here, ϕ is the angle between the velocity vector and bed steepest slope direction [105], and μ_s is a friction coefficient set to 0.65. It should be noted that Sattar *et al.* use the critical Shields number terminology, which is replaced here with threshold Shieds number to be consistent with the drifting snow terminology. Sattar *et al.* do not mention how they determine the threshold Shields number θ_t, but it can be done as follows according to Shields *et al.* [116],

$$\theta_t = \frac{u_{*t}^2}{(\rho_s/\rho_w - 1)gD_{50}}. \tag{1.86}$$

Here, ρ_s is the sediment density, and u_{*t} is the threshold friction velocity for onset of sediment motion. It can be determined from the Shields diagram, which relates θ_t to the non-dimensional particle diameter D_* from equation 1.70.

1.3   Solid Particle Phase Viscosity Models

In the general context of two-phase flows, researchers usually resort to empirical or theoretical expressions of the mixture viscosity [117–122], and calculate the dispersed phase viscosity using equation 1.27. The first theoretical expression of mixture viscosity is by Einstein [117, 118] who derived it for spherical particles in a flow dilute enough so that the particles do not feel their mutual hydrodynamic effects ($\alpha_1 < 0.03$, where α_1 is the dispersed phase volume fraction). It relates the mixture dynamic viscosity μ_m to the continuous phase dynamic viscosity μ_2 as follows,

$$\mu_m = \mu_2(1 + 2.5\alpha_1 + O(\alpha_1)). \tag{1.87}$$

The Einstein expression was later extended independently by Brinkman [119] and Roscoe [120] to dilute flows with spherical particles of very diverse sizes, and for all concentrations. Their mixture viscosity expression is,

$$\mu_m = \mu_2(1 - \alpha_1)^{-2.5}. \tag{1.88}$$

For spherical particles of equal sizes and medium to high concentrations, Roscoe [120] also provides the following expression,

$$\mu_m = \mu_2(1 - 1.35\alpha_1)^{-2.5}. \tag{1.89}$$

Equation 1.89 implies that a suspension carrying a high concentration of uniform spherical particles is equivalent to a suspension of spherical particles of very diverse sizes, but a concentration 35 % higher. This follows from Vand's argument that as the particle concentration is increased, many particles tend to aggregate together until a certain concentration where nearly all particles are combined in larger tightly packed clusters of roughly spherical form [123]. The factor of 1.35 follows from geometric packing considerations. At low concentrations, equations 1.88 and 1.89 give similar results.

Ishii [121] provides the following mixture viscosity expression for all concentrations, based on the same considerations behind equation 1.89 and taking into account $\alpha_{1,max}$ the maximum packing of the particles,

$$\mu_m = \mu_2 \left(1 - \frac{\alpha_1}{\alpha_{1,max}}\right)^{-2.5\alpha_{1,max}(\mu_1 + 0.4\mu_2)/(\mu_1 + \mu_2)}. \tag{1.90}$$

For particle viscosities $\mu_1 \gg \mu_2$, which is normally the case of solid particle-laden flows, the expression above reduces to,

$$\mu_m = \mu_2 \left(1 - \frac{\alpha_1}{\alpha_{1,max}}\right)^{-2.5\alpha_{1,max}}. \tag{1.91}$$

Equation 1.91 above was tested and confirmed to yield identical results to equation 1.90, except for a very narrow margin of volume fraction in the densest part of the flow where $\alpha_1 > 0.1$. Since $\alpha_1 < 0.1$ for the most part of the flows simulated in this thesis, equation 1.91 is the one retained for the ensuing viscosity model validation due to its simplicity.

Graham [122] derives a mixture viscosity model using spherical cell theory to assess the energy dissipation rate of the continuous phase in a two-phase situation, compared to the energy dissipation rate of a hypothetical single-phase fluid under the same macroscopic flow conditions. The derivation assumes cubic packing of the spherical particles and leads to the following expression valid at all particle concentrations,

$$\mu_m = \mu_2 \left(\frac{9}{4}\left[\frac{1}{1 + 0.5\psi}\right]\left[\frac{1}{\psi} - \frac{1}{1 + \psi} - \frac{1}{[1 + \psi]^2}\right] + 1 + 2.5\alpha_1\right). \tag{1.92}$$

Here, the parameter ψ is given by,

$$\psi = \left(\frac{\alpha_{1,max}}{\alpha_1}\right)^{1/3} - 1. \tag{1.93}$$

A notable exception to the mixture viscosity approach is the CC dispersed phase viscosity model for fluidised beds with large solid to gas density ratio [124], reported by Murray [125]. This viscosity model was obtained by Murray from an unpublished Los Alamos report by the original authors, and its details and validity range are not available. The brief derivation reproduced by Murray in his appendix is based on the ratio of distortion (essentially strain) of a single-phase fluid to the same sheared fluid with particles present. The CC model does not seem to be specifically developed for fluidized beds situations, so it is reported here. It consists of the following expression for the particle dynamic viscosity,

$$\mu_1 = \mu_2 A_{cc} \frac{d_p}{2h}. \tag{1.94}$$

Here, A_{cc} is a constant reported by the model authors to be of order $O(1)$, d_p is the particle diameter, and h the shortest distance between the outer circumferences of neighbouring particles (see Figure 1.3). Based on geometric considerations, h can be defined as follows from the particle diameter and volume fraction,

$$h = \frac{d_p}{2}\left(\sqrt[3]{\frac{\pi}{6\alpha_1}} - 1\right). \tag{1.95}$$

Based on this result, the CC model becomes,

$$\mu_1 = \mu_2 \frac{A_{cc}}{\sqrt[3]{\frac{\pi}{6\alpha_1}} - 1}. \tag{1.96}$$
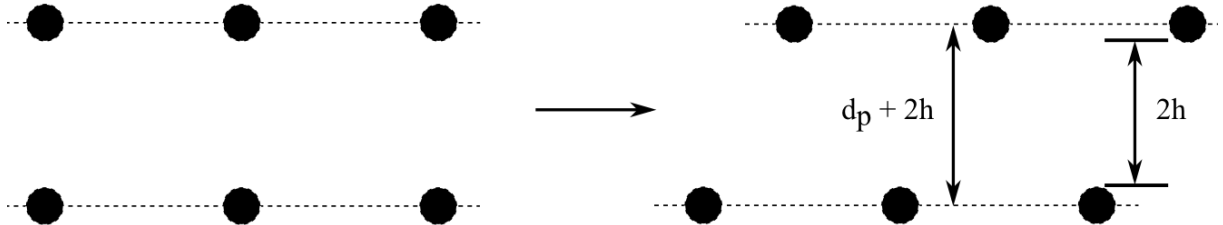
Figure 1.3: Reproduction of the sheared (right side) particle-laden flow configuration used to explain the viscosity relationship of Carrier and Cashwell.

Kazhikov and Smagulov [126] also propose a particle viscosity model. The original Russian paper is not available, so the description below is taken from Dutykh *et al.* [127] instead. The KS model consists of the following expression for the particle viscosity μ_1,

$$\mu_1 = \mu_0 e^{-aT} e^{\beta \rho_1}. \tag{1.97}$$

Here, $\mu_0 = 3.6 \times 10^6 \text{ kg} \cdot \text{m}^{-1} \cdot \text{s}^{-1}$, $a = 0.08 \text{ K}^{-1}$, and $\beta = 0.021 \text{ m}^3 \cdot \text{kg}^{-1}$.

In the context of settling snow, many compactive viscosity models are available for very low rates of strain, the latest by Teufelsbauer [128] including a short review of the main models in the literature. However, nothing is available at the high rates of strain of saltating and suspended particle phase.

1.4 Discussion and Proposed Approach

Both TSD and VOF models examined do not achieve better than order of magnitude agreement with experimental measurements of snowdrift levels around bluff bodies, and experimental measurements of sediment bed height. This is attributed to the fact that neither model resolves the saltation layer, relying instead on empirical equilibrium relationships to estimate the saltation transport. Such relationships were developed for fully-developed flows away from the acceleration and deceleration effects of flows near bluff bodies. Moreover, the two-phase flow in the saltation layer is known to be two-way coupled, where the airflow or water velocity is affected by the saltating particles. However, both TSD and VOF models are one-way coupled formulations, and can be derived from the more general two-way coupled E-E formulation. It seems then logical to resolve the saltation layer with two-way coupling, as opposed to modelling it with one-dimensional equilibrium formulations and one-way coupling.

The two-fluid model is an E-E two-way coupled system where each phase is treated as a continuum and both phases are interpenetrating. One such solver is `twoPhaseEulerFoam`, within the opensource C++ toolkit OpenFOAM® [109, 129]. Since `twoPhaseEulerFoam` is an open-source code, it can be easily modified to allow simulation of drifting snow and sediment transport.

The E-E fluid model requires a viscosity property for the viscous stress tensor, so a particle phase viscosity model for high rates of strain typical of saltation and suspension is developed and implemented.

1.4.1 Thesis Layout

In what follows, a two-way coupled model for simulating particle-laden flows, based on the two-fluid model, is presented in Chapter 2. It consists of the standard two-fluid equations with turbulent drag. A novel Eulerian solid particle phase viscosity model is also presented in section 2.3.

The validation of the particle-laden flow model is carried out in three parts. In Chapter 3 we present simulation results of a controlled wind tunnel saltating drifting snow exper-

iment, at a solid to fluid phase density ratio of order $O(100)$. In Chapter 4 we present simulation results of a controlled flume experiment of suspended sediment transport, at a solid to fluid phase density ratio of the order of $O(1)$. The suspended sediment simulations are also compared to the results of a VOF formulation. The two sets of simulations are complementary in that they address both extremes of the solid to fluid density ratio, both saltating and suspended transport regimes, as well as polydisperse and monodisperse particle distributions. In Chapter 5 we present validation results for the solid particle phase viscosity model for both drifting snow and suspended sediment.

1.4.2   Scientific Contributions

The main scientific contributions of this thesis are the following:

1. a two-way coupled model for computing particle laden saltating and suspended flows, for all flow regimes, and without the limitations of equilibrium empirical treatments;

2. a particle phase viscosity model for very high rates of strain, typical of creep, and saltation;

3. corrections to the KS particle phase viscosity model, consisting of a multiplicative constant of 0.1, and a volume fraction correction to the exponential density term, for dense drifting snow;

4. a multiplicative constant equal to the local phase density ratio for the CC particle viscosity model for dense drifting snow.

Chapter 2

Physical Model

2.1 The Two-Way Coupled Formulation

The formulation of `twoPhaseEulerFoam` is based on the Gosman multiphase flow model for interpenetrating phases [130], itself derived from the Ishii formulation [131]. In the introduction, subscript s designates the snow phase, and subscript a the air phase. Here, the notation consistent with `twoPhaseEulerFoam` version 2.2.x is used, where subscript 1 designates the snow phase, and subscript 2 the air phase.

The model consists of the following conditional ensemble-averaged equations of conservation of mass and linear momentum,

$$\frac{\partial \alpha_i}{\partial t} + \nabla \cdot (\alpha_i \mathbf{u}_i) = 0, \tag{2.1}$$

$$\frac{\partial}{\partial t}(\alpha_i \mathbf{u}_i) + \nabla \cdot (\alpha_i \mathbf{u}_i \mathbf{u}_i) + \nabla \cdot (\alpha_i \mathbf{R}_i) = -\frac{\alpha_i}{\rho_i}\nabla p + \alpha_i \mathbf{g} + \frac{\mathbf{M}_i}{\rho_i}. \tag{2.2}$$

Here, α_i, ρ_i, $\mathbf{u}_i$ and $\mathbf{R}_i$ are the volume fraction, density, velocity and stress tensor of phase i, respectively. p is the static pressure field, and $\mathbf{g}$ is the gravitational acceleration vector. $\mathbf{M}_i$ is the momentum exchange term between the phases which is defined as,

$$\mathbf{M}_i = \mathbf{F}_l + \mathbf{F}_d + \mathbf{F}_t + \mathbf{F}_{vm}. \tag{2.3}$$

Here, $\mathbf{F}_l$, $\mathbf{F}_d$, $\mathbf{F}_t$, and $\mathbf{F}_{vm}$ are respectively the aerodynamic lift, generalized drag, turbulent drag, and virtual mass forces. The present approach is to explicitly define a turbulent drag term, as opposed to others who use a drift velocity term in the relative velocity definition (see equation 1.56), and define it based on the continuous phase turbulent velocity fluctuations (see equation 1.57). Using scale analysis, Gauer [132] found the aerodynamic lift and drag forces to dominate at the onset of drifting, but did not consider the turbulent drag force. An earlier scale analysis by Gosman *et al.* [130] including the turbulent drag force found the lift to be negligible for gas/solid particle-laden flows, where the ratio of continuous gas density to dispersed solid density is proportional to 10^{-3}. The

lift force is given by,

$$\mathbf{F}_l = \alpha_2 \alpha_1 (\alpha_2 C_{l1} \rho_2 + \alpha_1 C_{l2} \rho_1) \mathbf{u}_r \times \nabla \times \mathbf{u}_m \tag{2.4}$$

Here, $\mathbf{u}_m = \alpha_2 \mathbf{u}_2 + \alpha_1 \mathbf{u}_1$ is the mixture velocity, and $\mathbf{u}_r = \mathbf{u}_2 - \mathbf{u}_1$ is the relative velocity between the phases. It should be pointed out that some relative velocity definitions like equation 1.56 include the particle phase drift velocity in the calculation of the reference velocity. This refinement seems unnecessary here since turbulent particle dispersion is accounted for in the turbulent drag term, which is elaborated on below. Numerical tests with the present model confirmed the lift force to be negligible, therefore it was not used in the present simulations. The only two forces found relevant for saltation and suspension are then the generalized and turbulent drag forces. The latter force was also reported to be the main mechanism for transporting smaller particles into suspension [1]. The generalized drag model used is the Gidaspow-Schiller-Naumann model [133], which is expressed as follows for the snow phase,

$$\mathbf{F_d} = K\mathbf{u}_r, \tag{2.5}$$

$$K = \frac{3}{4d_p} \rho_2 C_D \alpha_1 \alpha_2^{-1.65} |\mathbf{u}_r|. \tag{2.6}$$

C_D is the drag coefficient on a single sphere given by the following relationship [134],

$$C_D = \begin{cases} \dfrac{24}{Re_p}(1 + 0.15 Re_p^{0.687}) & \text{if } Re_p < 1000, \\[2mm] 0.44 & \text{if } Re_p \geq 1000. \end{cases} \tag{2.7}$$

Re_p is the particle Reynolds number based on the particle diameter d_p and air kinematic viscosity ν_2,

$$Re_p = \frac{\alpha_2 |\mathbf{u}_r| d_p}{\nu_2}. \tag{2.8}$$

The Gidaspow-Schiller-Naumann drag model is valid for dilute flows with $\alpha_2 > 0.8$ [135], which is the case in the creep, saltation and suspension layers. Moreover, the Gidaspow-Schiller-Naumann drag model applies to spherical particles and is used here since no practical correlations for irregular particles such as depicted in Figure 3.4 are available in the literature. However, as the present irregular particles drift they will rotate within a somewhat spheroidal volume of air around the particle's centre of mass. Their drag function could then be similar to that of a spherical particle with differences that cannot be predicted at the moment. It remains that the spherical particle drag correlations are

the only present recourse. The virtual mass force expression is the following [136],

$$F_{vm} = \alpha_1\alpha_2(\alpha_1 C_{vm2}\rho_1 + \alpha_2 C_{vm1}\rho_2)\left(\frac{d_2\mathbf{u}_2}{dt} - \frac{d_1\mathbf{u}_1}{dt}\right). \tag{2.9}$$

Here, C_{vm1} and C_{vm2} are constant coefficients and the transient terms are given by,

$$\frac{d_i\mathbf{u}_i}{dt} = \frac{\partial\mathbf{u}_i}{\partial t} + \mathbf{u}_i \cdot \nabla\mathbf{u}_i. \tag{2.10}$$

For the snow phase, the turbulent component of the drag force, arising from turbulent fluctuations of the volume fractions and velocities in the Gosman two-fluid model is given by,

$$\mathbf{F_t} = -K\frac{\nu_{t2}}{\sigma_\alpha}\nabla\alpha_1. \tag{2.11}$$

Here, ν^t and σ_α are respectively the turbulent kinematic viscosity of the air phase and the Schmidt number.

The current formulation of `twoPhaseEulerFoam` does not include the turbulent drag term. Instead, it uses a continuity equation of the following form,

$$\frac{\partial\alpha_i}{\partial t} + \nabla \cdot (\mathbf{u}_m\alpha_i) - \nabla \cdot (\mathbf{u}_r\alpha_i(1 - \alpha_i)) = 0 \tag{2.12}$$

Equation 2.12 provides tighter coupling between the phases since it uses the mixture and relative velocities, as well as both volume fractions [136]. It does not include a turbulent diffusion term, but the third term on the left hand side can be considered a volumetric mass flow rate source term, playing the same role as the turbulent diffusion term in equations 1.1 and 1.24.

The stress term in the phase momentum equation is the sum of the laminar viscous and Reynolds stresses, where the latter is modelled according to the Boussinesq formulation. The combined viscous and Reynolds stress term is then given by,

$$\mathbf{R}_i = -\nu_{eff_i}\left(\nabla\mathbf{u}_i + \nabla\mathbf{u}_i^T - \frac{2}{3}\mathbf{I}\nabla \cdot \mathbf{u}_i\right) + \frac{2}{3}\mathbf{I}k_i. \tag{2.13}$$

Here, the effective kinematic viscosity ν_{eff_i} is the sum of the phase kinematic viscosity ν_i and the phase turbulent kinematic viscosity,

$$\nu_{eff_i} = \nu_i + \nu_{t_i} \tag{2.14}$$

The phase turbulent kinematic viscosity can be obtained from the turbulence model used as explained in section 2.2.

In this thesis, the modified phase continuity equation 2.12 that is available by default in `twoPhaseEulerFoam` has been replaced with the classical continuity equation 2.1. Moreover, the turbulent drag term from equation 2.11 has been added to the momen-

tum equation 2.2. This is believed to be a more suitable model since it includes all the relevant physics. The discretisation and solution procedure of the present model mimic closely those of `twoPhaseEulerFoam`, as detailed by Weller [136] and Rusche [137].

2.2   The Treatment of Turbulence

The air phase turbulence is modelled using the standard $k-\epsilon$ turbulence model, consisting of transport equations for the turbulent kinetic energy k and dissipation rate ϵ [138]. In reality, particle-laden flows exhibit turbulence modulation by the particles, and Gosman *et al.* [130] present a modified $k-\epsilon$ turbulence model that accounts for the continuous fluid phase volume fraction, with source terms representing the turbulence kinetic energy and dissipation rate modulation. The Gosman model was developed for gas-solid and gas-liquid flows in stirred vessels with much higher particle phase loadings than the present application. The source terms in the Gosman model are based on the turbulent drag force and the turbulence response function presented below. This model was tested on dilute flows such as the ones concerned in this thesis, and found to perform identically to the standard $k-\epsilon$ model applied to the continuous phase alone. As such, the standard unmodified model is used for its simplicity. The standard $k-\epsilon$ transport equations for the continuous phase turbulent kinetic energy k_2 and dissipation rate ϵ_2 as implemented are,

$$\frac{\partial k_2}{\partial t} + \nabla \cdot (\mathbf{u}_2 k_2) - \nabla \cdot \left(\frac{\nu_{t2}}{\sigma_k} \nabla k_2 \right) = P - \epsilon_2, \tag{2.15}$$

$$\frac{\partial \epsilon_2}{\partial t} + \nabla \cdot (\mathbf{u}_2 \epsilon_2) - \nabla \cdot \left(\frac{\nu_{t2}}{\sigma_\epsilon} \nabla \epsilon_2 \right) = \frac{\epsilon_2}{k_2}(C_1 P - C_2 \epsilon_2). \tag{2.16}$$

Here, $\sigma_\epsilon = 1.3$ and $\sigma_k = 1.0$ are the turbulent dissipation rate and kinetic energy Schmidt numbers, $C_1 = 1.44$ and $C_2 = 1.92$ are model constants, $P = 2\nu_{t2}S_2^2$ is the turbulent kinetic energy production, and S_2 is the strain rate of the air phase. The continuous phase turbulent viscosity is calculated as $\nu_{t2} = C_\mu \frac{k_2^2}{\epsilon_2}$, where $C_\mu = 0.09$.

Particle phase turbulence is modelled using the turbulence response function C_t approach of the Gosman model. The turbulence response function is defined as,

$$C_t = \frac{u_1'}{u_2'}, \tag{2.17}$$

where u_1' and u_2' are respectively the turbulent velocity fluctuations of the dispersed snow phase and the continuous air phase. Issa and Oliveira [139] present a simple and practical definition of C_t,

$$C_t = \frac{3 + \beta}{1 + \beta + 2\frac{\rho_1}{\rho_2}}. \tag{2.18}$$

For spherical particles the parameter β is given by,

$$\beta = 2\frac{\alpha_1 K L_e^2}{\rho_2 \nu_2 Re_t}. \tag{2.19}$$

The turbulent Reynolds number Re_t is given by,

$$Re_t = \frac{u_2' L_e}{\nu_2}. \tag{2.20}$$

L_e is the characteristic length for energy-containing eddies which can be calculated using the following expression,

$$L_e = C_\mu \frac{k_2^{1.5}}{\epsilon_2}. \tag{2.21}$$

Finally, the continuous fluid phase turbulent velocity fluctuation can be calculated using the following expression,

$$u_2' = \sqrt{\frac{2k_2}{3}}. \tag{2.22}$$

Using C_t one can calculate the turbulent viscosity and kinetic energy of the dispersed phase as follows,

$$\nu_{t1} = C_t^2 \nu_{t2}, \tag{2.23}$$

$$k_1 = C_t^2 k_2. \tag{2.24}$$

2.3   The Particle Phase Viscosity Model

In this section the derivation of the particle phase viscosity model for high rates of strain is presented in detail. The analysis is carried out on the control volume shown in Figure 2.1. The drifting particle phase viscosity model is derived by matching the total momentum of a number of ideal spherical drifting particles within the control volume, with the momentum of the same control volume containing an equal amount of the equivalent viscous fluid. Drifting particles move in transient hops and bounce over the bed, but since drifting snow and sand can be observed in self-sustained steady-state mode in natural and controlled environments, the motion of the spherical particles can be considered steady-state *in the*

average Eulerian sense. This approximation is only used for the purpose of deriving a particle phase viscosity model. A scale analysis showed that the rolling friction force is negligible compared to the drag force, so friction was omitted from the analysis. Neglecting friction forces is further justified by the fact that their effects and that of bed asperities are already implicitly included in the experimentally measured surface threshold shear stress.
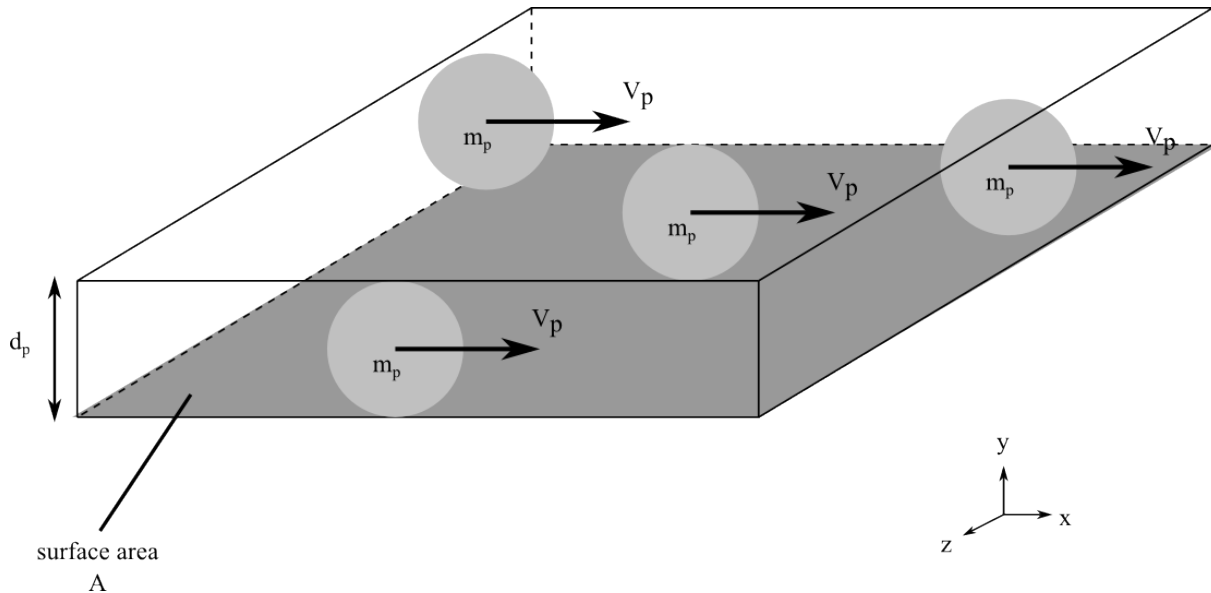
Figure 2.1: Control volume on the bed with ideal spherical particles.

The derivation of the drifting particle phase dynamic viscosity starts with the momentum equations of the continuous and dispersed phases respectively, for fully-developed steady-state flow in a control volume containing a number of rolling particles on the bed, and having the same height as a particle. At typical drifting particle height $d_p \leqslant 1\,\text{mm}$, surface threshold friction velocity $u_* \leqslant 0.5$ [140], and air temperature below freezing, the non-dimensional wall distance to the bed is $y_+ \leqslant 50$. Under such conditions, the airflow profile is weakly non-linear, and the divergence of the stress tensor negligible compared to the pressure gradient. Therefore, we can write the dispersed particle phase and continuous air phase momentum equations for steady-state fully-developed flow as,

$$-\alpha_1 \frac{\partial p}{\partial x} + F_d + \alpha_1 \mu_1 \frac{d^2 u_1}{dy^2} = 0, \tag{2.25}$$

$$-\alpha_2 \frac{\partial p}{\partial x} - F_d = 0. \tag{2.26}$$

Here, $\partial p/\partial x$ is the downstream pressure gradient, F_d is the drag force on a particle, and μ_1 is the particle phase dynamic viscosity. One can eliminate the drag force between the equations above and solve for the particle phase velocity on the bed using the following boundary conditions at the bed surface,

$$u_1 = 0, \tag{2.27}$$

$$\tau_t = \alpha_2 \rho_2 u_*^2. \tag{2.28}$$

The resulting particle phase velocity on the bed is,

$$u_1(y) = \frac{1}{2\alpha_1 \mu_1} \frac{\partial p}{\partial x} y^2 + \frac{\tau_t}{\alpha_1 \mu_1} y. \tag{2.29}$$

The expression for the dynamic viscosity is obtained by matching the linear momentum of the Lagrangian particle phase with that of the equivalent Eulerian particle phase. The Lagrangian linear momentum per unit volume $P_{L,v}$ and the Eulerian linear momentum per unit volume $P_{E,v}$ are given by,

$$P_{L,v} = \alpha_1 \rho_{ice} V_p, \tag{2.30}$$

$$P_{E,v} = \alpha_1 \rho_{ice} d_p \int_0^{d_p} u_1(y) dy. \tag{2.31}$$

Here, ρ_{ice} is the ice density and V_p the average particle velocity. Integrating and setting $P_{L,v} = P_{E,v}$ provides the following expression of the drifting particle phase dynamic viscosity,

$$\mu_1 = \frac{\frac{1}{6} \frac{\partial p}{\partial x} d_p + \frac{1}{2} \tau_t}{\dot{\gamma}_1}. \tag{2.32}$$

Here, $\dot{\gamma}_1$ is the particle phase rate of strain defined as,

$$\dot{\gamma}_1 = \alpha_1 \frac{V_p}{d_p} \tag{2.33}$$

Equation 2.32 can also be reformulated in terms of the drag force,

$$\mu_1 = \frac{-\frac{1}{6} \frac{F_d d_p}{\alpha_2} + \frac{1}{2} \tau_t}{\dot{\gamma}_1}. \tag{2.34}$$

In aeolian transport phenomena the drag force usually points downstream, in the direction of the decreasing downstream pressure gradient. The surface shear stress usually resists the particle motion and this competition between the threshold shear stress τ_t and the pressure gradient (or drag force) is highlighted in equations 2.32 and 2.34. The pressure gradient and the drag force tend to induce motion, therefore reducing the effective viscosity

of the particle phase. Surface shear stress tends to inhibit motion, therefore increasing the effective viscosity of the particle phase. The viscosity expressions of equations 2.32 and 2.34 correctly define viscosity as the proportionality parameter between the balance of shear stress in the numerators, and the particle rate of strain in the denominator. In the present case the particle rate of strain in equation 2.33 is defined at particle scale due to the appearance of d_p in its definition. Another interesting aspect of equations 2.32 and 2.34 is their explicit dependence on the phase volume fractions.

The viscosity expressions from equations 2.32 and 2.34 apply to the drifting layers. However, they can also be used as viscosity wall functions at the bed interface with the airflow, in the one-way coupled drifting snow and suspended sediment formulations discussed in the introduction. Here, there is no significant airflow beneath the particle bed, and accurate representation of bed packing is not required. Therefore, the drag/pressure gradient term can be eliminated from equations 2.32 and 2.34 in the bed, and the viscosity of the particle Eulerian continuum is represented by the threshold shear stress. The resulting drifting particle viscosity expression implemented and tested in the present simulations is the following,

$$
\mu_1 =
\begin{cases}
0.5 \dfrac{\tau_t}{\dot{\gamma}_1} & \text{in the particle bed,} \\
\left(-\frac{1}{6} \dfrac{F_d d_p}{\alpha_2} + \frac{1}{2}\tau_t \right)/\dot{\gamma}_1 & \text{in creep/saltation/suspension.}
\end{cases}
\tag{2.35}
$$

Chapter 3

Drifting Snow Validation

The E-E formulation provides volume fraction and velocity fields of both air and snow phases, while accounting for two-way coupling between them, without equilibrium assumptions. Turbulence fields of turbulent kinetic energy and dissipation rate are also calculated. Therefore, a comprehensive validation should be done against detailed, experimental measurements that consider all such aspects. The experiment needs to be sufficiently controlled to provide reliable and stable measurement data. To the knowledge of the author, the only measurement data of this nature is from a wind tunnel controlled drifting snow experiment performed by Okaze *et al.* [141]. The relevant details of the experiment are presented first, then the numerical setup of the simulations. The discussion proceeds with comparisons of the numerical simulation results to the experimental measurements for the classical formulation with turbulent drag. Monodisperse results are presented first, then polydisperse results.

3.1 The Controlled Wind Tunnel Drifting Snow Experiment

The experimental data used to validate the present viscosity model comes from a controlled wind tunnel experiment of drifting snow using actual snow particles [141]. The wind tunnel is of the return flow closed-circuit kind, and has a 1 by 1 m working section that is 14 m long. The experiment was carried out at the Cryospheric Environment Simulator (CES) of the Shinjo Branch of the Snow and Ice Research Center (SIRC) by the snow research group of the Tohoku university in Japan. This experiment was selected because it provides detailed measurements of the snow fluxes, airflow velocity and turbulent kinetic energy profiles at several measurement stations in the working section of the tunnel, and across the entire saltation layer and lower part of the suspension layer. Moreover, this experiment allows comparison to both developing and nearly developed regimes, since the flow was found to transition from a developing state at the first two

39

measurement stations to a nearly developed state at the last two measurement stations.

The experimental layout of the wind tunnel working section is shown in Figure 3.1 with all measurement stations. The wind tunnel is installed in a cold chamber where the temperature was set to $-10\,°C$ for the experiment. The first measurement station is at X = 0 m , and is preceded by a 1 m fetch of hardened snow that cannot drift. This fetch is used to induce a non-equilibrium boundary layer before the 14 m working section, which includes a groove that is 0.8 m wide and 2 cm deep along its entire length. The groove is filled with loose snow that can drift. The other five measurement stations are located at X = 1, 3, 6, 9 and 11.5 m.

The airflow velocity profiles were measured at all six stations, and the snow flux profiles only at the last five (X = 1 m to 11.5 m). A hot-wire anemometer was used to measure the instantaneous airflow velocity at the first measurement station (X = 0 m), presumably because there would be no risk of impact from drifting snow particles. At X = 0 m, measurements were taken at twelve vertical levels (Z = 5, 7.5, 10, 15, 20, 25, 30, 40, 50, 60, 75 and 100 cm) . Unlike the first measurement station, the airflow velocity and snow flux profiles at the five downstream stations were measured at nine levels along the vertical Z-axis (Z = 1, 2, 3, 4, 5, 6, 8, 12 and 20 cm). At the downstream stations the authors used an ultrasonic anemometer with a probe span of 30 mm to measure the airflow instantaneous velocity at all points above Z = 3 cm, due to the span limitation of the probe. The three points closest to the snowbed (Z = 1, 2 and 3 cm) were sampled with a pitot tube having an Outer Diameter (OD) of 1.5 mm and an Inner Diameter (ID) of 0.5 mm, according to the approach adopted by several authors for aeolian sand transport [142–145], and saltating snow[146]. The snow flux was measured with a Snow Particle Counter (SPC), similarly to the approach of Sato *et al.* [24]. The turbulent kinetic energy profiles were measured at the first and last measurement stations (X = 0 and 11.5 m). The model names and sampling rates of the instrumentation used for the measurements are provided in Table 3.1.

During each experiment run the measurements were taken at each measurement station for a period of 7 s once the saltation layer had reached steady-state. The 7 s period was confirmed to be long enough to provide stable averages during preliminary runs. Once measurements were completed at one station, the measurement instruments were moved to the next station for another measurement period of 7 s, and so on. The total measurement period for all stations was 30 s, during which erosion of the snowbed height was negligible. The measurement periods were repeated several times for all stations in order to verify the validity of the data. The snow was spread and smoothed again before each measurement run in order to ensure the same conditions of developing saltation layer. The time-averaged values were calculated for the middle 5 s in the 7 s measurement period. The total number of times measurements were repeated at each station for the airflow velocity setting concerned here are provided in Table 3.2. It should be mentioned that

the experiment authors did not report snow flux and airflow velocity profiles for X = 1 m, so numerical results at this station are not reported in our analyses below.

Table 3.1: Instruments used for the experimental measurements, with sampling rates and frequency response limits.

Parameter	Instrument type	Brand	Model	Probe	Sampling rate (Hz)	Frequency response limit (Hz)
Airflow velocity (m/s)	3D ultrasonic anemometer	Kaijo Sonic Corporation	DA-650	TR-92T	100.0	20.0
	Pitot tube	Okano Works, Ltd.	LK-00	-	2.0	2.0
	Hot wire anemometer	Kanomax	IHW-100	0252R-T	10,000	10,000
Snow flux	Snow particle counter	Niigata Electric Co., Ltd.	SPC-S7	-	1.0	1.0

Table 3.2: Number of times the measurements were repeated at each measurement station per instrument type.

Instrument	Date	X = 1 m	X = 3 m	X = 6 m	X = 9 m	X = 11.5 m
Pitot tube	August 2009	5	7	8	-	2
	September 2010	-	-	4	4	4
Ultrasonic anemometer	August 2009	5	7	6	-	2
	September 2010	-	-	3	3	3

The turbulence kinetic energy and airflow velocity profiles measurements at X = 0 m are shown in Figures 3.2 and 3.3. They are non-dimensionalized with the reference airflow velocity U_r at a reference height $Z_r = 20$ cm. The airflow velocity and snow flux profiles were also measured at the downstream stations located at X = 3, 6, 9 and 11.5 m. Turbulent kinetic energy profiles were also measured at the last downstream station at X = 11.5 m. The experiment authors report developing flow conditions at X = 3 and 6 m, and nearly-developed flow conditions at X = 9 and 11.5 m, based on the snow flux profiles.

Samples of the snow particles used in the experiment are shown in Figure 3.4 with a 1 mm scale bar in green. The experimental snow particles are quite irregular, exceeding
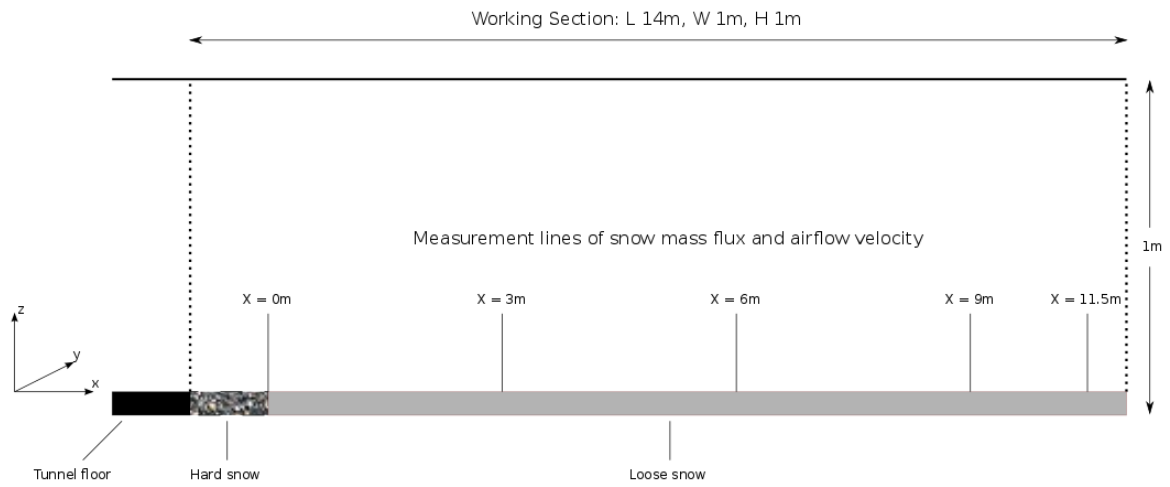
Figure 3.1: Wind tunnel experimental layout.
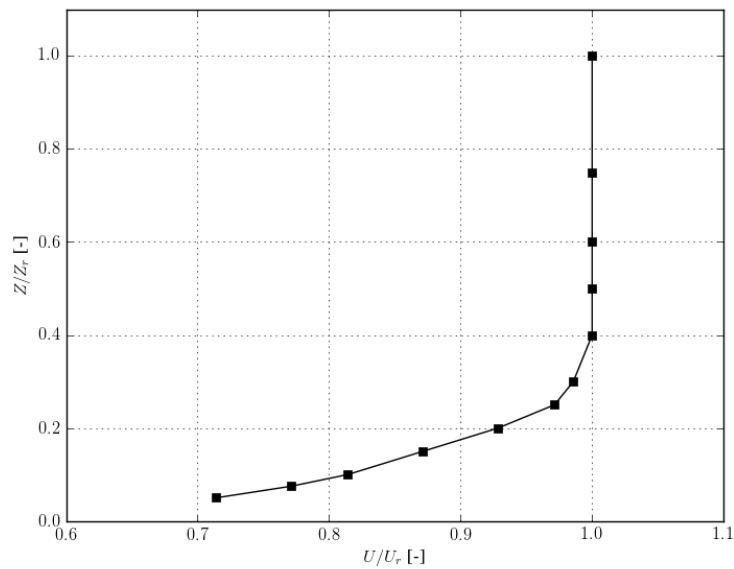
Figure 3.2: Airflow velocity non-dimensionalized by the reference velocity at 20 cm height, measured at X = 0 m and used as an inlet boundary condition for the simulations.
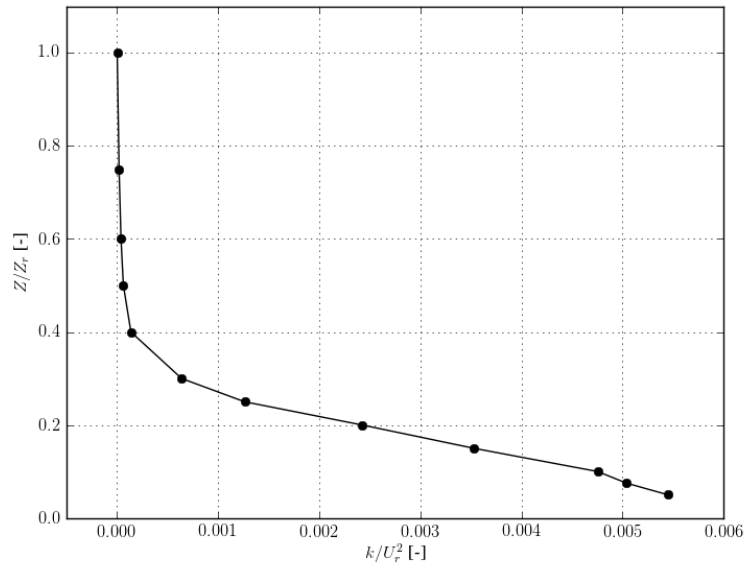
Figure 3.3: Turbulent kinetic energy non-dimensionalized by the reference velocity at 20 cm height, measured at X = 0 m and used as an inlet boundary condition for the simulations.

1 mm in length quite often, but rarely smaller than 0.10 mm in either length or width. The present formulation relies on spherical particle drag correlations since no practical correlations for irregular particles are available in the literature. However, as the present irregular particles drift they rotate around three axes within a somewhat spheroidal volume of air. Therefore, their drag function could be similar to that of a spherical particle with differences that cannot be predicted at the moment. It remains that the spherical particle drag correlations are the only practical recourse at the moment.

3.2 The Drifting Snow Simulations Setup

The 2D computational domain used for the simulations is shown in the top part of Figure 3.5. A close-up of the mesh at the inlet of the computational domain from X = 0 m to about X = 1 m is also shown, with another close-up showing the loose snow layer in the gutter in white. The volume fraction of the snowbed is set to 0.394 in order to match the experimentally measured snowbed density of $361 \, \text{kg} \cdot \text{m}^{-3}$, in relation to the maximum ice density of $917 \, \text{kg} \cdot \text{m}^{-3}$. The measured profiles at X = 0 m from Figure 3.1 are used as inlet boundary conditions for the simulations. The multiphase flow equations are solved using the PISO algorithm [147] and second-order accurate discretization schemes, considered to be the best trade-off between accuracy and computational cost with the FVM. An overview of the boundary conditions is provided in Table 3.3. The computational mesh is fully structured, composed of hexahedral cells, with a transverse cell size of 2 mm in the gutter and at the top of the tunnel. The longitudinal cell size in the flow direction
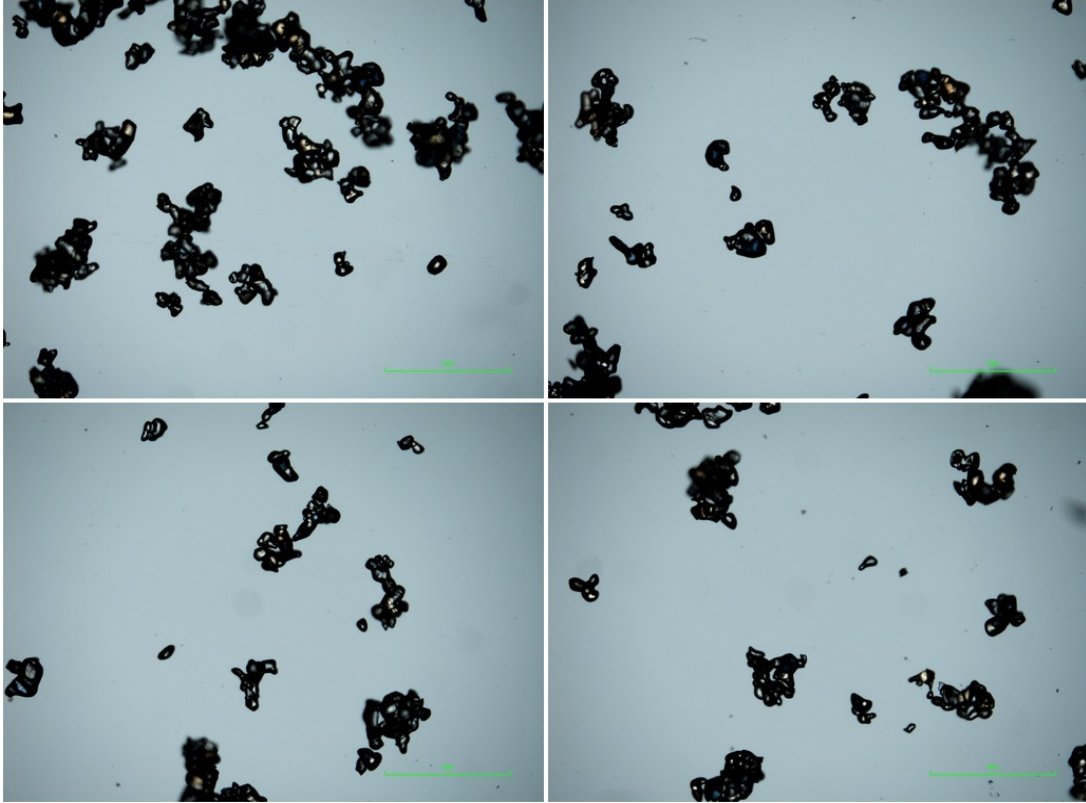
Figure 3.4: Samples of the snow particles used in the experiment with a 1 mm scale bar in green (courtesy of Professor Tsubasa Okaze).

along the X-axis is about 3.125 cm. The results obtained with the present mesh varied by less than 15% from results obtained with a mesh twice as coarse in both transverse and longitudinal directions. Therefore, the present results can be reasonably considered mesh-independent. All numerical results reported in this section were obtained over successive periods of 7 s, with time averages carried out over the middle 5 s, as was done in the experiments.

Table 3.3: Boundary conditions used for the E-E drifting snow simulations (L in the ϵ inlet boundary condition is the mixing length, taken as 10% of the channel height).

	inlet	outlet	Boundaries top	bottom	sides
α_1	Dirichlet (fixedValue)	Dirichlet-Neumann (inletOutlet)	Neumann (zeroGradient)	Neumann (zeroGradient)	empty
p	Neumann (zeroGradient)	Dirichlet (zero pressure)	Neumann (fixedFluxPressure)	Neumann (fixedFluxPressure)	empty
$U_{1,2}$	Dirichlet (exp. prof.)	Dirichlet-Neumann (inletOutlet)	wall function	wall function	empty
k	Dirichlet (exp. prof.)	Dirichlet-Neumann (inletOutlet)	wall function	wall function	empty
ϵ	Dirichlet $\left(C_\mu^{0.75} k^{1.5}/L\right)$	Dirichlet-Neumann (inletOutlet)	wall function	wall function	empty

The threshold friction velocity for each particle size class was calculated using the

following relationship [1],

$$u_{*t}(d_p) = A\left(\frac{\rho_{ice} - \rho_2}{\rho_2} g d_p\right)^{0.5}. \tag{3.1}$$

Here, $A = 0.17$ for old snow particles with highly irregular shapes [148], and $\rho_{ice} = 917\,\mathrm{kg \cdot m^{-3}}$. The threshold shear stress is calculated as,

$$\tau_{*t} = \rho_2 u_{*t}^2. \tag{3.2}$$

The resulting values of threshold friction velocity and shear stress for all particle sizes used in the present simulations are shown in Table 3.4.
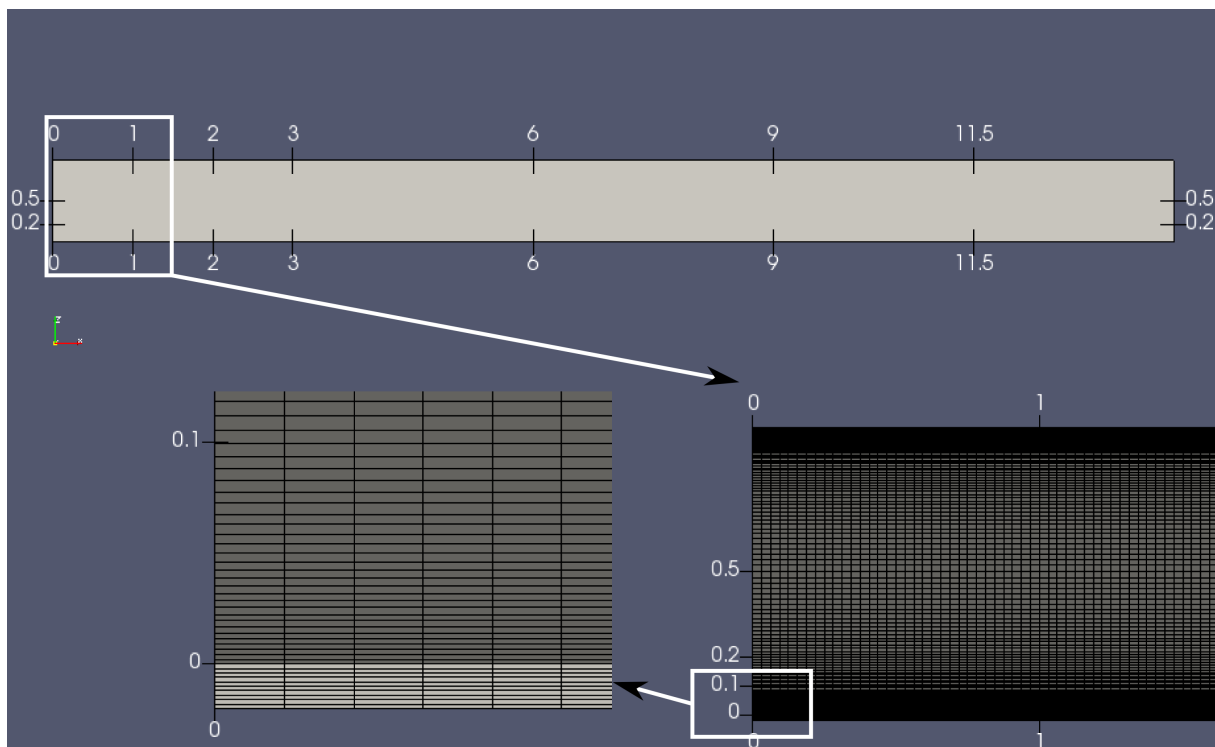
Figure 3.5: Drifting snow simulation domain (upper right), with close-ups of the computational mesh at the inlet region (lower right) showing the white snow layer in the gutter (lower left).

Table 3.4: Threshold friction velocities and shear stresses for simulation particle sizes.

Particle size (mm)	0.1	0.3	0.5	0.7	0.9	1.1	1.3
$u_{*t}\,(\mathrm{m \cdot s^{-1}})$	0.13	0.23	0.29	0.34	0.39	0.43	0.47
$\tau_{*t}\,(\mathrm{kg \cdot m^{-1} \cdot s^{-2}})$	0.022	0.069	0.109	0.150	0.198	0.240	0.287

3.3   Results and Discussion

3.3.1   The Monodisperse Simulations

The drifting experiment analysed here is a transient one given the limited supply of drifting snow in the wind tunnel gutter. Judging from the snow samples shown previously, particles of different sizes were present, so monodisperse simulations of single particle size were carried out for each of the following seven particle diameters that seem to cover the entire size range: 0.1, 0.3, 0.5, 0.7, 0.9, 1.1 and 1.3 mm. The snow flux results of 0.2 mm, 0.3 mm and 0.7 mm particles at X = 3 m are shown in Figures 3.6, 3.7 and 3.8, for $\sigma_\alpha = 1.0$. The snow flux profiles of the 0.2 mm particles are much larger than the experimental measurements profiles and do not match them in either value or shape. There is a small qualitative improvement in the 0.3 mm particles snow flux profiles but the agreement is still quite poor with no snow flux whatsoever in the suspension layer above 6 cm height. The 0.7 mm particles are the largest of the three sizes analyzed here and they show the poorest agreement with experimental measurements, with no snow flux whatsoever above 1 cm height at the lowest levels of the saltation layer. The larger the particle the bigger the cross section it presents to the airflow, hence the drag force acting against it. Larger diameter result also in much more weight, which combined with the increase in drag force translates into much less snow flux than the smaller particles. The results of the other five particles sizes are not shown here, but they follow the same trend seen with the three sizes analyzed here, and poor agreement with the experimental measurements as well. This prompted an investigation of polydisperse effects for particle size distributions, presented in the next section.

3.3.2   The Polydisperse Simulations

The present formulation can only simulate one particle size at a time. Therefore, the only way to reproduce the results of polydisperse particle size distributions is to combine the results of several monodisperse simulations. Here, it is done linearly using the statistical weight of each size class in the distribution. This approach is considered acceptable since the particle flow in the saltation and suspension layers is dilute, with no particle collisions or interactions occurring. Particle size distributions were not reported in the experimental paper but mechanical breakage phenomena such as drifting snow usually obey a two-parameter Γ distribution, whether aggregate on the ground [149] or drifting above it [150]. The two-parameter Γ Probability Distribution Function (PDF) $f(x)$ and the Γ function are given by,

$$f(x) = \frac{b^a}{\Gamma(a)} x^{a-1} e^{-bx}, \tag{3.3}$$
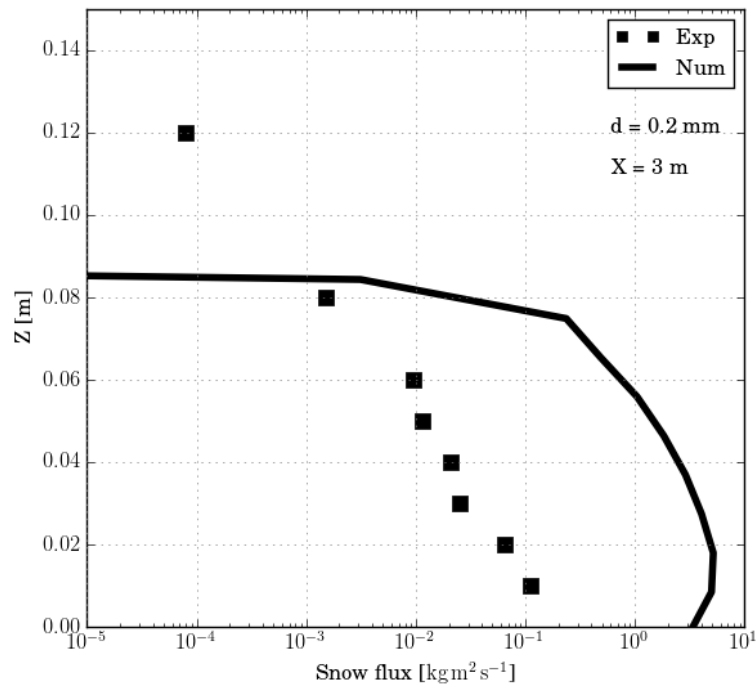
Figure 3.6: Snow flux profiles for $d_p = 0.2$ mm at X = 3 m, with turbulent drag and the classical continuity equation 2.1.
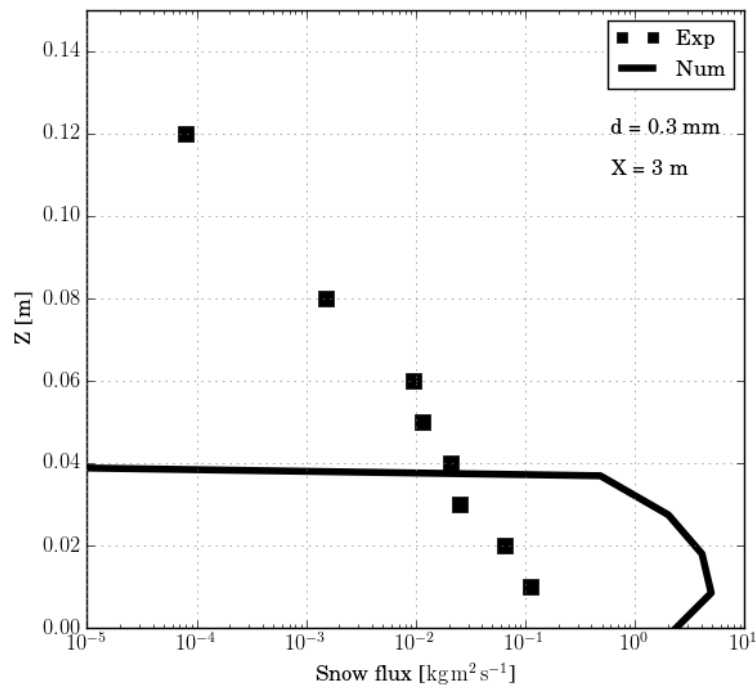
Figure 3.7: Snow flux profiles for $d_p = 0.3$ mm at X = 3 m, with turbulent drag and the classical continuity equation 2.1.
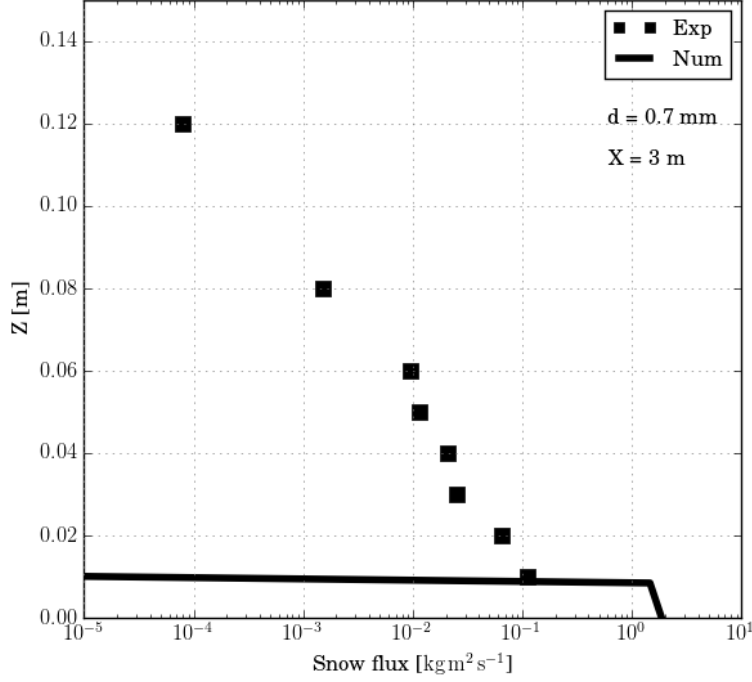
Figure 3.8: Snow flux profiles for $d_p = 0.7$ mm at X = 3 m, with turbulent drag and the classical continuity equation 2.1.

$$\Gamma(a) = \int\limits_0^\infty x^{a-1}e^{-x}dx, \qquad a \in (0,\infty). \tag{3.4}$$

Here, a and b are respectively the distribution shape and scale parameters, which define the distribution average size as $d_{avg} = a/b$. The statistical weight $w_i(d_i)$ is calculated as follows,

$$w_i(d_i) = \int\limits_{\frac{d_i+d_{i-1}}{2}}^{\frac{d_{i+1}+d_i}{2}} f(x)dx. \tag{3.5}$$

Here, d_{i-1} and d_{i+1} are the lower and upper particle size classes. Examples of two-parameter Γ PDFs are shown in Figure 3.9. The percentage contributions of the different particle classes to several distributions with average particle size from 0.3 mm to 0.9 mm are shown in Table 3.5. Contributions smaller than 0.1% are neglected.

Verifications revealed that a two-parameter Γ distribution with an average diameter of 0.6 mm matches the experimental data best. Since particle turbulence effects are not included in the present version of the $k - \epsilon$ model, the turbulent Schmidt number is taken as $\sigma_\alpha = 1.0$. Smaller average diameter distributions produced excessive snow flux due to the excess contributions of the smaller particle size classes that populate
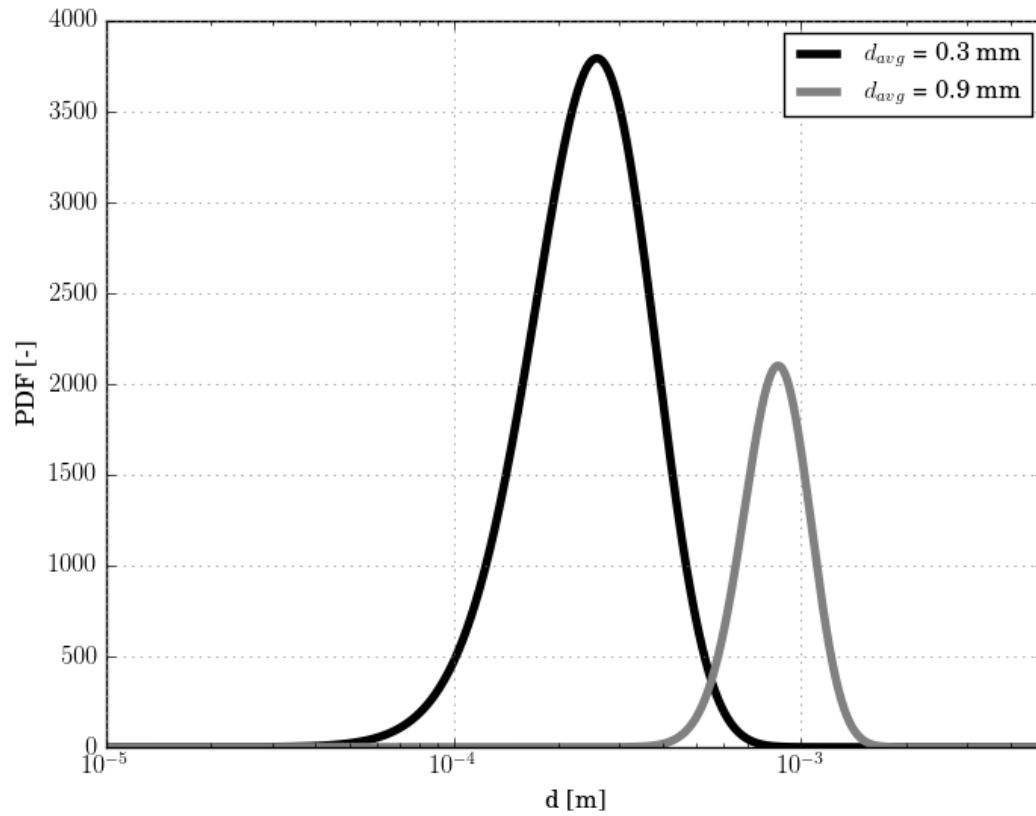
Figure 3.9: 2-parameter Γ distribution functions for $d_{avg} = 0.3$ mm and 0.9 mm.

Table 3.5: Percentage contributions to average size distributions (leftmost column) of different particle size classes.

	Particle size classes						
d_{avg}	0.1 mm	0.3 mm	0.5 mm	0.7 mm	0.9 mm	1.1 mm	1.3 mm
0.3 mm	18.6%	63.7%	16.2%	1.3%	0.5%	0.0%	0.0%
0.6 mm	0.3%	8.8%	44.6%	35.5%	9.5%	1.3%	0.1%
0.9 mm	0.0%	0.0%	4.5%	27.6%	39.4%	21.4%	6.6%

the saltation and suspension layers, as seen in the previous section. Correspondingly, larger average diameter distributions produced too little snow flux. The distribution snow flux simulation results for an average particle size of 0.6 mm at the four measurement stations from X = 3 m and downstream are shown in Figures 3.10 to 3.13, along with the experimental measurements. The agreement between simulation and experiment snow fluxes is reasonably good at all measurement stations, considering the details of the size distribution are unknown, and a spherical particle drag correlation is used for highly deformed particles. In particular, the agreement is quite good in the saltation layer, below 5 cm, where the two-way coupling between both phases is most significant. On the other hand, the simulations show no snow flux at all in the highest part of the suspension layer, above 8 cm. The experiment snow fluxes in that region are lowest, with values less than $10^{-5}\,\mathrm{kg \cdot m^{-2} \cdot s^{-1}}$, at least an order of magnitude less than the rest of the drifting layers. It is also quite possible the Γ distribution with an average diameter of 0.6 mm is not a good representation for the size distribution in the suspension layer. The two-way coupled formulation might be inaccurate in such extreme one-way coupled regimes, and further investigation is necessary. However, it is noteworthy that the new two-way coupled approach performs well in both developing and nearly developed parts of the flow.

Figure 3.10: Polydisperse Γ distribution snow flux profiles for $d_{avg} = 0.6$ mm at X = 3 m, with turbulent drag and the classical continuity equation 2.1.

The simulation airflow velocity profiles corresponding to the 0.6 mm average diameter snow fluxes are shown in Figure 3.14 to 3.17. Here, the agreement with experiment is very good at all measurement stations, and all levels of the saltation and suspension layers. In

Figure 3.11: Polydisperse Γ distribution snow flux profiles for $d_{avg} = 0.6$ mm at X = 6 m, with turbulent drag and the classical continuity equation 2.1.
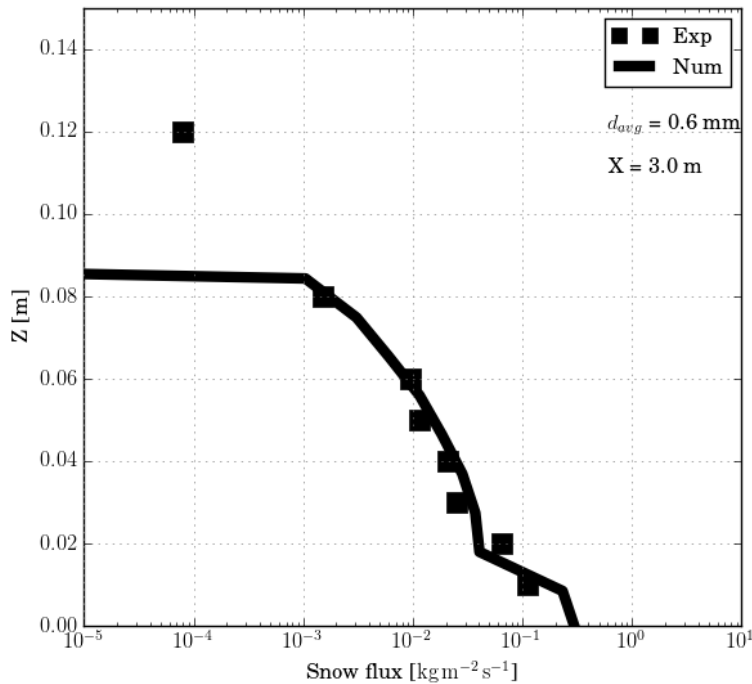

Figure 3.12: Polydisperse Γ distribution snow flux profiles for $d_{avg} = 0.6$ mm at X = 9 m, with turbulent drag and the classical continuity equation 2.1.
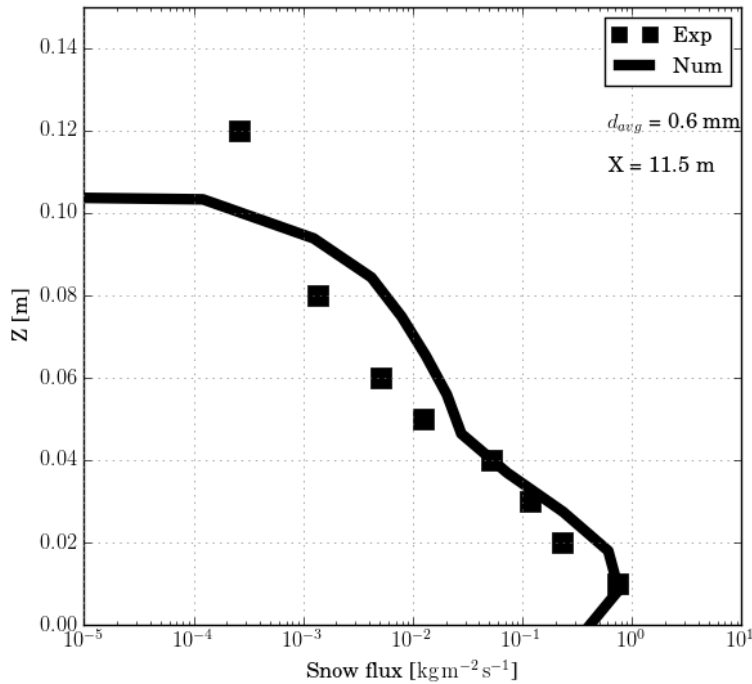
Figure 3.13: Polydisperse Γ distribution snow flux profiles for $d_{avg} = 0.6$ mm at X = 11.5 m, with turbulent drag and the classical continuity equation 2.1.

particular, the agreement between simulation and experiment improves above 8 cm, but this is effectively a single-phase flow result since the simulation distribution results report no snow flux in this region. Nonetheless, it is another indication that a hybrid approach with two-way coupling in the saltation layer, and one-way coupling *in the suspension layer* without a drag term in the airflow momentum equation could be better suited.

The turbulent kinetic energy simulation profile for the 0.6 mm average diameter distribution is compared to the experimental measurements at X = 11.5 m in Figure 3.18. Two sets of experimental measurements are shown, one for the gutter filled with hard snow that does not drift and another for loose snow that does drift. The experiment authors found that drifting snow approximately doubled the turbulent kinetic energy of the airflow, which is normally attributed to two mechanisms. The first is turbulence generation at the shear layer that forms above the snowbed as the airflow accelerates in the transition from two-way coupling in the saltation layer, to one-way coupling in the suspension layer without particle drag. This effect is akin to turbulence generation by shear at solid surfaces and is accounted for by the production term in the turbulent kinetic energy equation. The second mechanism is turbulence generation by turbulent wakes of large particles which can move faster than the airflow [151], and would form stagnation regions at their leading edges. Such stagnation regions would also form at the trailing edges of particles moving slower than the airflow.

The results of the 0.6 mm average diameter distribution simulation exceed by roughly
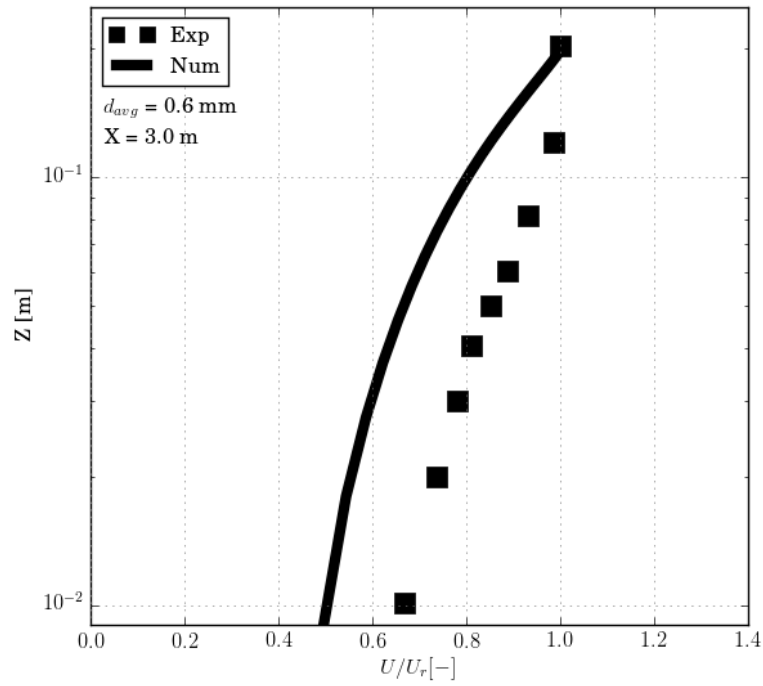
Figure 3.14: Polydisperse Γ distribution airflow velocity profile for $d_{avg} = 0.6$ mm at X = 3 m, with turbulent drag and the classical continuity equation 2.1.
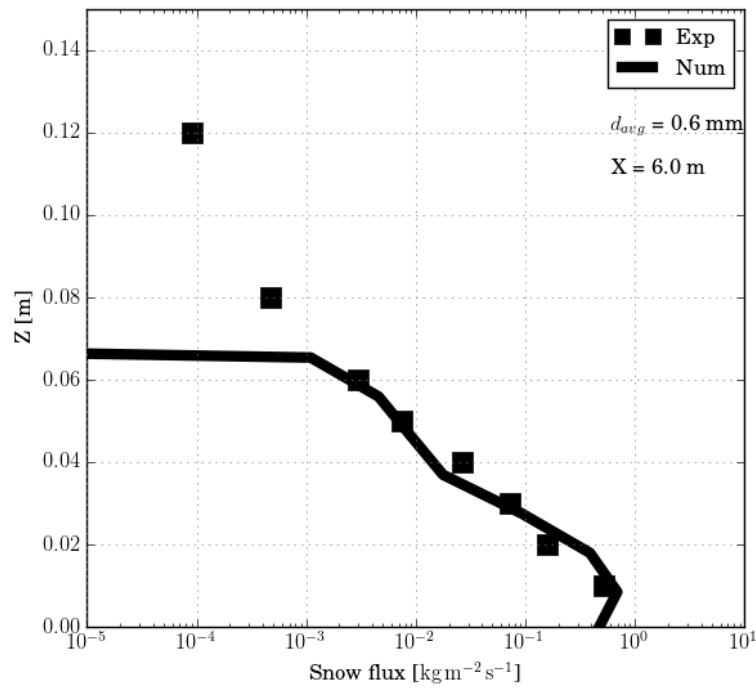

Figure 3.15: Polydisperse Γ distribution airflow velocity profile for $d_{avg} = 0.6$ mm at X = 6 m, with turbulent drag and the classical continuity equation 2.1.
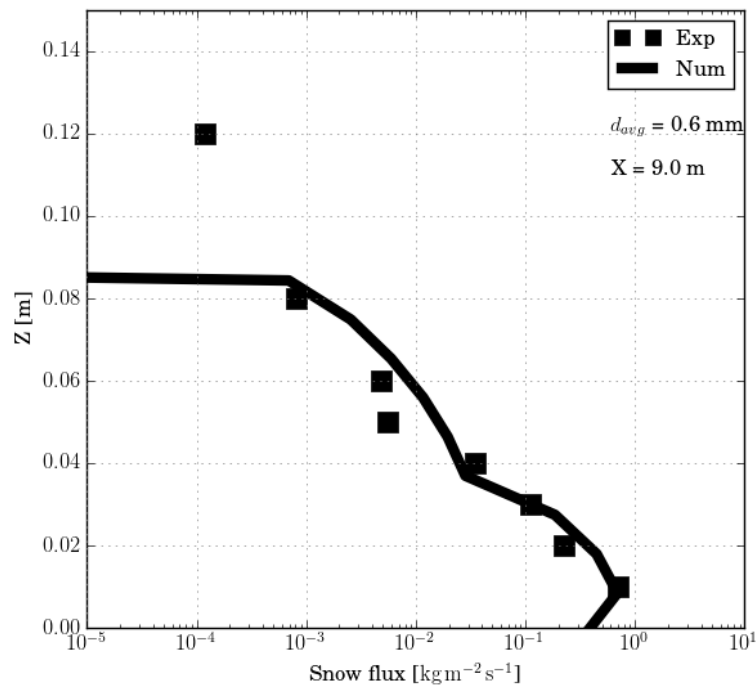
Figure 3.16: Polydisperse Γ distribution airflow velocity profile for $\boldsymbol{d_{avg}} = 0.6$ mm at X = 9 m, with turbulent drag and the classical continuity equation 2.1.

Figure 3.17: Polydisperse Γ distribution airflow velocity profile for $\boldsymbol{d_{avg}} = 0.6$ mm at X = 11.5 m, with turbulent drag and the classical continuity equation 2.1.
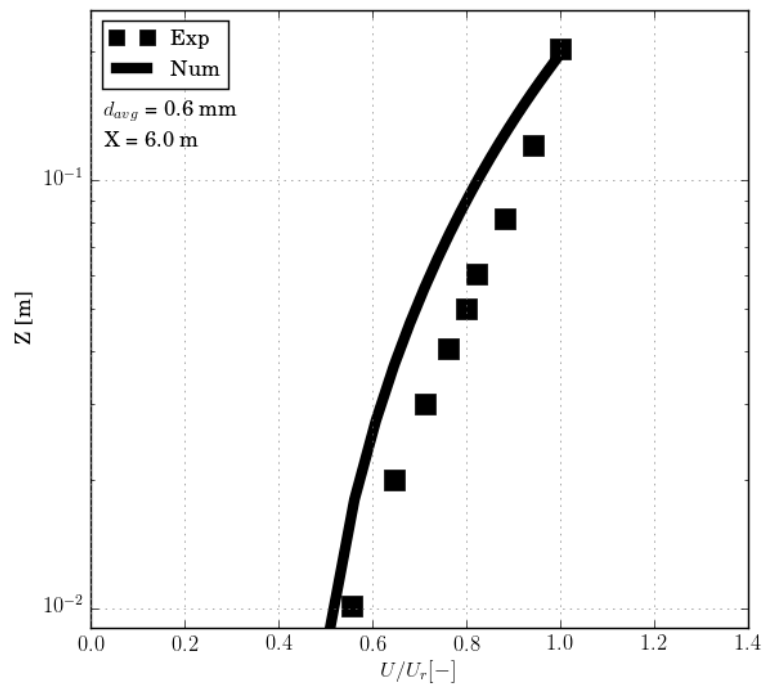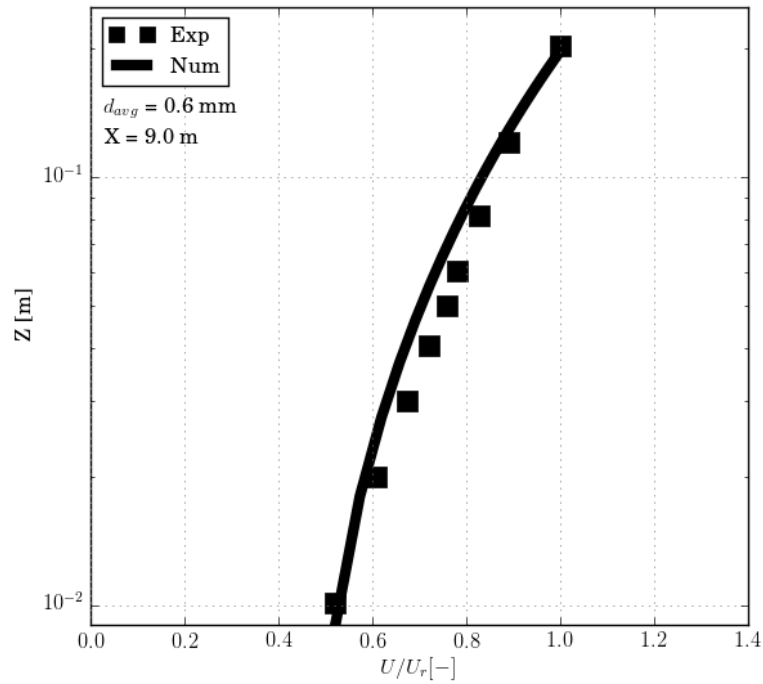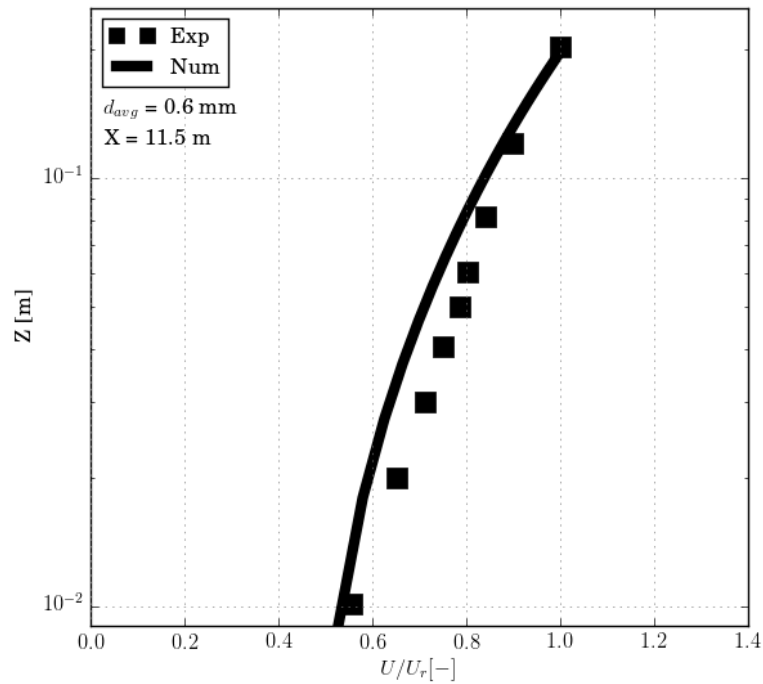
three times the loose snow experimental measurements. This is a common occurrence with the standard $k - \epsilon$ model, which is well-known to overestimate k and turbulent viscosity in regions of high strain [152], [153], and can propagate that effect to the rest of the computational domain [34]. The overestimation is due to excessive turbulence time scale, with too little production of ϵ, in turn leading to excessive production of k. Excessive turbulent kinetic energy production is also reported by Rusche [137] for two-phase flow monodisperse simulations using a similar continuous phase turbulence model. Another modification of the present standard $k - \epsilon$ model based on mixture flow properties with particle drag effects modelled by source terms for the k and ϵ conservation equations by Behzadi et $al.$ [154] reports simulation k levels that are roughly double the experimental measurements. Of particular interest to the present validation is a modified single-phase $k - \epsilon$ model by Okaze et $al.$ [155], the authors of the drifting snow experiment, that also uses source terms in the turbulence conservation equations to account for the drag effect of particles. Their approach is based on a vehicle canopy model of the subgrid effect of moving cars on wind and turbulence [156]. The extra terms are based on the generalized aerodynamic drag force in the air phase momentum equation, multiplied with proportionality constants. They impose the snow fluxes obtained from spatial interpolations of the present experimental measurements, instead of solving the snow density conservation equation, and optimize the constants in the extra terms to match the airflow velocity profiles very closely. The authors in [155] do not compare their turbulent kinetic energy profiles directly to the experimental profiles, but visual comparaison of their numerical turbulent kinetic energy profiles in Figure 8 of their paper reveals their particle-laden simulation results are about double the particle-laden measurements of Figure 10.a of their experimental paper [141]. Another important source of error is the fact that the authors of the drifting snow experiment could not measure turbulence energy in the high frequency range above 20 Hz due to instrumental limitations. Particle contribution could be important at such scales.

In short, all reviewed implementations overestimate turbulent kinetic energy in the dilute regime, which highlights the time scale shortcomings of the $k - \epsilon$ model, and the experimental measurements most certainly underestimate the actual turbulent kinetic energy levels. Therefore, the poor match in turbulent kinetic energy cannot be considered a definitive result.

Finally, the simulation snow transport is compared to the experimental values in Figure 3.19, for all measurement stations. Experimentally, the snow transport was calculated by integrating the snow flux measurements over height from Z = 0 m to Z = 5 cm. The same was done with the simulation data, which agrees well with the experimental values at all measurement stations. The numerical snow flux inaccuracies in the suspension layer are not a factor since the snow flux values there are negligible with respect to the saltation layer.
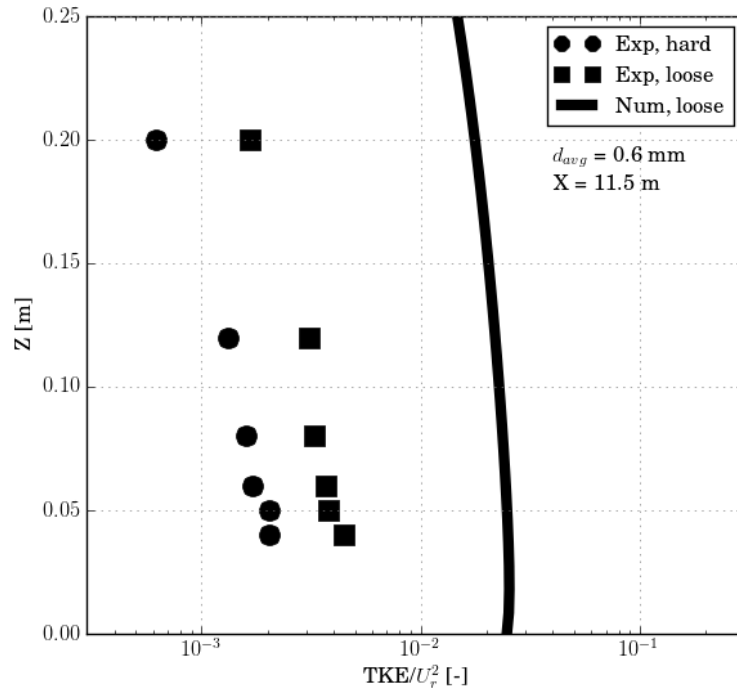
Figure 3.18: Polydisperse Γ distribution turbulent kinetic energy profiles for $d_{avg} = 0.6$ mm at $X = 11.5$ m, with turbulent drag and the classical continuity equation 2.1.
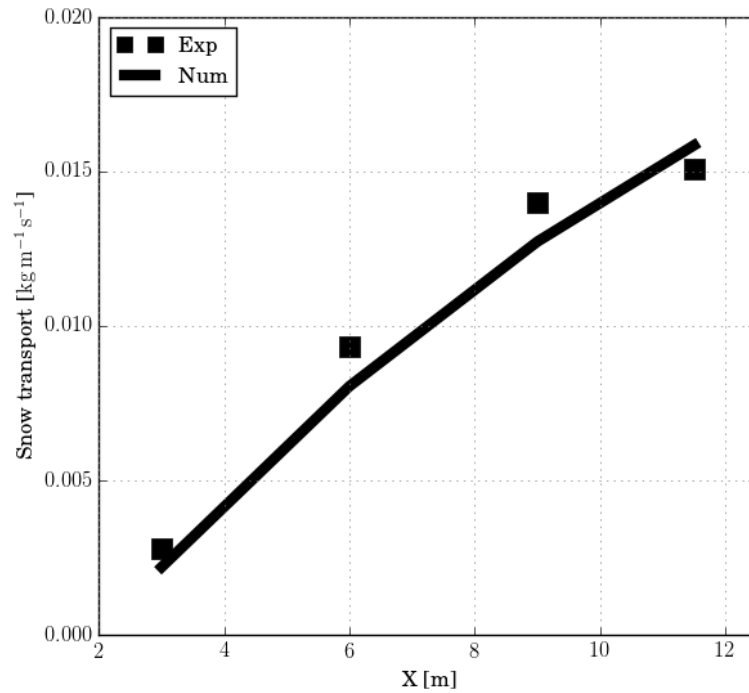

Figure 3.19: Polydisperse Γ distribution snow transport profile for $d_{avg} = 0.6$ mm at all measurement stations, with turbulent drag and the classical continuity equation 2.1.

3.4   Conclusions

The two-way coupled Eulerian-Eulerian approach to simulating drifting snow was presented along with validation results against a controlled wind tunnel drifting snow experiment. The Eulerian-Eulerian approach includes a new discrete particle phase viscosity model developed to allow calculating the viscous stress tensor in the snow phase momentum equation, without resorting to equilibrium empirical correlations used by other Eulerian methods. Simulations were performed using the classical continuity equation 2.1 and turbulent drag.

When taking the polydisperse characteristics of the experiment into consideration, the classical Eulerian-Eulerian approach with turbulent drag correctly predicted the snow flux profiles in the saltation layer and lower suspension layer, as well as the snow transport values, at all experimental measurement stations. The Eulerian-Eulerian approach is inaccurate in the upper parts of the suspension layer possibly due to particle size distribution effects, since the particle size distribution in the suspension layer can be quite different from the distribution in the saltation layer [149, 150]. Unfortunately, such an effect cannot be reliably simulated without a polydisperse numerical formulation. The new approach correctly predicted the airflow velocity profiles at all measurement stations as well. Altogether, the classical approach was found to perform well in both developing and nearly developed flows, but further validation is desirable for flows around obstacles under highly accelerating and decelerating conditions.

The turbulent kinetic energy profile measured in the experiment was overestimated with the classical two-way coupled approach, in agreement with other similar implementations. This could be due to turbulent time scale overestimation at the particle level, since the $k - \epsilon$ model overestimates turbulent kinetic energy in stagnation zones [157], and individual particles exhibit such features relative to the airflow. Another possible reason for the discrepancy is the fact that the experimental measurements of turbulent kinetic energy were obtained with an ultra-sonic anemometer that cannot measure small scale fluctuations of frequencies higher than 20 Hz [141]. Therefore, the experimental measurement is most certain to underestimate the actual values. This experimental discrepancy cannot be estimated, but the true experimental values are expected to be somewhere between the published values and the current numerical results.

The present approach can easily be extended to other multiphase flows involving transport of solid particles by fluids, such as aeolian sand erosion and riverbed sediment transport. In section 4, the present approach is validated against experimental measurements of a weakly polydisperse sand sediment suspension flume, in order to demonstrate the Eulerian-Eulerian method's applicability to multiphase flows with low phase density ratio, and assess its accuracy in the suspension layer for monodisperse particle size distributions. Comparison will also be done against the results of a one-way coupled method that uses a

classical convection-diffusion equation for sediment transport, as well as mesh movement at the bed surface in order to account for deposition and erosion.

Chapter 4

Suspended Sediment Transport Validation

The present validation is complementary with respect to the drifting snow validation in that it addresses aspects that could not be addressed in the latter. Namely, the particle transport is strictly by suspension, the particle to fluid density ratio is of the order $O(1)$, and the particle size distribution is narrow enough to be considered monodisperse. Moreover, the measurements are detailed and stable enough to be reliable for validation. The relevant details of the controlled flume experiment used for the suspended sediment validation are presented first, then the numerical setup of the simulations. The discussion proceeds with comparisons of the numerical simulation results to the experimental measurements for the classical E-E formulation with turbulent drag. The E-E results are also compared to the results of a conventional VOF formulation [106].

4.1   The Suspended Sediment Transport Experiment

The suspended sediment transport validation is carried out by simulating a suspended sediment controlled experiment [81]. The experiment consists of a straight laboratory water flume (length = 30 m, width = depth = 0.5 m) shown in Figure 4.1. A uniform flow was realised with a water depth a = 0.216 m, at a volume flow rate Q = $0.0601\,\mathrm{m^3 \cdot s^{-1}}$. Sand sediment was added to the water at a transport rate S = $70.8\,\mathrm{kg \cdot h^{-1}}$, well below the maximal transport capacity in order to avoid bedforms.

The sediment was allowed to mix along an initial fetch of 10 m over a rigid bottom, followed with a measurement section of 16 m over a perforated plate, and an outflow section of 4 m. The perforation diameter is 3 mm and the plate open area ratio is 33 %. Several compartments were included underneath the flume, with half pipes mounted 1 cm under the perforated plate in order to evacuate settling sediment and dampen turbulence under the perforations. This apparatus is shown in the compartment magnification de-

tail in Figure 4.1, and insured no sediment was reinjected into the flow from under the perforations by turbulent dispersion. Therefore, the only transported sediment was due to suspension above the perforations.

The sediment used is sand with a density of $2650 \, \text{kg} \cdot \text{m}^{-3}$, a median diameter D_{50} = $100 \, \mu\text{m}$, and a narrow size distribution with D_{84}/D_{16} = 1.46. As mentioned before for drifting snow, such particle sizes normally obey a two-parameter Γ distribution. In that case, the 84 % diameter (for which the total mass of all particles with smaller diameters would equal 84 % of the total mass present in the distribution) would be D_{84} = $119 \, \mu\text{m}$, and the 16 % diameter D_{16} = $83 \, \mu\text{m}$. A representative sampling of the applicable two-parameter Γ distribution is shown in Table 4.1 with the corresponding cumulative probabilities. The corresponding probability distribution function is plotted in Figure 4.2 with the D_{16}, D_{50}, and D_{84} diameters indicated in red, green, and blue respectively.

Table 4.1: Cumulative probabilities and particles sizes of the equivalent two-parameter Γ particle size distribution of the suspended transport experiment.

Cumulative probability (%)	Particle size (μm)
5	73
16	83
27	89
39	95
50	100
61	105
72	111
84	119
95	133

As the flow reached steady-state, measurements of sediment concentration and water velocity profiles were taken at several locations in the working section along the full height of the water flume. An unspecified sampling instrument is used to simultaneously sample 8 points along the vertical, based on the siphon method. Several measurement runs are used and the measurements are taken exclusively at the flume vertical centre plane since sediment concentration hardly varied in the lateral direction. The velocity measurements are taken using a micro-propellor. No velocity measurements are taken within the first 1.5 cm above the perforated bed due to the dimensions of the device. Artificial roughness

over the initial rigid bed helps provide a constant shape velocity profile over the perforated bed. This is shown in Figure 4.3, where it is noted that the velocity profile is only truly logarithmic from about 2 cm above the perforated plate until about 4 cm below the free surface. The lower departure from a logarithmic profile is the effect of the perforated plate, and an indication that the bed should not be modelled as a flat plate with a wall function Boundary Condition (BC), as done by other authors [106].
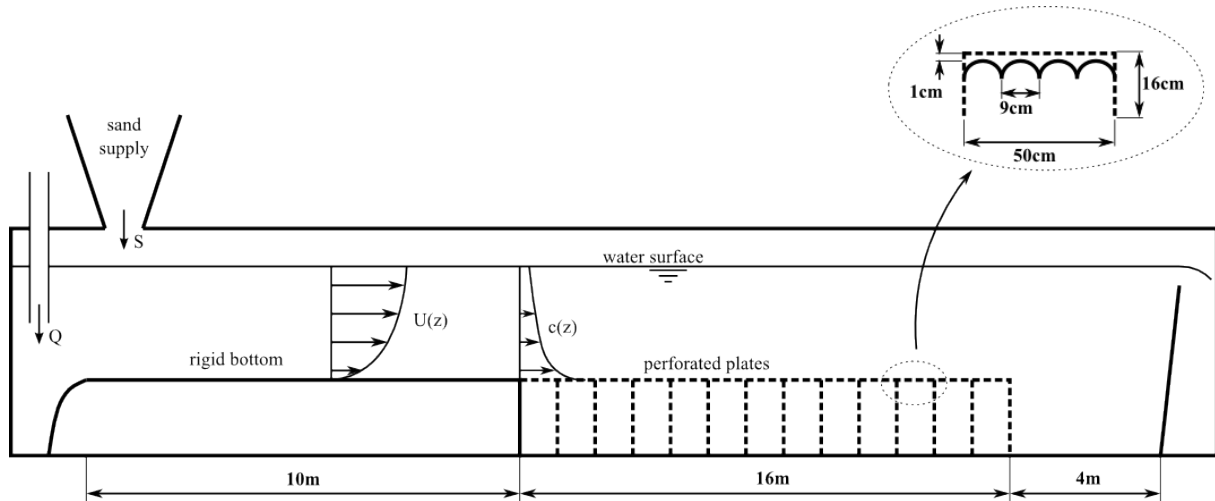
Figure 4.1: Schematic of the controlled suspended sediment experiment.

4.2   The Suspended Sediment Transport Simulations Setup

Three different simulations were computed, the first with the classical E-E approach used for the drifting snow simulations in section 3.4, the second with the VOF formulation of Sattar *et al.* without deposition and erosion at the bed, and the third with the VOF formulation again but with deposition and erosion at the bed. The experiment was carried out in a homogeneous straight rectangular flume with measurements taken in the central longitudinal plane. The computational mesh used for the E-E simulations is a three-dimensional fully structured hexahedral mesh of 1.275M cells. A side view of the mesh is shown in the upper part of Figure 4.4, with the inlet boundary and a closeup of the near-wall region at the bottom of the inlet in the lower part of the figure. The mesh used for the VOF simulations is also a three-dimensional hexahedral mesh, but consisting of 700K cells only, while accounting for the free water surface. It is shown in Figure 4.5, in a format similar to Figure 4.4. The outer dimensions of the two meshes are exactly similar in length and depth. The E-E mesh stops at the free water surface and is only 21.5 cm high since the E-E method cannot account for two continuous phases at present. The VOF mesh is 25 cm high, the same height as the flume, since the VOF method can account for the free water interface and two continuous phases, water and air.

The numerical inlet sediment concentration profile was obtained from the published
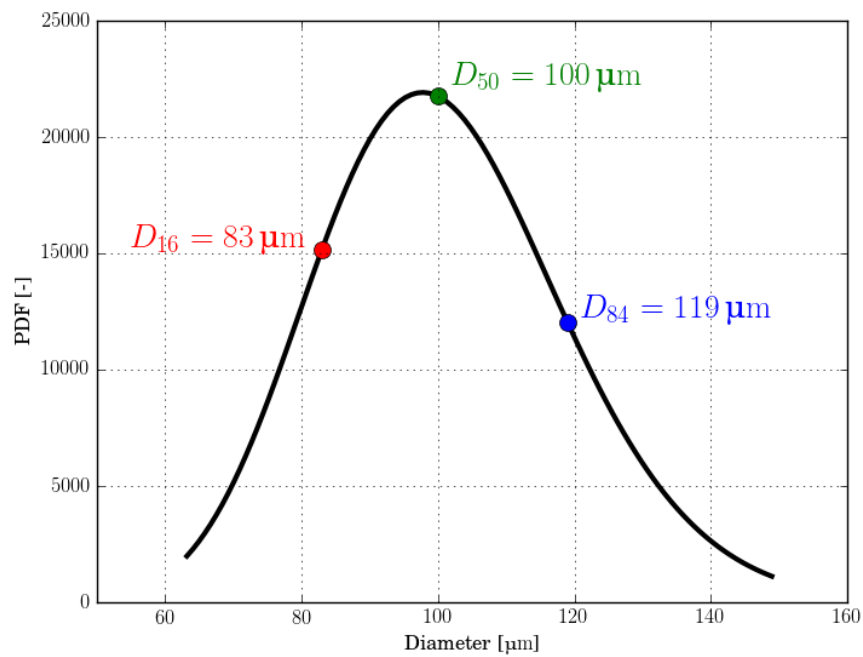
Figure 4.2: Equivalent two-parameter Γ probability distribution function of the sediment particle size of the suspended sediment experiment, with the D_{16}, D_{50}, and D_{84} diameters indicated in red, green, and blue respectively.
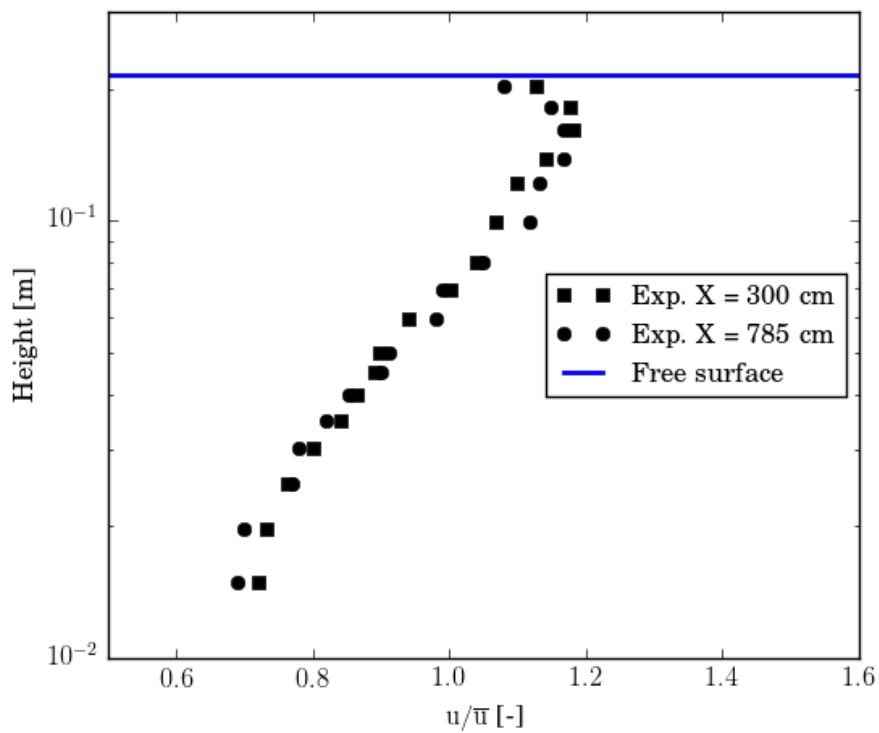
Figure 4.3: Experimental non-dimensional water velocity profiles at two stations in the measurement section of the experimental flume.

experimental profile [81], and is shown in Figure 4.6. Other inlet BCs were obtained from SS simulations of free-surface flow in a channel having the same cross section as the experimental flume. All BCs for the E-E and VOF simulations are provided in Tables 4.2 and 4.3, respectively. It must be noted that the bed perforations are not implemented, due to the very large number of perforations required. Such a geometry is very time consuming to implement, and would require a much higher number of computational cells to resolve the flow around the perforations. Moreover, there is no boundary condition available within OpenFOAM® that can represent such a surface condition. Instead, wall functions are used at the bottom bed and side walls with a roughness height of 0.0025 m at the bed, similarly to Sattar *et al.* [106]. For the sediment concentration (α_1 for the E-E simulations and c_s for the VOF simulations), a Neumann BC (`zeroGradient`) is used at the bottom. In the VOF simulations, the sediment settling velocity vS is defined as a simulation variable even though it is calculated using an empirical correlation and set constant in all computational cells. Setting a Neumann BC for vS at the bottom provides a flux boundary condition, allowing the sediment to seep through [106]. This mimics the sediment flushing effect of the perforated bottom, and the validity of this treatment is examined further below. Finally, both E-E and VOF simulations use the $k - \omega$ SST turbulence model [158, 159].
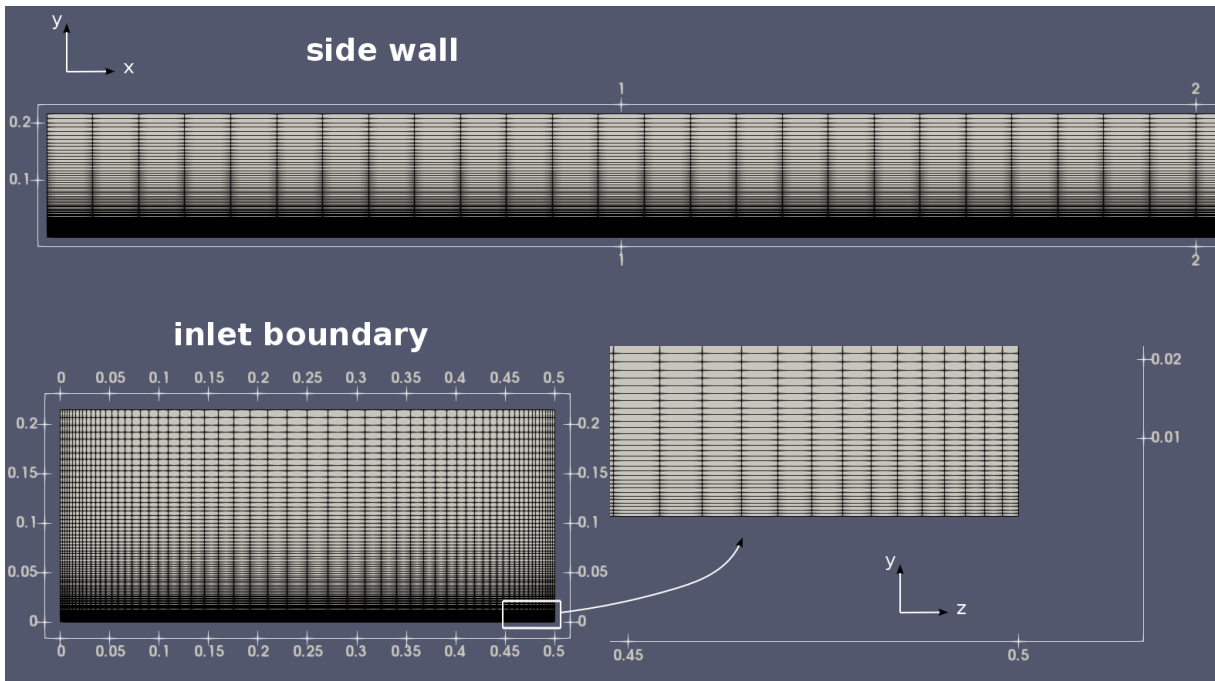
Figure 4.4: Side-view of the hexahedral mesh used for the E-E sediment simulations (upper row), with the inlet boundary and a close-up of the near-wall bottom region (lower row).

The critical friction velocity is determined according to the Shields procedure using equations 1.86 and 1.70. This results in $u_{*t} = 0.0127\,\mathrm{m \cdot s^{-1}}$, and a threshold shear stress $\tau_t = 0.1613\,\mathrm{Pa}$.
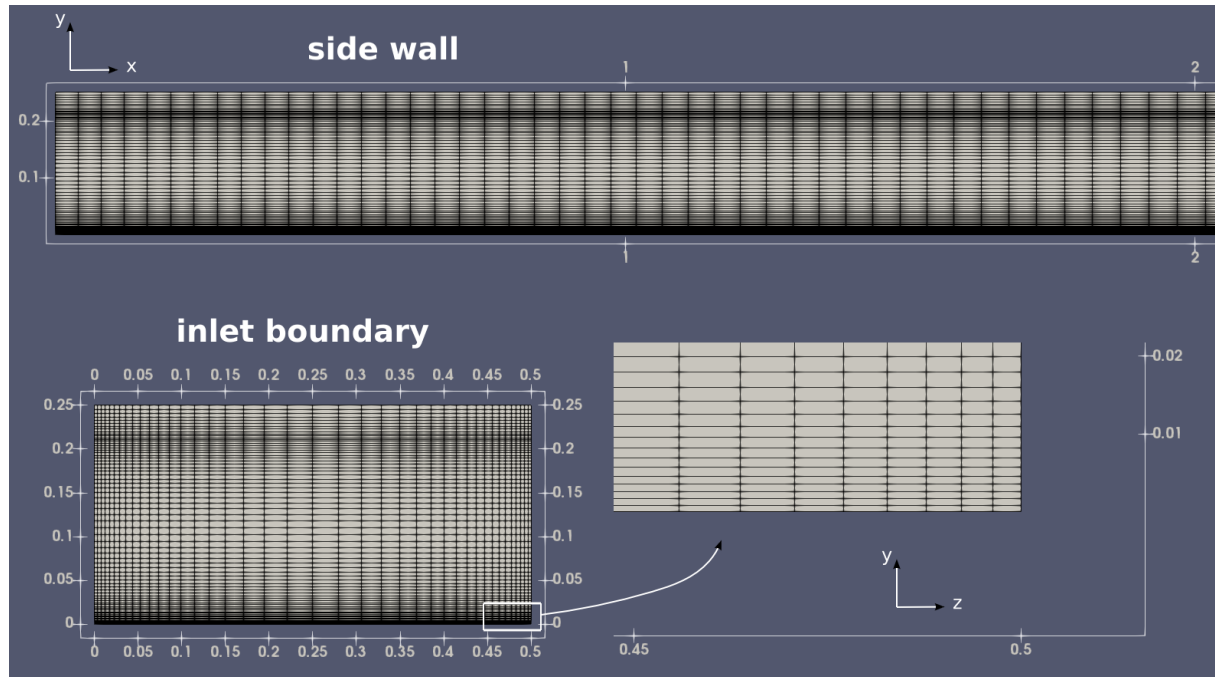
Figure 4.5: Side-view of the hexahedral mesh used for the VOF sediment simulations (upper row), with the inlet boundary and a close-up of the near-wall bottom region (lower row).

Table 4.2: Boundary conditions used for the E-E sediment transport simulations.

| | Boundaries | | | | |
	inlet	outlet	top	bottom	walls
α_1	Dirichlet (exp. prof.)	Neumann (`zeroGradient`)	Dirichlet-Neumann (`inletOutlet`)	Neumann (`zeroGradient`)	Neumann (`zeroGradient`)
p	Neumann (`zeroGradient`)	Neumann (`zeroGradient`)	Dirichlet (`totalPressure`)	Neumann (`zeroGradient`)	Neumann (`zeroGradient`)
$U_{1,2}$	Dirichlet (exp. prof.)	Dirichlet-Neumann (`inletOutlet`)	Dirichlet-Neumann (`inletOutlet`)	Dirichlet (wall function)	Dirichlet (wall function)
k	Dirichlet (SS prof.)	Dirichlet-Neumann (`inletOutlet`)	Dirichlet-Neumann (`inletOutlet`)	Dirichlet (wall function)	Dirichlet (wall function)
ω	Dirichlet (SS prof.)	Dirichlet-Neumann (`inletOutlet`)	Dirichlet-Neumann (`inletOutlet`)	Dirichlet (wall function)	Dirichlet (wall function)
ν_{t2}	Dirichlet (SS prof.)	`calculated`	`calculated`	Dirichlet (wall function)	Dirichlet (wall function)

Table 4.3: Boundary conditions used for the `sedFoam` suspended sediment transport simulations.

| | Boundaries | | | | |
	inlet	outlet	top	bottom	walls
α_w	Dirichlet (`fixedValue`)	Neumann (`zeroGradient`)	Dirichlet-Neumann (`inletOutlet`)	Neumann (`zeroGradient`)	Neumann (`zeroGradient`)
pd	Neumann (`zeroGradient`)	Neumann (`zeroGradient`)	Dirichlet (`totalPressure`)	Neumann (`zeroGradient`)	Neumann (`zeroGradient`)
U	Dirichlet (SS prof.)	Dirichlet-Neumann (`inletOutlet`)	Dirichlet-Neumann (`inletOutlet`)	Dirichlet (`fixedValue`)	Dirichlet (`fixedValue`)
vS	Neumann (`zeroGradient`)	Neumann (`zeroGradient`)	Neumann (`zeroGradient`)	Neumann (`zeroGradient`)	Dirichlet (`fixedNormalSlip`)
k	Dirichlet (SS prof.)	Dirichlet-Neumann (`inletOutlet`)	Dirichlet-Neumann (`inletOutlet`)	Dirichlet (wall function)	Dirichlet (wall function)
ω	Dirichlet (SS prof.)	Dirichlet-Neumann (`inletOutlet`)	Dirichlet-Neumann (`inletOutlet`)	Dirichlet (wall function)	Dirichlet (wall function)
ν_t	Dirichlet (SS prof.)	`calculated`	`calculated`	Dirichlet (wall function)	Dirichlet (wall function)
c_s	Dirichlet (exp. prof.)	Neumann (`zeroGradient`)	Dirichlet-Neumann (`inletOutlet`)	Neumann (`zeroGradient`)	Neumann (`zeroGradient`)
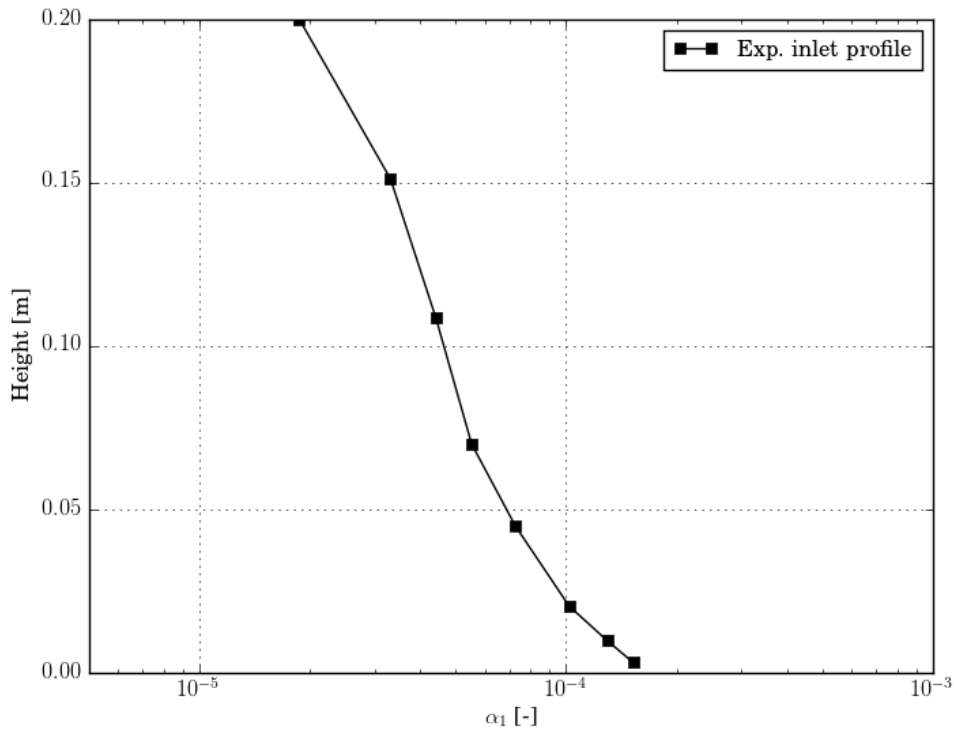
Figure 4.6: Inlet boundary condition of sediment volume fraction α_1 for the E-E and the VOF approaches.

Initial verifications of the polydispersity effects were carried out by running simulations for the D_{16} and D_{84} distributions diameters with all three formulations and comparing the results. The concentration profile comparisons at X = 2 m of the D_{16} and D_{84} diameters for the E-E simulations are shown in Figure 4.7. The concentration profile comparisons at X = 2 m of the D_{16} and D_{84} diameters for the VOF simulations with and without deposition, are shown in Figure 4.8. The differences between the VOF simulations with and without deposition turned out to be minute, with no ridge layers predicted in either case. Thisis probably due to the sediment concentration flux BC at the bottom. The E-E approach does not predict any ridge layers either, so both models agree with experimental observations on that aspect. However, the E-E model correctly predicts a saltation layer at the bottom with sediment concentration of the order of $O(10^{-3})$. This saltation layer formation is due to the drag term included in the E-E sediment momentum equations, but not in the VOF formulation. The drag term becomes increasingly important as the sediment volume fraction increases close the bottom. As a result, more momentum is extracted from the water phase as was seen in the saltating snow layer simulations. The saltating layer forming in the sediment simulations is not as intensive as the drifting snow one, since the sediment volume fraction at the bottom is just above the saltating threshold of 10^{-3}. Nonetheless, the saltating layer formation is a physical consequence of the non-perforated bottom wall BC in the E-E simulations. In the following sections, the E-E approach will only be compared to the VOF approach without deposition, and

to experimental measurements.
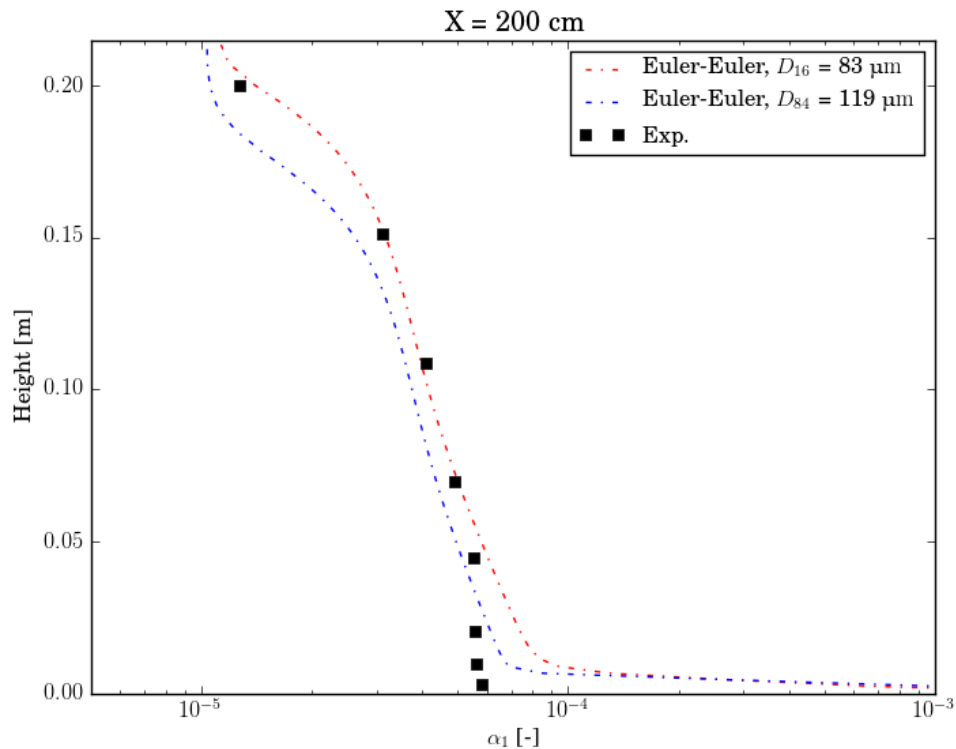
Figure 4.7: Concentration profile comparisons at X = 2 m of the D_{16} and D_{84} diameters for the E-E formulation.

4.3 Results and Discussion

4.3.1 The Suspended Sediment Volume Fraction Profiles

The simulation profiles of sediment volume fraction are shown with the experimental results in Figures 4.9 to 4.13, at the measurement stations X = 200, 300, 600, 800 and 1200 cm. Both models perform well in the suspension layer away from the bottom, with the E-E profile generally closer to the experimental measurements than the VOF model. Closest to the bed the E-E model predicts a saltating layer. This feature is very localized, which gives credibility to the results in the suspension layer. Close to the bottom, the VOF model agrees much better with the experimental measurements due to the sediment flux BC.

The E-E model has a tendency to produce constant sediment concentration close to the top boundary, which the free water surface modelled as a rigid lid. The effect of this BC becomes increasingly obvious downstream, and its suitability is put into question. The disagreement with experimental measurements increases as well in suspension in the downstream direction. There is less and less dispersion of particles into suspension, and this raises questions about turbulent dispersion from the bottom surface modelled with a
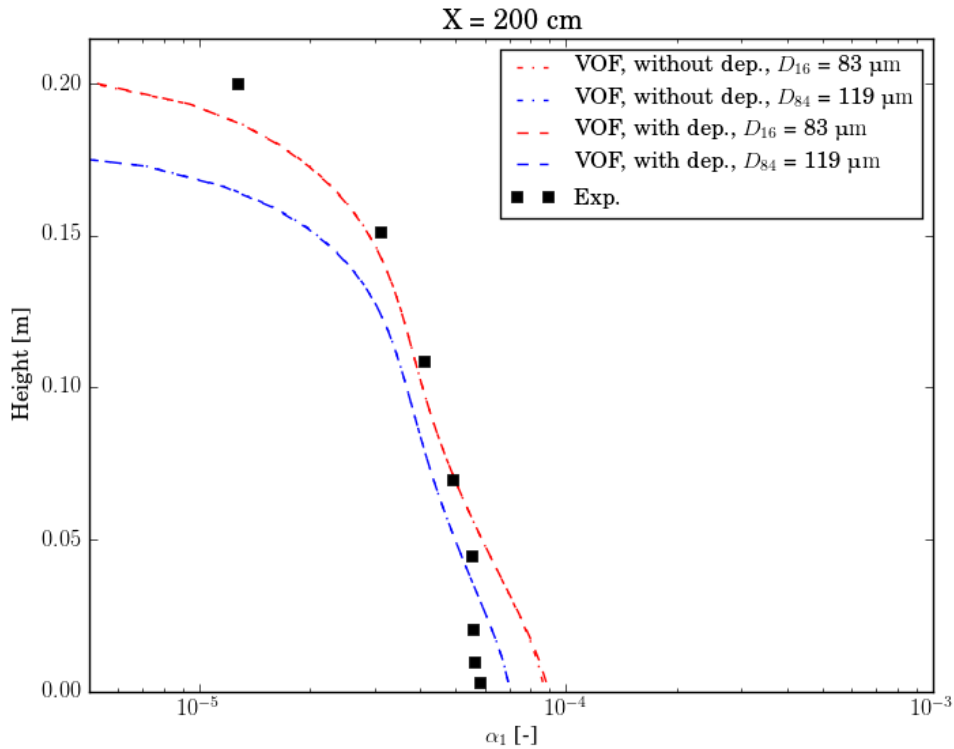
Figure 4.8: Concentration profile comparisons at X = 2 m of the D_{16} and D_{84} diameters for the VOF formulation, with and without deposition.

wall function as a non-perforated plate. This is also an issue with the VOF method since the sediment concentration conservation equation 1.38 uses turbulent dispersion on the RHS.

Overall, the present good agreement of the E-E model with experimental measurements is significant, since it highlights the model's ability to perform well when the particle size distribution is known. It also highlights the model's ability to perform well in one-way coupled situations, and for lower phase density ratios of order $O(1)$.

4.3.2   The Water Velocity Profiles

The advantage of solving a separate set of conservation equations for the sediment phase is quite obvious in the water velocity plots, shown in Figures 4.14 and 4.15. At X = 300 cm, the E-E water velocity profile is clearly closest to the experimental measurements, with the exception of the bottom part where the E-E predicts the saltation layer discussed previously. Accordingly, the E-E velocity profile at the bed shows a velocity deficit due to the larger presence of sediment particles in that region, and increased drag on the water flow. There, the one-way coupled VOF model velocity exceeds the experimental measurement. One would also expect the VOF approach to produce much better agreement close to the free surface where the flow is much more dilute than close the bed. Surprisingly, the VOF approach is showing a large velocity deficit there compared to the experimental
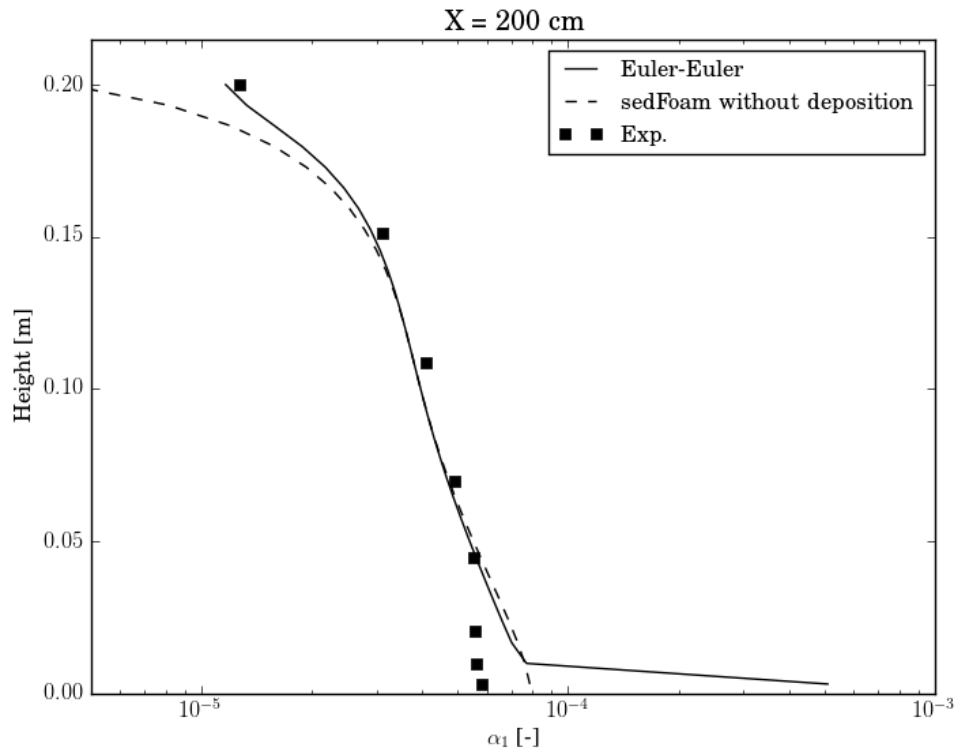
Figure 4.9: Comparison of sediment volume fraction α_1 for the E-E and the VOF approach to experimental measurement at X = 200 cm.
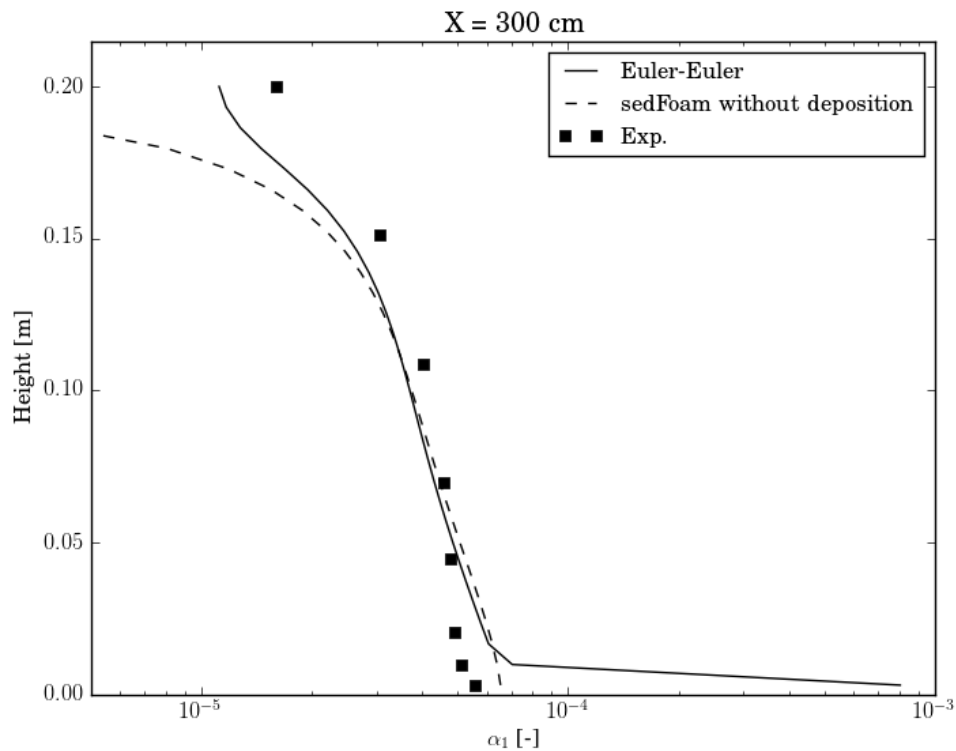
Figure 4.10: Comparison of sediment volume fraction α_1 for the E-E and the VOF approach to experimental measurement at X = 300 cm.
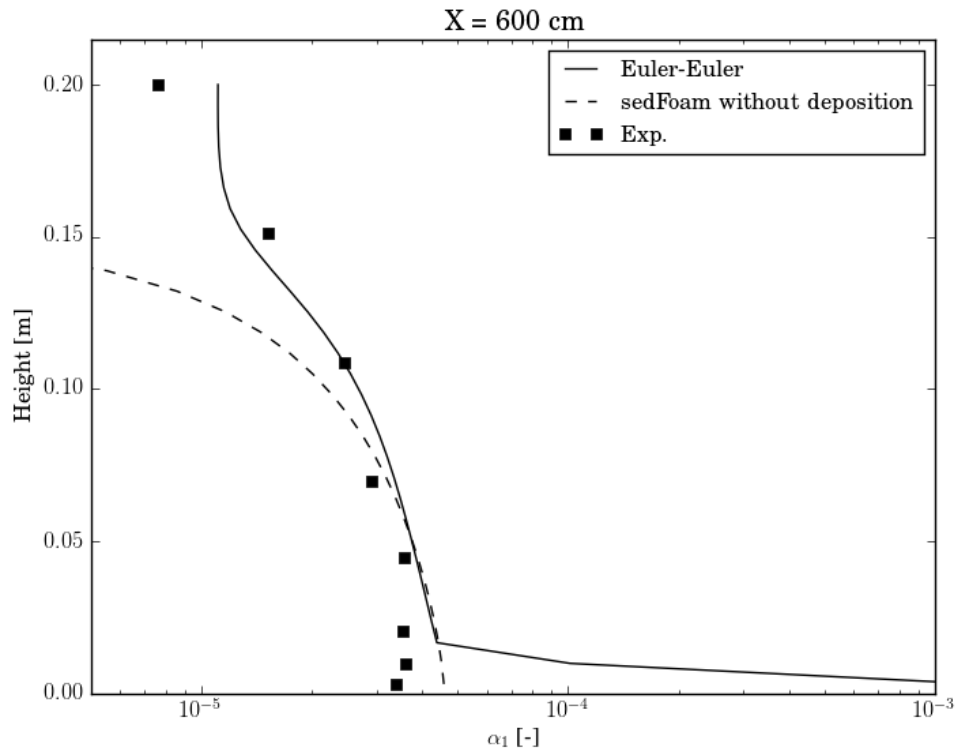
Figure 4.11: Comparison of sediment volume fraction α_1 for the E-E and the VOF approach to experimental measurement at X = 600 cm.
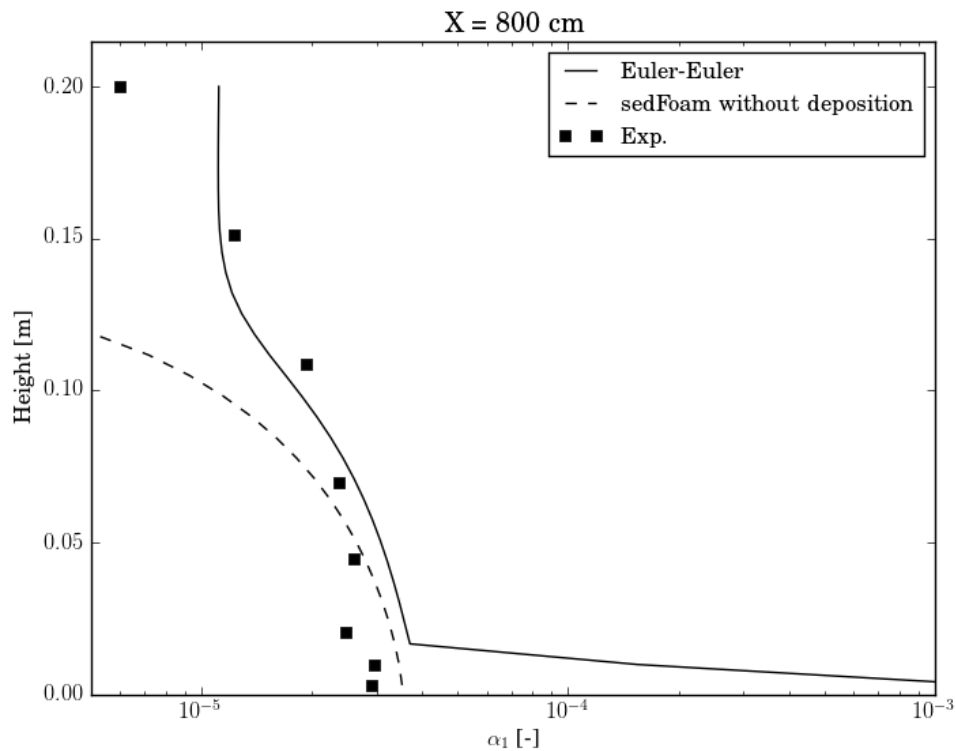
Figure 4.12: Comparison of sediment volume fraction α_1 for the E-E and the VOF approach to experimental measurement at X = 800 cm.
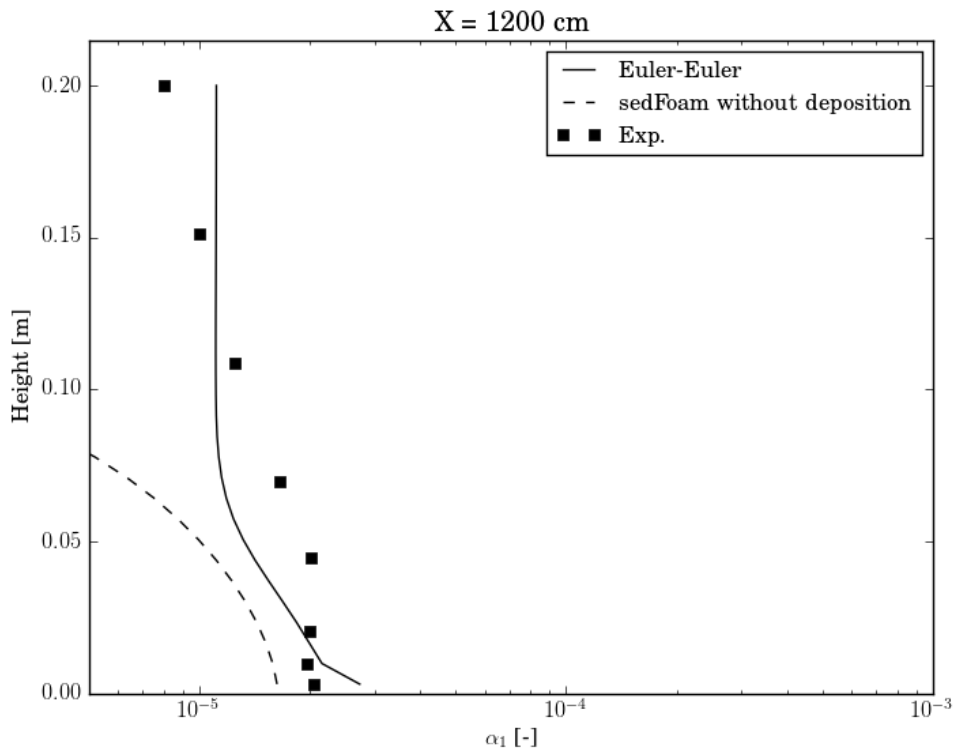
Figure 4.13: Comparison of sediment volume fraction α_1 for the E-E and the VOF approach to experimental measurement at X = 1200 cm.

measurement.

The water velocity profiles comparison at X = 785 cm, shown in Figure 4.15, shows a similar picture to the one at X = 300 cm. Here, the E-E profile again follows the shape of the experimental profile closest. Close to the bed we see the same physical velocity defect in the E-E profile, and the VOF profiles exceeding the experimental measurements. Near the free surface, the E-E profile is exceeds the experimental profile, and this is believed to be due to the flow becoming more and more dilute downstream. The VOF profiles are closer to the experimental measurements than at X = 300 cm, but they still underestimate them.

4.3.3 The Suspended Sediment Settling Velocity

The sediment settling velocity is essentially the vertical component of the sediment relative velocity ω_s with respect to the water flow, which is calculated as [130],

$$\omega_s = w_s - w_w. \tag{4.1}$$

Here, w_s and w_w are respectively the sediment and water vertical velocity components. The drift velocity used in equation 1.56 is neglected since sediment turbulent dispersion is already accounted for by the turbulent drag term of equation 2.11.

The sediment relative velocities calculated with the E-E approach are plotted in Fig-
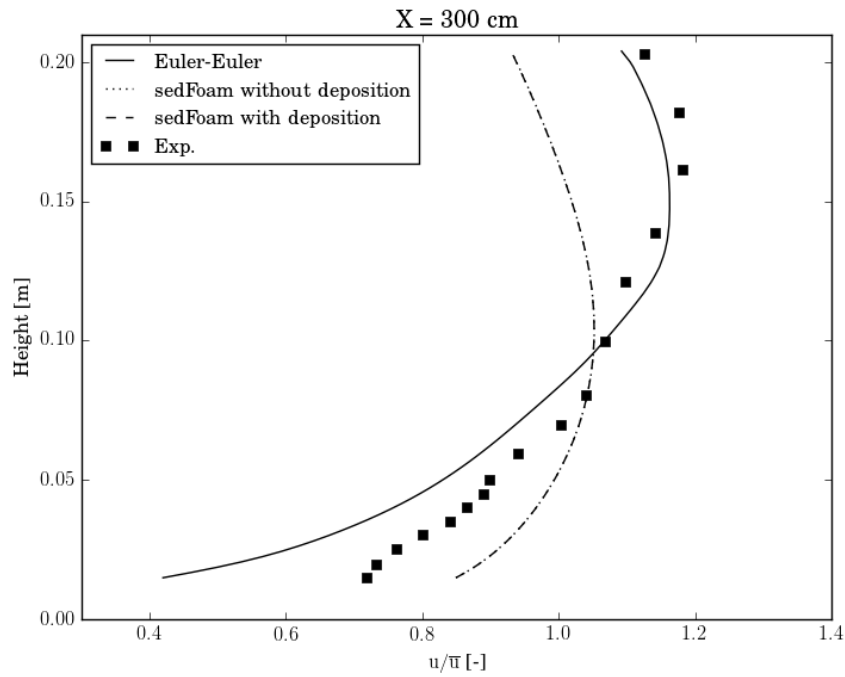
Figure 4.14: Comparison of simulations profiles of normalized water velocity to experiment at X = 300 cm for the E-E and the VOF approaches.
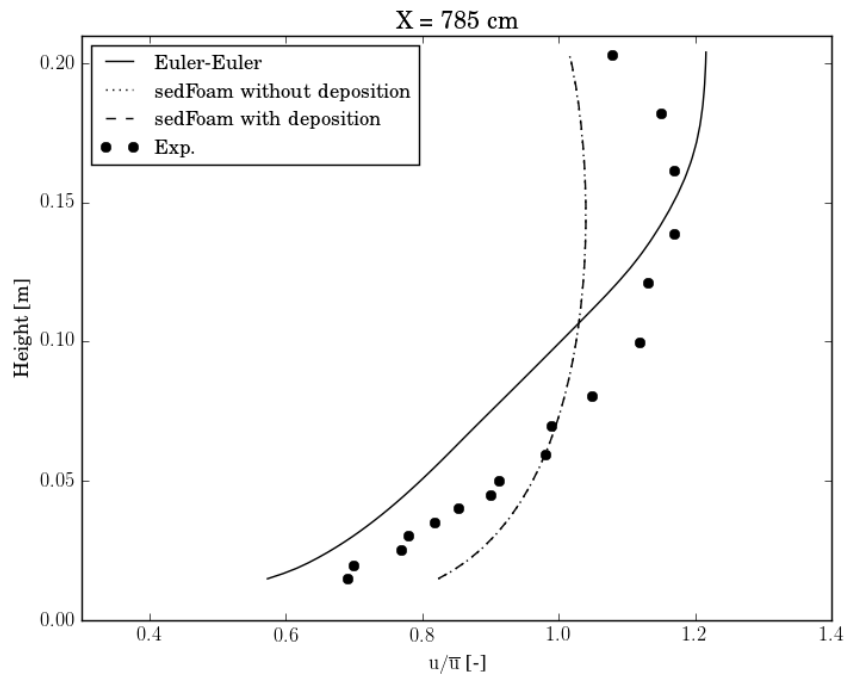
Figure 4.15: Comparison of simulations profiles of normalized water velocity to experiment at X = 785 cm for the E-E and the VOF approaches.

ures 4.16 and 4.17 for X = 300 cm and X = 785 cm, respectively. The average sediment settling velocities in the E-E simulations were -0.0069 m $\cdot$ s^{-1} and -0.0070 m $\cdot$ s^{-1} at X = 300 cm and X = 785 cm, respectively. These values match perfectly the average settling velocity of -0.007 m $\cdot$ s^{-1} measured in the experiment. The empirical sediment settling velocity calculated by `sedFoam`, which is constant across the flow, is -0.0067 m $\cdot$ s^{-1}. These findings are reported in Table 4.4. Furthermore, the very localized effect of the boundary on the settling velocity profiles indicates that the E-E results in the rest of the flow should be reliable.
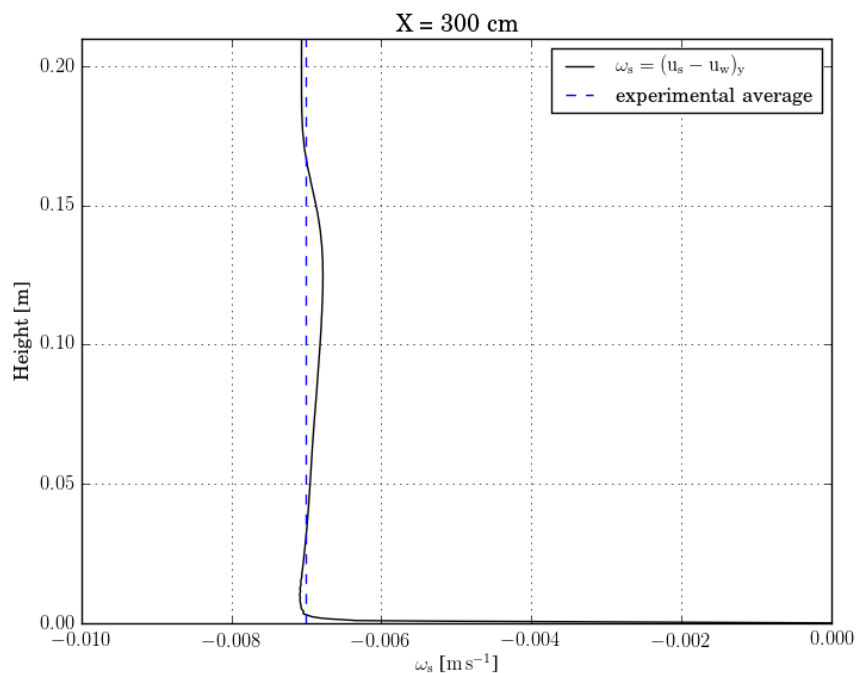
Figure 4.16: Simulation sediment relative velocities at X = 300 cm for the E-E approach.

Table 4.4: Comparison of the numerically calculated and experimentally measured average sediment settling velocities.

Experimental average	-0.007 m $\cdot$ s^{-1}
E-E, X = 300 cm	-0.0069 m $\cdot$ s^{-1}
E-E, X = 785 cm	-0.0070 m $\cdot$ s^{-1}
VOF	-0.0067 m $\cdot$ s^{-1}
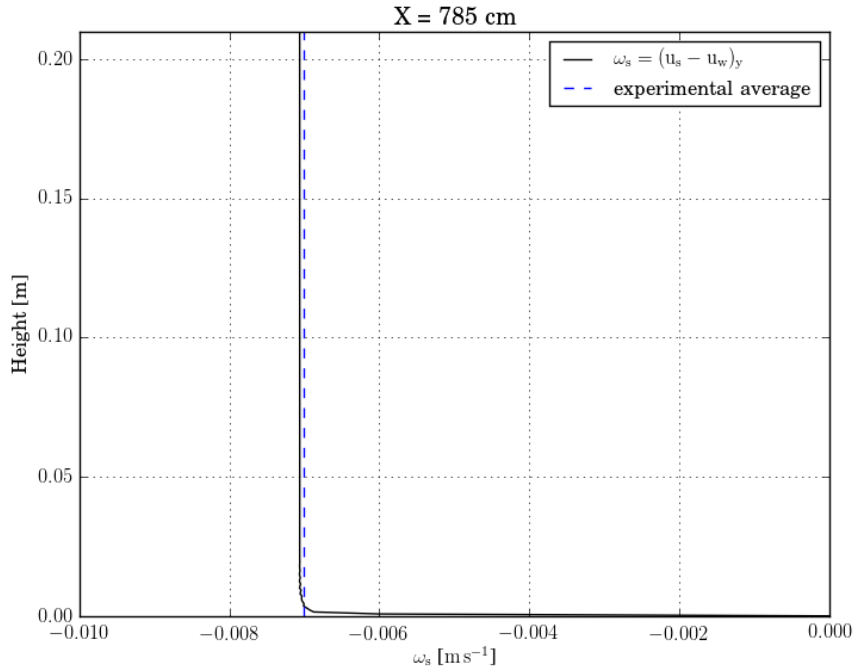
Figure 4.17: Simulation sediment relative velocities at X = 785 cm for the E-E approach.

4.3.4   Discussion on the Validity of the Bottom Boundary Condition

The effect of the bottom wall function BC used here turned out to be very localized for the E-E and VOF models, but is it really representative of flow over a perforated bottom? The experimental water velocity profiles in Figure 4.3 show the velocity profile is not logarithmic at the bottom, unlike what is expected from a wall function. Moreover, the progressively poor agreement in sediment concentration downstream raises questions about the turbulent dispersion, wich is greatly affected by the wall function. A closer look at the physical nature of such a flow is then required. Perforated bottoms within hydrodynamic flows have been studied extensively for configurations quite similar to the present validation experiment. A comprehensive review is outside the validation scope, so only a couple of directly relevant publications are discussed below.

Celik and Rockwell [160] study a hydrodynamic system with a freestream velocity of $0.126 \ \mathrm{m \cdot s^{-1}}$ over a regular arrangement of perforations of diameter 6.4 mm with an open area ratio of 68.6 %. They note the formation of self-sustained oscillations, as well as large-scale patterns of vorticity concentration and streamline topology, similar to those occurring in free-shear flows. Ozalp *et al.* [161] investigate the case of freestream velocity of $0.24 \ \mathrm{m \cdot s^{-1}}$, perforations of minimum diameter 6.4 mm and an open area ratio of 69 %. They also report the formation of highly coherent self-sustained oscillations of the shear flow over the perforations, with local vortex shedding from each perforation and unsteady pressure fluctuations. Moreover, a hydrodynamic instability with a wavelength

much longer than the perforation diameter rapidly emerges well above the background turbulence level. Ozalp *et al.* [161] find that the intensity of the coherent structures increases with decreasing perforation diameter, and that the structures get closer to the bottom surface. The freestream velocity in the sediment suspension experiment simulated here is about twice that of Ozalp *et al.* [161], and the perforation diameter about half, implying similar Reynolds numbers based on perforation diameter. The halving of the open area in the present experiment can result in less coherent structures and reduced vorticity levels, but a flow substantially different from a typical flat plate shear layer is expected.

Sediment particles are present in larger concentrations upstream, but the heaviest particles will be flushed earlier from the bottom in the most upstream part of the flume due to their higher inertia. The experimental measurements indicate a clearly dilute and one-way coupled flow from the computational inlet on, so no turbulence damping effect is to be expected from the suspended sediment. The coherent structures forming over the perforated bottom are then quite likely to intensify downstream as observed in the experiments of Celik and Rockwell [160] and Ozalp *et al.* [161].

Finally, the wall functions used as boundary conditions for the E-E and VOF simulations are derived from analysis of fully developed shear layers over flat plates, and fitted to such experimental data. Even with roughness effects the resulting wall functions are clearly not applicable to water flumes over perforated plates, and the vorticity production in the experiment is most certainly very different from what the wall functions predict. This has direct implications on the turbulent viscosity field, which affects the turbulent drag term in the E-E approach, and the turbulent dispersion term on the RHS of the convection-diffusion sediment transport equation of the VOF formulation. Instead of wall functions, it is desirable to use a low Reynolds number turbulence model with the bottom perforations directly represented. This will also help explain the dual role of the perforations in flushing sediment and generating turbulence.

4.4 Conclusions

The new Eulerian-Eulerian model was successfuly validated against sediment concentration and water velocity measurements in a laboratory suspension flume over a perforated bottom. Comparison was also done to the predictions of a one-way coupled Volume of Fluid model using a convection-diffusion transport equation for the sediment phase. The Eulerian-Eulerian model was found able to accurately predict the suspended sediment concentration profiles, and generally better than the Volume of Fluid model, which systematically underestimates them. Moreover, the Eulerian-Eulerian model managed to predict the water velocity profiles more accurately than the one-way coupled model.

The Eulerian-Eulerian model calculated very accurately the average sediment settling

velocity, which needs to be imposed beforehand in the one-way coupled model using empirical relationships. The settling velocity profiles indicate the bottom boundary condition effect is very localized and does not affect the rest of the flow.

The present results validate the Eulerian-Eulerian model in suspension layers for monodisperse particle size distributions, and phase density ratios of order $O(1)$. Such a validation is complementary to the drifting snow validation for saltating flows with polydisperse particle size distributions, and discrete to continuous phase density ratios of order $O(100)$.

A wall function boundary condition for non-perforated surfaces was examined and found unsuitable for representing perforated surfaces. This is because a wall function boundary condition for non-perforated surfaces most likely produces a very different turbulent flow than what would actually occur along a perforated bottom. Inaccurate turbulence generation by the wall function boundary condition could be a factor in the poor agreement in sediment concentration profiles at the downstream measurement stations for both models. Instead of wall functions, it is recommended to use a low Reynolds number turbulence model, with true representation of the bottom perforations.

Chapter 5

Particle Viscosity Model Validation

As discussed in section 1.3, the usual approach to assessing the particle phase viscosity is to derive it from empirical or theoretical expressions of the mixture viscosity, using equation 1.27. Here, the particle viscosity model of equation 2.34 is validated by following the inverse approach. The particle phase viscosity from equation 2.34 is used to calculate the mixture viscosity per equation 1.27. The mixture viscosity is then compared to the results of the mixture viscosity models discussed in section 1.3.

The E-E mixture viscosity was calculated from the numerical results using two approaches. The first one $\mu_{m,U}$ is an estimation of the mixture viscosity based on the mixture velocity gradient and the sum of the shear stresses in the particle and fluid phases,

$$\mu_{m,U} = \frac{\alpha_1 \tau_1 + \alpha_2 \tau_2}{\partial U_m / \partial z}.$$
(5.1)

Here, τ_1 and τ_2 are respectively the shear stresses in the particle and fluid phases, and $U_m = \alpha_1 U_1 + \alpha_2 U_2$ is the mixture velocity. The second E-E mixture viscosity estimate, $\mu_{m,\alpha}$ is calculated according to the conventional volume fraction weighting of equation 1.27.

The mixture viscosity validation is complemented with one for the particle phase alone. At the current validation experimental drifting snow temperature T = 263 K, and using the snowbed density $\rho_1 = 361$ kg $\cdot$ m^{-3}, one gets from the KS model of equation 1.97 a snow viscosity $\mu_1 = 5.142$ kg $\cdot$ m^{-1} $\cdot$ s^{-1} across all transport layers. Such a value could make sense for a bonded and hardened snowbed, but it is extremely high for drifting snow [162, 163]. Instead, it is suggested that equation 1.97 be modified by adjusting ρ_1 to the local volume fraction. Inserting an additional multiplicative constant in equation 1.97, we get the following expression that is used for the current validation,

$$\mu_1 = A_{ks} \mu_0 e^{-aT} e^{\beta \alpha_1 \rho_1}.$$
(5.2)

Particle phase viscosities obtained with equation 5.2 are smaller than those obtained using equation 1.97 by a factor of $A_{ks} e^{(\alpha_1 - 1)\beta \rho_1}$. For typical values of $\alpha_1 \approx 10^{-3}$ in a saltating

layer, and $\rho_1 \approx 10^3$ in the current snow and sediment transport experiments, this ratio is of the order of $O(A_{ks} \times 10^{-3})$.

5.1 The Snow Viscosity Results

The validation is carried out for the 0.1 mm particle class, which exhibits creep, saltation, and suspension in the experiment. A snapshot of the snow phase volume fraction at X = 3 m is shown in Figure 5.1, with the airflow velocity vectors superimposed on the snow volume fraction in shades of white. One can clearly see the momentum extraction effect of the particles on the airflow velocity in the lower and denser parts of the snowbed. The mixture dynamic viscosity comparisons are shown in Figure 5.2. The Brinkman and Roscoe model was not retained for the comparison since it was found to give similar results to the Einstein model. The mixture viscosity models included are the Einstein model (equation 1.87), the Ishii model (1.91), and the Graham model (1.92). The snow phase volume fraction profile is also shown to differentiate the dense parts of the flow from the dilute ones. Firstly, it is noted that the two ways to calculate the E-E mixture viscosity are equivalent, and practically indistinguishable for $\alpha_1 < 0.05$. Secondly, all results are equivalent for a height z > 0 cm, which corresponds to $\alpha_1 < 0.03$, and happens to be the validity threshold of the Einstein model. For z > 4 cm, which corresponds to $\alpha_1 < 0.011$, all five curves collapse to the air phase dynamic viscosity value $\mu_2 = 1.69 \times 10^{-5}\,\mathrm{kg} \cdot \mathrm{m}^{-1} \cdot \mathrm{s}^{-1}$. This region is also the top of the saltation layer where the two-way coupling effects of the snow phase on the air phase are vanishing quickly. For z < 0 cm, which corresponds to $\alpha_1 > 0.03$, the Einstein and Ishii models give similar results. This is surprising since the Ishii model is known to be valid at all concentrations, while the Einstein model is only valid at low concentrations. Moreover, the Graham model and the present E-E model diverge progressively from the previous two as the snow volume fraction increases. The Graham and E-E models are very close up til $\alpha_1 \approx 0.07$, where the E-E curve increases sharply. This is due to the $\tau_t/\dot{\gamma}_1$ term in equation 2.34, which contains an implicit contribution of particle bonding and collisions. None of these effects are taken into consideration in the Einstein, Ishii, and Graham models. Moreover, the E-E model explicitly accounts for particle phase shear stress and rate of strain, whereas the other models use a correction to the fluid phase viscosity based on particle volume fraction. The E-E model is therefore more physical.

The profile of kinematic viscosity ν_1 of the E-E model for $d_p = 0.1$ mm at X = 3 m is shown in Figure 5.3, and compared to the kinematic viscosity profiles of the CC model (equation 1.94), and the KS model (equation 5.2). The comparison is restricted to the bottom 2 cm where the particles are in saltation and the particle volume fraction is between 2×10^{-2} and just over 10^{-1}, which is a weakly dense regime. The E-E kinematic viscosity profile in Figure 5.3 indicates that the snow phase can indeed be considered
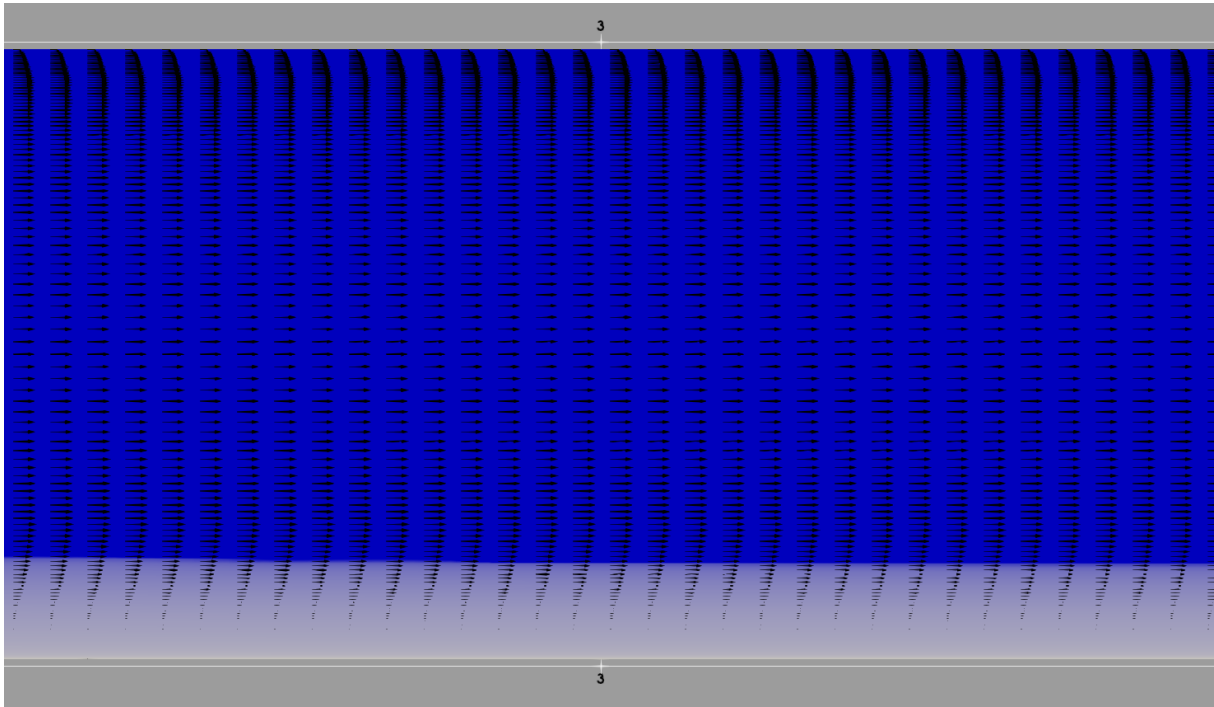
Figure 5.1: E-E simulation snow phase volume fraction and airflow velocity vectors for $d_p = 0.1$ mm at X = 3 m.
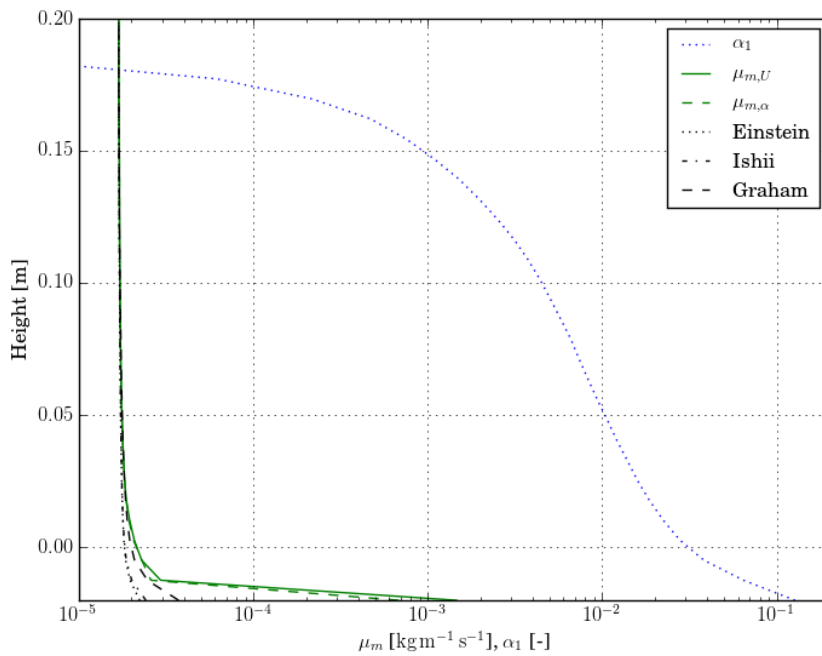
Figure 5.2: Comparisons of the E-E simulation air-snow mixture dynamic viscosities to the Einstein model (equation 1.87), the Ishii model (equation 1.91), and the Graham model (equation 1.92), for $d_p = 0.1$ mm at X = 3 m.

inviscid in the saltation and suspension layers. The only appreciably viscous region is the lowest part of the saltation layer, well within the tunnel gutter, just outside the validity threshold of the Einstein mixture viscosity model.

The CC and KS model values are plotted in Figure 5.3 as well. The good agreement of the CC model with the E-E model stems from setting the constant A_{cc} to the following expression,

$$A_{cc} = \frac{\alpha_1}{\alpha_2} \cdot \frac{\rho_1}{\rho_2}. \tag{5.3}$$

In this form, A_{cc} is essentially the ratio of local density corrected to volume fraction. This correction seems reasonable considering the CC model is derived based on strain ratio, which should correlate with density ratio for incompressible phases.

The values of the KS model have merely been adjusted by $A_{ks} = 0.1$. A density ratio correction was not necessary for the KS model, which already has a density exponential term with a volume fraction correction. More validations are necessary to confirm these findings.

Figure 5.3: Comparisons of the E-E simulation snow phase kinematic viscosity ν_1 to the CC model (equation 1.94) and KS model (equation 5.2), for $d_p = 0.1$ mm at X = 3 m.

Finally, in Figure 5.4 the numerical snow phase kinematic viscosity ν_1 is compared to the snow phase effective viscosity $\nu_{eff1} = \nu_1 + \nu_{t1}$, which includes the turbulent component. ν_1 is non-dimensionalized by ν_{eff1}, and ν_{eff1} by the air phase effective viscosity, $\nu_{eff2} = \nu_2 + \nu_{t2}$. The aim of this comparison is to determine how ν_1 compares to ν_{eff1}, and how ν_{eff1} compares to ν_{eff2}. The snow phase laminar viscosity is found to be non-negligible compared to the effective viscosity, and by extension the snow phase turbulent viscosity

ν_{t1}. The reason is that $\nu_{t1} = C_t^2 \nu_{t2}$, and C_t is of order $O(10^{-3})$ as seen in Figure 5.4. C_t (see equation 2.18) is so small because of the ratio of the densities of the dispersed to the continuous phase in its denominator, which is of order $O(100)$ here. Therefore, C_t^2 is of order $O(10^{-6})$ and the ensuing turbulent viscosity component is quite modest compared to the air phase turbulent viscosity. However, ν_{eff1} is four to five orders of magnitude smaller than ν_{eff2}. This indicates that the particle viscous transport, be it molecular or turbulent, is negligible. Therefore, particle dispersion relies entirely on the turbulent drag term for aeolian transport of solid particles.
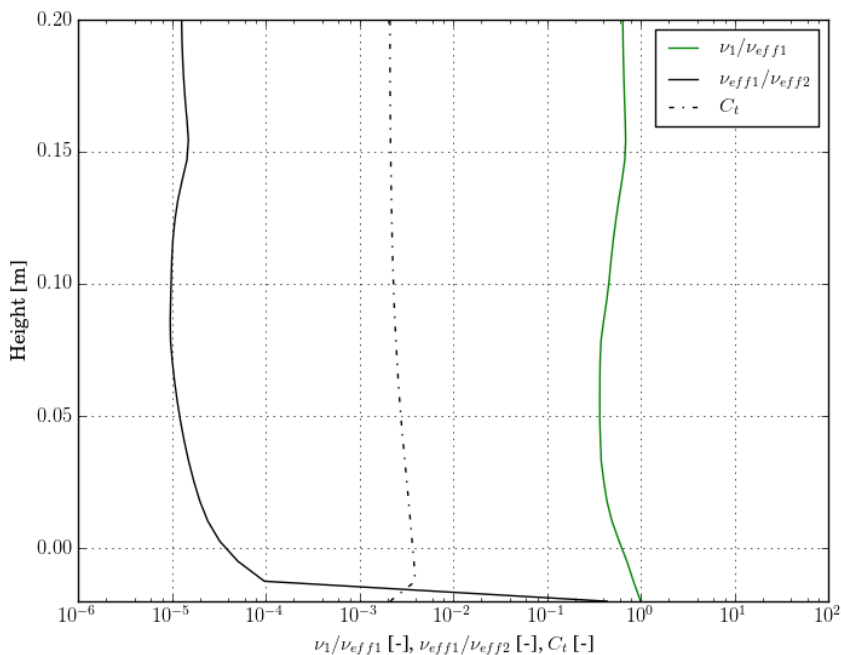
Figure 5.4: Comparisons of the E-E simulation snow phase kinematic viscosity ν_1, effective viscosity ν_{eff1}, and air phase effective viscosity ν_{eff2}, for $d_p = 0.1$ mm at X = 3 m.

5.2   The Sediment Viscosity Results

The same analysis carried out above for snow transport is repeated here for sediment transport. First, a snapshot of the sediment volume fraction with the water flow velocity vectors for $d_p = 0.1$ mm at X = 2 m is shown in Figure 5.5. In contrast to the flow snapshot of the denser and mostly saltating snow field in Figure 5.1, the dilute and suspended sediment field extends here all the way to the top of the domain and the velocity vectors are unaffected by the sediment phase. This is due to the fact that the sediment volume fraction is below 10^{-3} at the bottom, which is the limit of the two-way coupled regime. This can be verified in Figure 5.6, the equivalent of Figure 5.2 for the snow. Figure 5.6 also shows comparisons of the E-E mixture viscosities $\mu_{m,U}$ and $\mu_{m,\alpha}$ to the Einstein,

Ishii, and Graham mixture viscosities. Since the flow is dilute, all mixture viscosities give the same results, the dynamic viscosity of water $\mu_2 = 1.15 \times 10^{-3}\,\mathrm{kg \cdot m^{-1} \cdot s^{-1}}$. It is interesting to note that the two E-E mixture viscosities, $\mu_{m,U}$ and $\mu_{m,\alpha}$ diverge significantly at $\alpha_1 \approx 8 \times 10^{-5}$, much lower than than $\alpha_1 \approx 5 \times 10^{-2}$ for the denser snow simulations.
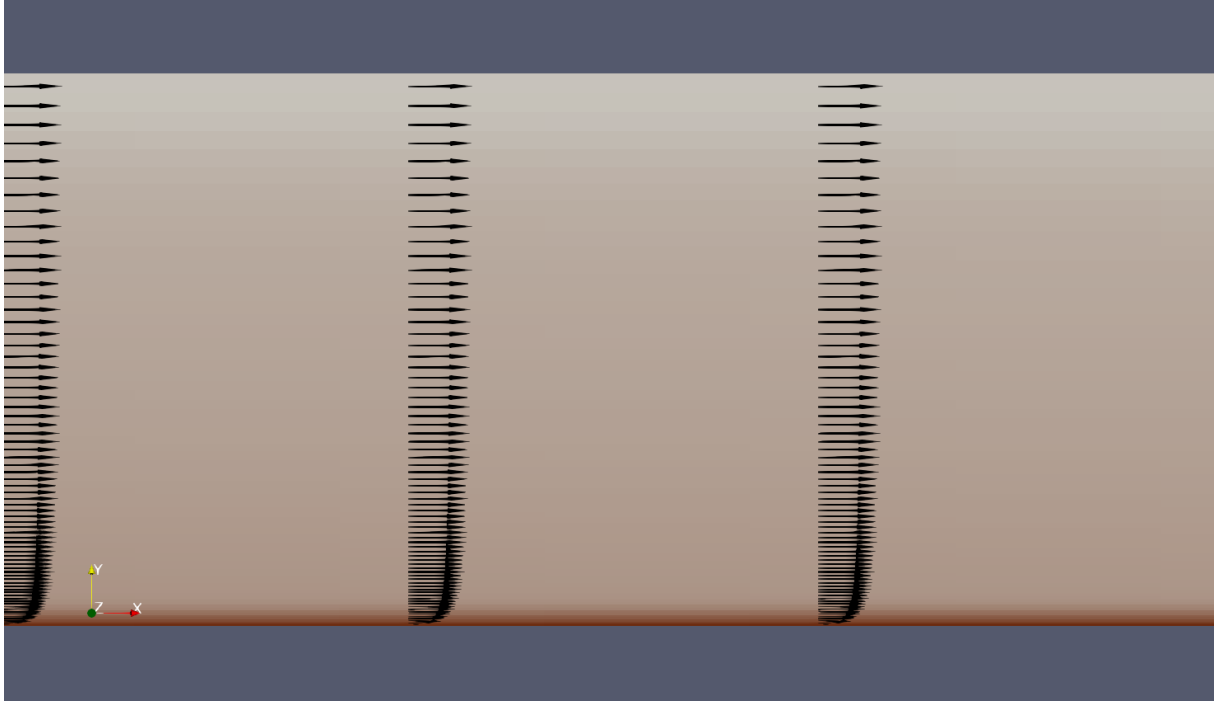
Figure 5.5: E-E simulation sediment phase volume fraction and water flow velocity vectors for $d_p = 0.1$ mm at X = 2 m.

In Figure 5.7, the sediment phase E-E kinematic viscosity model is compared to the CC and KS kinematic viscosity models of equations 1.96 and 5.2. The comparisons are restricted to the first 5 cm above the bottom, where the sediment concentration is between 10^{-5} and just over 10^{-3}, a dilute regime. The present vicosity profile of the E-E model is a couple of orders of magnitude larger than the profile of drifting snow in Figure 5.3. This is because the sediment volume fractions are much lower here, and the drag force term in equation 2.35 accordingly. The E-E model profile shows again that the sediment phase can be considered inviscid in the suspension layer, except in the lowest part where the saltation layer begins to develop. Here, the CC and KS model constants are set to 1 since the corrections that proved successful for drifting snow did not work for suspended sediment. The three viscosity profiles do not agree with each other. Little is known about the derivation of the KS model, but the strain ratio analogy behind the derivation of the CC model might be invalid in dilute regimes. As for the E-E model, it is derived for creeping and saltation layers with volume fractions of order $O(d-3)$ and more. Accordingly, the E-E model proved successful in the denser drifting snow, but does not seem to work as well here in the much more dilute suspended sediment.

In Figure 5.8, the sediment phase kinematic viscosity is compared to the sediment
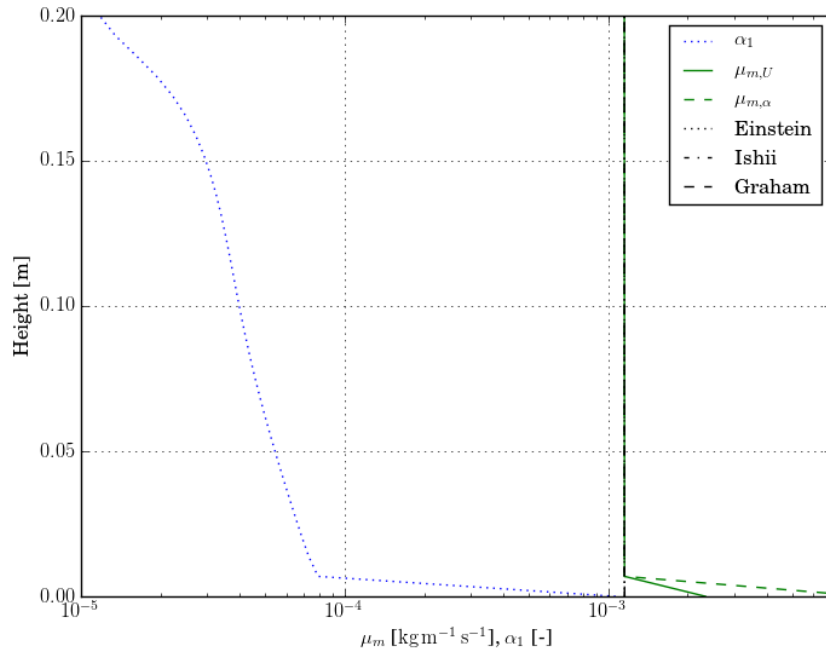
Figure 5.6: Comparisons of the E-E simulation water-sediment mixture dynamic viscosities to the Einstein model (equation 1.87), the Ishii model (equation 1.91), and the Graham model (equation 1.92), for $d_p = 0.1$ mm at X = 2 m.
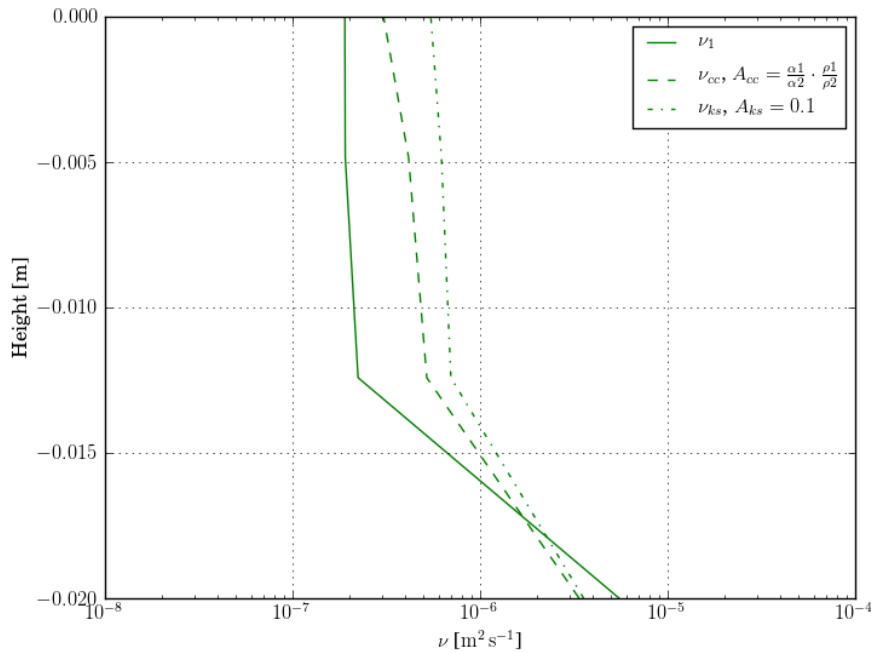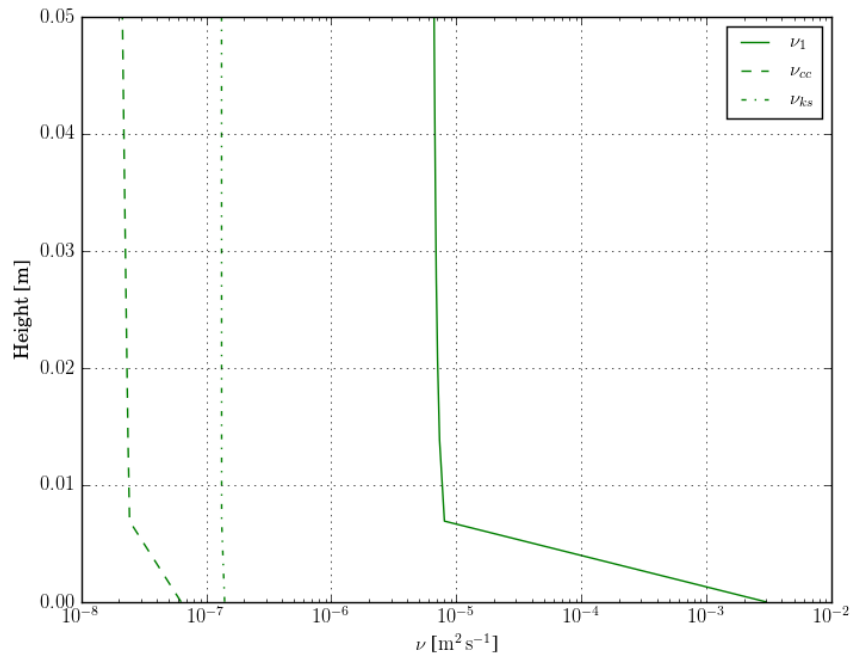

Figure 5.7: Comparisons of the E-E simulation sediment phase kinematic viscosity ν_1 to the CC model (equation 1.94) and KS model (equation 5.2), for $d_p = 0.1$ mm at X = 2 m.

phase effective viscosity, and the latter is compared to the water phase effective viscosity. The comparisons are done by means of non-dimensionalization just like the drifting snow case, but show opposite trends. The sediment laminar kinematic viscosity is found negligible compared to the sediment effective kinematic viscosity. This is due to the substantially larger C_t, which is practically constant at just below 0.5 for the entire flow, and two orders of magnitude larger than for the snow case. As such, the turbulent contribution dominates in ν_{eff1}. The turbulent term domination results also in the phase effective viscosities ratio being proportional to C_t^2, except close to the bottom where the water turbulent viscosity is at its lowest and the sediment laminar kinematic viscosity is at its highest. Unlike aeolian transport of solid particles, particle turbulence is found to be relevant for hydrological transport of solid particles, along with the turbulent drag. In retrospect, this could help explain why the kinematic viscosity comparisons to the CC and KS models was successful for the laminar drifting snow flow, but not for the turbulent sediment transport flow. The E-E model is derived for laminar conditions, and it could very well be the case for the CC and KS models.
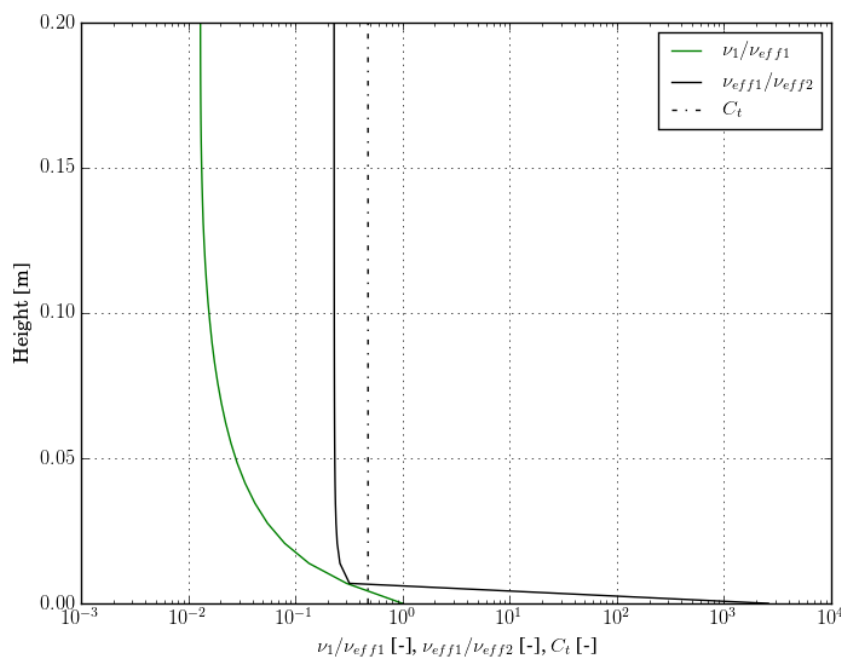
Figure 5.8: Comparisons of the E-E simulation sediment phase kinematic viscosity ν_1 and effective viscosity ν_{eff1}, to the water phase effective viscosity ν_{eff2}, for $d_p = 0.1$ mm at X = 2 m.

5.3 Conclusions

The mixture viscosity obtained from the present Eulerian-Eulerian particle viscosity model shows good agreement with mixture viscosity models from the literature. Deviations are

noted in the dense particle regime, and they are attributed to the threshold shear stress term in the Eulerian-Eulerian viscosity model. In general, the other mixture viscosity models are found to lack representation of many relevant particle phase physical phenomena, such as drag forces, shear stresses, threshold shear stress and rate of strain.

Comparisons to particle viscosity models from the literature pointed out similar discrepancies in their formulations to those noted above for mixture viscosity models. The particle viscosity models are also found to lack representation of the relevant shear stresses and rate of strain. These two aspects are explicitly accounted for in the Eulerian-Eulerian model, and constitute a unique feature. Both Carrier-Cashwell and Kazhikov-Smagulov viscosity models agree well with the Eulerian-Eulerian model in dense laminar regimes, provided their multiplicative constants are adjusted. The authors of the CC model quote the multiplicative constant A_{cc} to be of order $O(1)$, but it was necessary to use a variable constant equal to the local phase density ratio for good agreement with the E-E model. An additional volume fraction correction needed to be introduced within the density exponential in the Kazhikov-Smagulov model, along with a multiplicative constant of 0.1 for good agreement with the E-E model. It is desirable to validate the introduced corrections over a wider set of particle-laden flows. In the dilute and turbulent suspended sediment transport regime, the three particle viscosity models were orders of magnitude apart, raising questions about their suitability for such regimes, which are after all inviscid.

In the dilute suspended regime the volume fraction weighted approach to calculating the mixture viscosity was found to agree very well with calculations based on the volume fraction weighted phase shear stresses and the mixture rate of strain. Substantial deviations are noted in the dense regime.

The particle to fluid density ratio is found to be a determining factor in the C_t magnitude, and for the degree of turbulent contribution to the phase effective viscosity. A density ratio of order $O(100)$ for drifting snow, and most aeolian transport of solid particles, results in a small turbulent contribution comparable to the snow phase laminar viscosity. Moreover, the snow phase effective viscosity becomes negligible compared to the air phase effective viscosity, and the snow phase can then be considered inviscid compared to the air phase. Therefore, turbulent drag seems to be the only relevant dispersion mechanism for aeolian transport of solid particles. On the other hand, a density ratio of order $O(1)$ for suspended sediment in water results in a large turbulent contribution that dominates the sediment phase laminar viscosity. As such, the sediment phase effective viscosity becomes comparable to the water phase effective viscosity, and the sediment phase cannot be considered inviscid compared to the water phase. Particle turbulence is then found to be relevant for hydrological transport of solid particles, along with the turbulent drag.

Chapter 6

Conclusions and Recommendations

A new Eulerian-Eulerian two-way coupled approach for the simulation of solid particle-laden flows has been proposed and validated. The present approach includes a new purposely developed particle viscosity model developed from first principles, and relies on the $k - \epsilon$ and $k - \omega$ SST turbulence models for the continuous phase turbulence modelling. The particle phase turbulence is modelled using the Gosman model [130], as simplified by Issa and Oliveira [139]. Unlike other mixture-based methods for simulating solid particle-laden flows, the present approach does not rely on empiricism or equilibrium approximations. Particle dispersion is accounted for based on turbulent drag.

A first validation is done against the experimental results of a drifting snow experiment with a discrete to continuous phase density ratio of order $O(100)$. When taking the polydisperse characteristics of a controlled drifting snow experiment into consideration, the new Eulerian-Eulerian approach correctly predicts the snow flux profiles in the saltation layer and the lower suspension layer, as well as the snow transport values, at all experimental measurement stations. Polydispersity was accounted for by combining the results of several monodisperse simulations using the statistical weights of a two-parameter Γ distribution. Furthermore, the new approach correctly predicts the airflow velocity profiles at all measurement stations. The new Eulerian-Eulerian approach was found to perform well in the equilibrium and non-equilibrium parts of the experiment. The turbulent kinetic energy experimental profile was overestimated with the new Eulerian-Eulerian approach, in agreement with other similar implementations. This result, however, is inconclusive since the experimental measurements did not include turbulent kinetic energy at frequencies higher than $20Hz$.

A second complementary validation was done against the experimental results of a laboratory flume experiment over a perforated bottom, with monodisperse particle size distributions, and discrete to continuous phase density ratio of order $O(1)$. The Eulerian-Eulerian approach was found able to accurately predict the suspended sediment concentration and velocity profiles, and generally better than the one-way coupled Volume of Fluid approach using a convection-diffusion transport equation for the sediment phase.

Furthermore, the Eulerian-Eulerian approach calculated very accurately the average sediment settling velocity, which needs to be imposed beforehand in the one-way coupled approach using empirical relationships.

The effect of a non-perforated bottom boundary condition used to represent a perforated bottom was found very localized, and not affecting the rest of the flow when using the Eulerian-Eulerian approach. Using a wall function boundary condition in such situations was found unsuitable, since a perforated bottom would produce turbulent structures very different from those produced over a non-perforated bottom. A different dispersion effect would result, and it is recommended instead to use a low Reynolds number turbulence model without wall functions, with true geometric representation of the surface perforations.

A third and final validation was done for the new particle viscosity model. The mixture viscosity derived from the present Eulerian-Eulerian particle viscosity model agrees well with mixture viscosity models from the literature in the dilute suspended regime. Deviations are noted in the dense particle regime, due to the threshold shear stress term in the Eulerian-Eulerian viscosity model. Unlike the present particle viscosity model, other mixture viscosity models generally lack representation of many relevant particle phase physical phenomena, such as drag forces, shear stresses, threshold shear stress, and rate of strain. In the dilute suspended regime the volume fraction weighted approach to calculating the mixture viscosity was found to agree very well with calculations based on the phase shear stresses weighted by volume fraction and the mixture rate of strain. This is applicable to both experiments investigated with dispersed to continuous particle density ratios of orders $O(100)$ and $O(1)$.

Comparisons to particle viscosity models from the literature point out similar discrepancies in their formulations. The Kazhikov-Smagulov particle viscosity model required a multiplicative constant of 0.1, and a volume fraction correction in its exponential density term, in order to agree with the more physical Eulerian-Eulerian model in the dense and laminar drifting snow regime. In the same situation, the Carrier-Cashwell model required a variable constant equal to the local phase density ratio, as opposed to the constant of order $O(1)$ quoted by the original authors. The three particle viscosity models were orders of magnitude apart in the turbulent and dilute suspended sediment transport regime. This raises justified questions about their suitability for inviscid and turbulent particle flow regimes.

The particle to fluid density ratio was found to be a determining factor in the C_t magnitude, and the magnitude of the dispersed particle phase effective viscosity. A density ratio of order $O(100)$ for drifting snow results in a small turbulent contribution comparable to the snow phase laminar viscosity, and a negligible snow phase effective viscosity compared to the air phase effective viscosity. On the other hand, a density ratio of order $O(1)$ for suspended sediment in water results in a large turbulent contribution that dominates the

sediment phase laminar viscosity. The sediment phase effective viscosity becomes comparable to the water phase effective viscosity. Therefore, turbulent drag seems to be the only relevant dispersion mechanism for aeolian transport of solid particles, while particle turbulence was found to be equally relevant for hydrological transport of solid particles.

Based on the findings summarised above it is recommended to implement a polydisperse capability in the Eulerian-Eulerian formulation to be able to account for polydispersity in a native way, by allowing more than one dispersed phase with one particle diameter. This would require accounting for the interaction between particles explicitly in the creeping layer and the bed, as opposed to modelling it to zeroth order using the threshold shear stress. The particle viscosity treatment in the bed according to equation 2.35 needs to be revisited as well. It could be preferable to model the snow shear stress in the bed using a structural dynamics approach since snow viscous behaviour in the bed is limited to very low rates of strain [162, 163]. Moreover, an extra continuous phase would be required to be able to account for free surfaces such as water-air interfaces in sediment transport. Further validation is also desirable for flows around obstacles under highly accelerating and decelerating conditions. The proposed corrections to the Carrier-Cashwell and the Kazhikov-Smagulov particle viscosity models are promising, but should be further verified on a larger parameter space.

References

[1] R.A. Bagnold. *The physics of blown sand and desert dunes.* London, Methuen, 1941.

[2] D. Kobayashi. Studies of snow transport in low-level drifting snow. *Contributions from the Institute of Low Temperature Science*, A 24:1–58, 1972.

[3] NBC. *National Building Code of Canada*, volume 1. NRC, 2010.

[4] ASCE. *ASCE 7-10 - Minimum Design Loads for Buildings and Other Structures.* ASCE, 2010.

[5] B.E. Goodison. Compatibility of canadian snowfall and snow cover data. *Agricultural and Forest Meteorology*, 17(4):893–900, 1981.

[6] C.S. Benson, M. Sturm. Structure and wind transport of seasonal snow on the arctic slope of alaska. In *Symposium on Snow and Snow-Related Problems*, pages 279–283, Nagaoka, Japan, September 14-18 1993.

[7] J.W. Pomeroy, D.M. Gray, P.G. Landline. The prairie blowing snow model: characteristics, validation, operation. *Journal of Hydrology*, 144:165–192, 1993.

[8] J.W. Pomeroy, P. Marsh, D.M. Gray. Application of a distributed blowing snow model to the arctic. *Hydrological Processes*, 11:1451–1464, 1997.

[9] T. Uematsu, T. Nakata, K. Takeuchi, Y. Arisawa, Y. Kaneda. Three-dimensional numerical simulation of snowdrift. *Cold Regions Science and Technology*, 20:65–73, 1991.

[10] M. Naaim, F. Naaim-Bouvet, H. Martinez. Numerical simulation of drifting snow: erosion and deposition model. *Annals of Glaciology*, 26:191–196, 1998.

[11] Y. Tominaga, T. Okaze, A. Mochida. CFD modeling of snowdrift around a building: overview of models and evaluation of a new approach. *Building and Environment*, 46: 899–910, 2011.

[12] B. Bang, A. Nielsen, P.A. Sundsbø, T. Wiik. Computer simulation of wind speed, wind pressure and snow accumulation around buildings (SNOW-SIM). *Energy and Buildings*, 21(3):235–243, 1994. doi: 10.1016/0378-7788(94)90039-6.

[13] J.H.M. Beyers, P.A. Sundsbø, T.M. Harms. Numerical simulation of three-dimensional transient flow around a cube. *Journal of Wind Engineering and Industrial Aerodynamics*, 92:725–747, 2004.

[14] J.H.M. Beyers, B. Waechter. Modeling transient snowdrift development around complex three-dimensional structures. *Journal of Wind Engineering and Industrial Aerodynamics*, 96:1603–1615, 2008.

[15] I. Moore. *Numerical modeling of blowing snow around buildings*. PhD dissertation, Department of Mathematical Studies, University of Leeds, 1995.

[16] P.A. Sundsbø. Numerical simulations of wind deflection fins to control snow accumulation in building steps. *Journal of Wind Engineering and Industrial Aerodynamics*, 74-76:543–552, 1998.

[17] T.K. Thiis. A comparison of numerical simulations and full-scale measurements of snowdrifts around buildings. *Wind and Structures*, 3(2):73–81, 2000.

[18] C.D. Groot Zwaaftink, M. Diebold, S. Horender, J. Overney, G. Lieberherr, M. Parlange, M. Lehning. Modelling small-scale drifting snow with a Lagrangian stochastic model based on Large-Eddy Simulations. *Boundary-Layer Meteorology*, 153(1):117–139, 2014. doi: 10.1007/s10546-014-9934-2.

[19] E. Maldonado, M.W. Roth. Direct two–phase numerical simulation of snowdrift remediation using three–dimensional deflection fins. *Journal of Applied Fluid Mechanics*, 5(3):71–78, 2012.

[20] L. Zhao, Z. Yu, F. Zhu, X. Qi, S. Zhao. CFD-DEM modeling of snowdrifts on stepped flat roofs. *Wind and Structures*, 23(6):523–542, 2016.

[21] B.E. Lee, J.Y. Tu, C.A.J. Fletcher. On numerical modeling of particle-wall impaction in relation to erosion prediction: Eulerian versus Lagrangian method. *Wear*, 252:179–188, 2002.

[22] P. Gauer. Numerical modeling of blowing and drifting snow. *Journal of Glaciology*, 47(156):97–110, 2001.

[23] T. Uematsu. Numerical study on snow transport and drift formation. In *Symposium on Snow and Snow-Related Problems*, pages 135–141, Nagaoka, Japan, September 14-18 1992.

[24] T. Sato, T. Uematsu, T. Nakata, Y. Kaneda. Three dimensional numerical simulation of snowdrift. *Journal of Wind Engineering and Industrial Aerodynamics*, 46 & 47:741–746, 1993.

[25] Y. Tominaga, A. Mochida. CFD prediction of flowfield and snowdrift around a building complex in a snowy region. *Journal of Wind Engineering and Industrial Aerodynamics*, 81:273–282, 1999.

[26] Y. Tominaga, A. Mochida, H. Yoshino, T. Shida, T. Okaze. CFD prediction of snowdrift around a cubic building model. In *The Fourth International Symposium on Computational Wind Engineering (CWE2006)*, Yokohama, Japan, 2006.

[27] J.W. Pomeroy, D.M. Gray. Saltation of snow. *Water Resources Research*, 26(7): 1583–1594, 1990.

[28] T. Okaze, A. Mochida, Y. Tominaga, M. Nemoto, Y. Ito, T. Shida. Modeling of drifting snow development in a boundary layer and its effect on windfield. In *The Sixth Snow Engineering Conference*, Whistler, B.C., Canada, June 1-5 2008.

[29] Y. Tominaga, A. Mochida, T. Okaze, T. Sato, M. Nemoto, H. Motoyoshi, S. Nakai, T. Uematsu, M. Otsuki. Development of system for predicting snow distribution in built-up environment. In *The Fifth International Symposium on Computational Wind Engineering (CWE2010)*, Chapel Hill, North Carolina, USA, 2010.

[30] S. Oikawa, T. Tomabechi. Formation processes of the deposition and erosion of snow around a model building. *Seppyo*, 65(2):207–2018, 2003.

[31] R. Bintanja. Snowdrift suspension and atmospheric turbulence. Part I: Theoretical background and model description. *Boundary-Layer Meteorology*, 95:343–368, 2000.

[32] J.W. Pomeroy, D.H. Male. Steady-state suspension of snow. *Journal of Hydrology*, 136:275–301, 1992.

[33] R.S. Anderson, P.K. Haff. Simulation of eolian saltation. *Science*, 241:820–823, 1988.

[34] P.A. Durbin. On the k-3 stagnation point anomaly. *Int. J. Heat and Fluid Flow*, 17: 89–90, 1996.

[35] Y. Tominaga, A. Mochida, S. Murakami, S. Sawaki. Comparison of various revised $k - \epsilon$ models and LES applied to flow around a high-rise building model with 1:1:2 shape placed within the surface boundary layer. *Journal of Wind Engineering and Industrial Aerodynamics*, 96:389–411, 2008.

[36] S. Oikawa, T. Tomabechi, T. Ishihara. One-day observations of snowdrifts around a model cube. *Journal of Snow Engineering of Japan*, 15(4):3–11, 1999.

[37] J. Nakashizu, K. Hosokawa, S. Oikawa, T. Tomabechi. Experimental research about the snowdrift formation process near the building. *Summaries of technical papers of Annual Meeting Architectural Institute of Japan*, B-1, Structures I:69–70, 2003.

[38] C.W. Hirt, B.D. Nichols. Volume of Fluid (VOF) method for the dynamics of free boundaries. *J. Comput. Phys.*, 9:201–225, 1981.

[39] J.A.C. Humphrey. Fundamentals of fluid motion in erosion by solid particle impact. *International Journal of Heat and Fluid Flow*, 11(3), 1990. doi: 10.1016/0142-727x(90) 90036-b.

[40] W.F. Adler. Assessment of the state of knowledge pertaining to solid particle erosion. Final Report CR79-680, US Army Research Office, 1979.

[41] P.R. Owen. Saltation of uniform grains in air. *Journal of Fluid Mechanics*, 20(2): 225–242, 1964.

[42] J.H.M. Beyers, T.M. Harms. Outdoors modelling of snowdrift at SANAE IV research station, Antarctica. *Journal of Wind Engineering and Industrial Aerodynamics*, 91: 551–569, 2003.

[43] J.H.M. Beyers. *Numerical modeling of the snowdrift characteristics surrounding the SANAE IV research station.* PhD dissertation, Department of Mechanical Engineering, University of Stellenbosch, 2004.

[44] W. Schmidt. Der massenaustausch in freier luft und verwandte erscheinungen. *Probleme der Kosmischen Physik*, 7, 1925.

[45] L. Prandtl. Bericht über untersuchingen zur ausgebildeten turbulentz. *Z. Ang. Math. Mech.*, 5:136–137, 1925.

[46] E.A. Toorman. Sediment-laden turbulent flow: a review of theories and models. Technical Report HYD/ET/00/COSINUS1, Hydraulics Laboratory, KU Leuven, 2000.

[47] R.H. Rouse. Modern conceptions of the mechanics of fluid turbulence. *Trans. ASCE*, 102:463–543, 1937.

[48] R.H. Rouse. Experiments on the mechanics of sediment suspension. In *Proceedings of the Fifth International Congress for Applied Mechanics*, pages 550–554. John Wiley & Sons, New York, 1938.

[49] V.A. Vanoni. Transportation of suspended sediment by water. *Transactions of the ASCE*, 109:67–133, 1944.

[50] J.R. Ni. A generalized formula on the vertical distribution of suspended sediment concentration. In *Proceedings of the 4th International Symposium on River Sedimentation*, pages 603–610, Beijing, China, 1989. China Ocean Press.

[51] J.R. Ni, G.Q. Wang. Vertical sediment distribution. *Journal of Hydraulic Engineering*, 117(9):1184–1194, 1991. doi: 10.1061/(asce)0733-9429(1991)117:9(1184).

[52] J.F. Richardson, W.N. Zaki. Sedimentation and fluidisation: Part I. *Transactions of the Institution of Chemical Engineers*, 32:S82–S100, 1954. doi: 10.1016/s0263-8762(97)80006-8.

[53] M. Umeyama, F. Gerritsen. Velocity distribution in uniform sediment laden flow. *Journal of Hydraulic Engineering*, 118(2):229–245, 1992. doi: 10.1061/(asce)0733-9429(1992)118:2(229).

[54] M. Umeyama. Vertical distribution of suspended sediment in uniform open channel flow. *Journal of Hydraulic Engineering*, 118(6):936–941, 1992. doi: 10.1061/(asce)0733-9429(1992)118:6(936).

[55] H.A. Einstein, N. Chien. Effects of heavy sediment concentration near the bed on velocity and sediment distribution. *M.R.D. Sediment Series*, 8, 1955.

[56] E.M. Laursen. A concentration distribution formula from the revised theory of prandtl mixing length. In *Proceedings of the 1st International Symposium on River Sedimentation*, volume 1, Beijing, China, 1982. Guanghua Press.

[57] S. Tanaka, S. Sugimoto. On the distribution of suspended sediment in experimental flume flow. *Memoirs of the Faculty of Engineering, Kobe University*, 5:337–349, 1958.

[58] G.N. Barenblatt. *The suspended sediment movement in turbulent flow*. Water Conservancy Press, Beijing, China, 1956.

[59] J.N. Hunt. The turbulent transport of suspended sediment in open channels. *Proc. Royal Soc. of London, Ser. A*, 224:322–335, 1954.

[60] B.A. Christensen. Incipient motion on cohesionless channel banks. In H.S. Shen, editor, *Sedimentation, a Symp. to honor H.A. Einstein*, volume 4, pages 1–22, Colorado State University, Fort Collins, Colorado, 1972.

[61] J.C. Willis. Distributions of flow velocity and suspended sediment. In S.Y. Wang, editor, *Advances in Hydro-Science and Engineering, Proc. of the 1st ICHE*, pages 664–671, 1986.

[62] V.A. Vanoni. *Sedimentation Engineering*. ASCE, 2006.

[63] B.P. Greimann, M. Muste, F.M. Holly. Two-phase formulation of suspended sediment transport. *J. Hydraulic Res. IAHR 37*, 4:479–500, 1999.

[64] X. Wang, N. Qian. Velocity profiles of sediment laden flow. *International Journal of Sediment Research*, 7(1):27–58, 1997.

[65] W.C. Taggart, C.A. Yermoli, S. Montes, A.T. Ippen. Effects of sediment size and gradation on concentration profiles in turbulent flow. Report 152, Ralph M. Parsons Lab for Water Res. and Hydrodynamics, Dept. of Civil Eng., MIT, 1972.

[66] E. Deutsch, O. Simonin. Large Eddy Simulation applied to the motion of particles in stationary homogeneous fluid turbulence. *ASME FED*, 110:35–42, 1991.

[67] J. He, O. Simonin. Non-equilibrium prediction of the particle-phase stress tensor in vertical pneumatic conveying. *ASME FED*, 166:253–263, 1993.

[68] N. Kobayashi, S.N. Seo. Fluid and sediment interaction over a plane bed. *Journal of Hydraulic Engineering*, 111(6):903–921, 1985. doi: 10.1061/(asce)0733-9429(1985)111:6(903).

[69] Z.X. Cao, L.Y. Wei, J.H. Xie. Sediment-laden flow in open channels from two-phase flow viewpoint. *Journal of Hydraulic Engineering*, 10:725–735, 1995.

[70] J. Jiang, A.W-K. Law, N-S. Cheng. Two-phase modeling of suspended sediment distribution in open channel flows. *Journal of Hydraulic Research*, 42(3):273–281, 2004. doi: 10.1080/00221686.2004.9641195.

[71] D.Y. Liu. *Fluid Dynamics of Two-Phase Systems*. Junior Edu. Pub., Beijing, China, 1993.

[72] D.Y. Liu, K. Anders, A. Frohn. Drag coefficients of single droplets moving in an infinite droplet chain on the axis of a tube. *International Journal of Multiphase Flow*, 14(2):217–232, 1988. doi: 10.1016/0301-9322(88)90007-9.

[73] I. Nezu, W. Rodi. Open-channel flow measurements with a laser doppler anemometer. *Journal of Hydraulic Engineering*, 112(5):335–355, 1986. doi: 10.1061/(ASCE)0733-9429(1986)112:5(335).

[74] M. Cellino. *Experimental Study of Suspension Flow in Open Channels*. PhD dissertation, Laboratoire de Recherches Hydraulique, EPFL, Lausanne, Switzerland, 1998.

[75] M. Muste, V.C. Patel. Velocity profiles for particles and liquid in open-channel flow with suspended sediment. *Journal of Hydraulic Engineering*, 123(9):742–751, 1997. doi: 10.1061/(ASCE)0733-9429(1997)123:9(742).

[76] L.C. Van Rijn. Mathematical modeling of suspended sediment in nonuniform flows. *Journal of Hydraulic Engineering*, 112(6):433–455, 1986. doi: 10.1061/(asce)0733-9429(1986)112:6(433).

[77] L.C. Van Rijn. *Mathematical Modelling of Morphological Processes in the Case of Suspended Sediment Transport*. PhD dissertation, Delft Hydraulics Laboratory, TU Delft, Delft, The Netherlands, 1987.

[78] D. Coles. The law of the wake in the turbulent boundary layer. *Journal of Fluid Mechanics*, 1(02):191–, 1956. doi: 10.1017/s0022112056000135.

[79] P.J.M. Kerssens. Morphological computations for suspended sediment transport. Report S 78-VI, Delft Hydraulics Laboratory, Delft, the Netherlands, 1977.

[80] L.C. Van Rijn. Mathematical models for sediment concentration profiles in steady flow. In W. Bechteler, editor, *Euromech 192: Transport of Suspended Solids in Open Channels*, pages 49–68, 1985.

[81] Z.B. Wang, J.S. Ribberink. The validity of a depth-integrated model for suspended sediment transport. *J. Hydr. Res.*, 24(1):53–66, 1986.

[82] L.C. Van Rijn. Computation of siltation in dredged trenches. Report 1267-V, Delft Hydraulics Laboratory, Delft, the Netherlands, 1980.

[83] L.C. Van Rijn. Numerical model for non-steady suspended sediment transport. Report 975-II, Delft Hydraulics Laboratory, Delft, the Netherlands, 1977.

[84] A.O. Demuren, W. Rodi. Calculation of flow and pollutant dispersion in meandering channels. *Journal of Fluid Mechanics*, 172(1):63, 1986. doi: 10.1017/S0022112086001659.

[85] A.K. Rastogi, W. Rodi. Predictions of heat and mass transfer in open channels. *Journal of the Hydraulics Division-ASCE*, 104(3):397–420, 1978.

[86] W. Rodi, R. Pavlovic, S.K. Srivatsa. *Predictions of heat and mass transfer in open channels*, pages 63–111. Academic, 1981.

[87] M.A. Leschziner, W. Rodi. Calculation of annular and twin parallel jets using various discretization schemes and turbulence-model variations. *Journal of Fluids Engineering*, 103(2):352–, 1981. doi: 10.1115/1.3241745.

[88] Y.C. Chang. *Lateral mixing in meandering channels*. PhD dissertation, University of Iowa, USA, 1971.

[89] S. Fukuoka. *Longitudinal dispersion in sinuous channels*. PhD dissertation, University of Iowa, USA, 1971.

[90] A.O. Demuren. Development of a mathematical model for sediment transport in meandering rivers. Technical Report 693, Inst. for Hydro-mechanics, University of Karlsruhe, Karlsruhe, Germany, 1991.

[91] A.J. Odgaard, M.A. Bergs. Flow processes in a curved alluvial channel. *Water Resources Research*, 24(1):45–56, 1988. doi: 10.1029/wr024i001p00045.

[92] M.O. Green, G. Coco. Review of wave-driven sediment resuspension and transport in estuaries. *Reviews of Geophysics*, 52(1):77–117, 2014. doi: 10.1002/2013rg000437.

[93] F.E. Anderson. Resuspension of estuarine sediments by small amplitude waves. *Journal of Sedimentary Research*, 42(3):602, 1972. doi: 10.1306/74D725D6-2B21-11D7-8648000102C1865D.

[94] K.R. Dyer, M.C. Christie, N. Feates, M.J. Fennessy, M. Pejrup, W. van der Lee. An investigation into processes influencing the morphodynamics of an intertidal mudflat, the Dollard estuary, the Netherlands: I. Hydrodynamics and suspended sediment. *Estuarine, Coastal and Shelf Science*, 50(5):607–625, 2000. doi: 10.1006/ecss.1999.0596.

[95] M.O. Green. Very small waves and associated sediment resuspension on an estuarine intertidal flat. *Estuarine, Coastal and Shelf Science*, 93(4):449–459, 2011. doi: 10.1016/j.ecss.2011.05.021.

[96] R.J Uncles, J.A Stephens. Observations of currents, salinity, turbidity and intertidal mudflat characteristics and properties in the Tavy estuary, UK. *Continental Shelf Research*, 20(12-13):0–1549, 2000. doi: 10.1016/s0278-4343(00)00036-4.

[97] L.P. Sanford. Wave-forced resuspension of upper chesapeake bay muds. *Estuaries and Coasts*, 17(1):148–165, 1994. doi: 10.2307/1352564.

[98] M.C. Christie, K.R. Dyer, P. Turner. Sediment flux and bed level measurements from a macro tidal mudflat. *Estuarine, Coastal and Shelf Science*, 49(5):667–688, 1999. doi: 10.1006/ecss.1999.0525.

[99] M.O. Green, K.P. Black C.L. Amos. Control of estuarine sediment dynamics by interactions between currents and waves at several scales. *Marine Geology*, 144(1-3):97–116, 1997. doi: 10.1016/s0025-3227(97)00065-0.

[100] M.C. Christie, K.R. Dyer. Measurements of the turbid tidal edge over the Skeffling mudflats. *Geological Society London Special Publications*, 139(1):45–55, 1998. doi: 10.1144/GSL.SP.1998.139.01.04.

[101] W. Wu, W. Rodi, T. Wenka. 3D numerical modeling of flow and sediment transport in open channels. *Journal of Hydraulic Engineering*, 126(1):4–15, 2000.

[102] L.C. Van Rijn. Entrainment of fine sediment particles; development of concentration profiles in a steady, uniform flow without initial sediment load. Report M1531, Part II, Delft Hydraulics Laboratory, Delft, the Netherlands, 1981.

[103] J. Zeng, G. Constantinescu, L. Weber. A 3d non-hydrostatic model to predict flow and sediment transport in loose-bed channel bends. *Journal of Hydraulic Research*, 46(3):356–372, 2008. doi: 10.3826/jhr.2008.3328.

[104] J.E. Richardson, V.G. Panchang. Three-dimensional simulation of scour-inducing flow at bridge piers. *Journal of Hydraulic Engineering*, 124(5):530–540, 1998. doi: 10.1061/(ASCE)0733-9429(1998)124:5(530).

[105] X. Liu, M.H. García. Three-dimensional numerical model with free water surface and mesh deformation for local sediment scour. *Journal of Waterway Port Coastal and Ocean Engineering*, 134(4):203–217, 2008. doi: 10.1061/(ASCE)0733-950X(2008)134:4(203).

[106] A.M.A. Sattar, H. Jasak, V. Skuric. Three dimensional modeling of free surface flow and sediment transport with bed deformation using automatic mesh motion. *Environmental Modelling & Software*, 97:303–317, 2017. doi: 10.1016/j.envsoft.2017.08.005.

[107] W. Wu. *Computational River Dynamics*. Taylor and Francis, Leiden, the Netherlands, 2007.

[108] O. Ubbink, R.I. Issa. A method for capturing sharp fluid interfaces on arbitrary meshes. *Journal of Computational Physics*, 153(1):26–50, 1999. doi: 10.1006/jcph.1999.6276.

[109] ESI Group. *OpenFOAM Documentation, Extended Code Guide*, 2018.

[110] J. Roenby, H. Bredmose, H. Jasak. A computational method for sharp interface advection. *Royal Society Open Science*, 3(11):160405–, 2016. doi: 10.1098/rsos.160405.

[111] H. Jasak, V. Vukčević, D. Christ. Rapid free surface simulation for steady-state hull resistance with FVM using OpenFOAM. In *Proceedings of the 30th Symposium on Naval Hydrodynamics*, Hobart, Tasmania, Australia, 2–7 November 2014.

[112] L.C. Van Rijn. Sediment transport, Part II: suspended load transport. *J. Hydr. Engrg.*, 110(11):1613–1641, 1984.

[113] H.W. Fang, W. Rodi. Three-dimensional calculations of flow and suspended sediment transport in the neighborhood of the dam for the Three Gorges Project (TGP) reservoir in the Yangtze river. *Journal of Hydraulic Research*, 41(4):379–394, 2003. doi: 10.1080/00221680309499983.

[114] B. Brørs. Numerical modeling of flow and scour at pipelines. *Journal of Hydraulic Engineering*, 125(5):511–523, 1999. doi: 10.1061/(ASCE)0733-9429(1999)125:5(511).

[115] F. Engelund, J. Fredsoe. A sediment transport model for straight alluvial channels. *Nord Hydrol*, 7:293–306, 1976.

[116] A. Shields, W.P. Ott, J.C. van Uchelen. Application of similarity principles and turbulence research to bed-load movement report. *Mitteilunger der Preussischen Versuchsanstalt für Wasserbau und Schiffbau*, 26, 1936.

[117] A. Einstein. Eine neue bestimmung der moleküldimensionen. *Annalen der Physik*, 324(2):289–306, 1906. doi: 10.1002/andp.19063240204.

[118] A. Einstein. Berichtigung zu meiner arbeit: "eine neue bestimmung der moleküldimensionen". *Annalen der Physik*, 339(3):591–592, 1911. doi: 10.1002/andp.19113390313.

[119] H.C. Brinkman. The viscosity of concentrated suspensions and solutions. *The Journal of Chemical Physics*, 20(4):571–0, 1952. doi: 10.1063/1.1700493.

[120] R. Roscoe. The viscosity of suspensions of rigid spheres. *British Journal of Applied Physics*, 3(8):267–269, 1952. doi: 10.1088/0508-3443/3/8/306.

[121] M. Ishii. One-dimensional drift-flux model and constitutive equations for relative motion between phases in various two-phase flow regimes. Technical Report ANL-77-47, Argonne National Laboratory, Illinois, USA, 1977.

[122] A.L. Graham. On the viscosity of suspensions of solid spheres. *Flow, Turbulence and Combustion*, 37(3-4):275–286, 1981. doi: 10.1007/bf00951252.

[123] V. Vand. Viscosity of solutions and suspensions. I. Theory. *Journal of Physical Chemistry*, 52(2):277–299, 1948. doi: 10.1021/j150458a001.

[124] G.F. Carrier, E.D. Cashwell. Unpublished report. Technical report, Los Alamos National Lab, New Mexico, USA, 1956.

[125] J.D. Murray. On the mathematics of fluidization part 1. fundamental equations and wave propagation. *Journal of Fluid Mechanics*, 21(03):465–, 1965. doi: 10.1017/S0022112065000277.

[126] A. Kazhikov, Sh. Smagulov. The correctness of boundary value problems in a diffusion problem of an homogeneous fluid. *Sov. Phys. Dokl.*, 22:249–252, 1977.

[127] D. Dutykh, C. Acary-Robert, D. Bresch. Mathematical modeling of powder-snow avalanche flows. *Studies in Applied Mathematics*, 127(1):38–66, 2011. doi: 10.1111/j.1467-9590.2010.00511.x.

[128] H. Teufelsbauer. A two-dimensional snow creep model for alpine terrain. *Natural Hazards*, 56:481–497, 2011.

[129] F. Moukalled, L. Mangani, M. Darwish. *The Finite Volume Method in Computational Fluid Dynamics*. Springer International Publishing, 2016. ISBN 978-3-319-16873-9,978-3-319-16874-6. doi: 10.1007/978-3-319-16874-6.

[130] A.D. Gosman, R. Issa, C. Lekakou, S. Politis, M.K. Looney. Multidimensional modeling of turbulent two-phase flows in stirred vessels. *AIChE Journal*, 38(12): 1946–1956, 1992.

[131] M. Ishii. *Thermo-fluid Dynamic Theory of Two-phase Flow*. Eyrolles, 1975.

[132] P. Gauer. *Blowing and Drifting Snow in Alpine Terrain: A Physically-Based Numerical Model and Related Field Measurements*. PhD dissertation, ETH Zurich, 1999.

[133] D. Gidaspow. Hydrodynamics of fluidization and heat transfer: supercomputer modelling. *Appl. Mech. Rev.*, 39:1–22, 1986.

[134] L. Schiller, Z. Naumann. A drag coefficient correlation. *Z. Ver. Deutsch. Ing.*, 77, 1935.

[135] H. Enwald, E. Peirano, A.-E. Almstedt. Eulerian two-phase flow theory applied to fluidization. *Int. J. of Multiphase Flow*, 22:21–66, 1996.

[136] H.G. Weller. Derivation, modelling and solution of the conditionally averaged two-phase flow equations. Report TR/HGW/02, OpenCFD Ltd, 2005.

[137] H. Rusche. *Computational fluid dynamics of dispersed two-phase flows at high phase fractions*. PhD dissertation, Department of Mechanical Engineering, Imperial College of Science, Technology & Medicine, London, UK, 2002.

[138] B.E. Launder, D.B. Spalding. The numerical computation of turbulent flows. *Computer Methods in Applied Mechanics and Engineering*, 3(2):269–289, 1974.

[139] R.I. Issa, P.J. Oliveira. Numerical prediction of turbulent dispersion in two-phase jet flows. In G.P. Celata, R.K. Shah, editors, *Two-Phase Flow Modelling and Experimentation*, 1995.

[140] R.J. Kind. *Handbook of Snow, Principles, Processes, Management and Use*, chapter Snowdrifting, pages 338–359. Pergamon Press, 1981.

[141] T. Okaze, A. Mochida, Y. Tominaga, M. Nemoto, T. Sato, Y.Sasaki, K. Ichinohe. Wind tunnel investigation of drifting snow development in a boundary layer. *J. Wind Eng. Ind. Aerodyn.*, 104-106:532–539, 2012.

[142] C. McKenna Neuman, W. G. Nickling. Momentum extraction with saltation: implications for experimental evaluation of wind profile parameters. *Boundary-Layer Meteorology*, 68(1-2):35–50, 1994.

[143] C. McKenna Neuman, M. Maljaars. Wind tunnel measurement of boundary- layer response to sediment transport. *Boundary-Layer Meteorology*, 84(1):67–83, 1997.

[144] K.R. Rasmussen, H.E. Mikkelsen. On the efficiency of vertical array aeolian field traps. *Sedimentology*, 45(4):789–800, 1998. doi: 10.1046/j.1365-3091.1998.00179.x.

[145] P.J. Spies, I.K. McEwan, G.R. Butterfield. On wind velocity profile measurements taken in wind tunnels with saltating grains. *Sedimentology*, 42(3):515–521, 1995. doi: 10.1111/j.1365-3091.1995.tb00387.x.

[146] M. Nemoto, K. Nishimura. Numerical simulation of snow saltation and suspension in a turbulent boundary layer. *Journal of Geophysical Research*, 109(D18206), 2004.

[147] R.I. Issa. Solution of the implicitly discretised fluid flow equations by operator-splitting. *Journal of Computational Physics*, 62:40–65, 1985.

[148] A.J. Clifton. *Wind Tunnel Investigations of Boundary Layer Conditions Before and During Snow Drift*. PhD thesis, Swiss Federal Institute of Technology Zurich, Zurich, Switzerland, 2007.

[149] W.F. Budd. The drifting of nonuniform snow particles. In M.J. Rubin, editor, *Studies in Antarctic meteorology*. American Geophysical Union, 1966.

[150] R.A. Schmidt. Vertical profiles of wind speed, snow concentration and humidity in blowing snow. *Boundary-Layer Meteorology*, 23(2):223–246, 1982.

[151] C.T. Crowe, J.D. Schwarzkopf, M. Sommerfeld, Y. Tsuji. *Multiphase flows with droplets and particles*. CRC Press, 2nd edition edition, 2011.

[152] W.C. Strahle. Stagnation point flows with freestream turbulence – the matching condition. *AIAAJ*, 23:1822–1824, 1985.

[153] B.E. Launder, M. Kato. Modeling flow-induced oscillations in turbulent flow around square cylinder. In *ASME Fluid Eng. Conference*, page 20, 1993.

[154] A. Behzadi, R.I. Issa, H. Rusche. Modelling of dispersed bubble and droplet flow at high phase fractions. *Chemical Engineering Science*, 59:759–770, 2004.

[155] T. Okaze, Y. Takano, A. Mochida, Y. Tominaga. Development of a new $k - \epsilon$ model to reproduce the aerodynamic effects of snow particles on a flow field. *J. Wind Eng. Ind. Aerodyn.*, 144:118–124, 2015.

[156] T. Mochida, I.Y.F. Lun. Prediction of wind environment and thermal comfort at pedestrian level in urban area. *Journal of Wind Engineering and Industrial Aerodynamics*, 96:1498–1527, 2008.

[157] P. Durbin. Separated flow computations with the k-epsilon-v2 model. *AIAA Journal*, 33:659–664, 1995.

[158] F.R. Menter. Zonal two equation k-w turbulence models for aerodynamic flows. In *Proceedings of the American Institute of Aeronautics and Astronautics (AIAA) 23rd Fluid Dynamics, Plasmadynamics, and Lasers Conference*, Orlando, FL, USA, July 1993. doi: 10.2514/6.1993-2906.

[159] F.R. Menter. Two-equation eddy-viscosity turbulence models for engineering applications. *AIAA Journal*, 32(8):1598–1605, 1994. doi: 10.2514/3.12149.

[160] E. Celik, D. Rockwell. Shear layer oscillation along a perforated surface: A self-excited large-scale instability. *Physics of Fluids*, 14(12):4444–4447, 2002. doi: 10.1063/1.1519531.

[161] C. Ozalp, A. Pinarbasi, D. Rockwell. Self-excited oscillations of turbulent inflow along a perforated plate. *Journal of Fluids and Structures*, 17(7):955–970, 2003. doi: 10.1016/s0889-9746(03)00045-8.

[162] M. Mellor. A review of basic snow mechanics. In *Proceedings of Grindelwald symposium*, Grindelwald, Switzerland, 1975. IAHS Publ.

[163] M. Mellor. Engineering properties of snow. *Journal of Glaciology*, 19(81):15–66, 1977. doi: 10.3189/S002214300002921X.

Curriculum Vitae

Ziad Boutanios studied mechanical engineering at Concordia University in Montreal, Canada, where he completed his bachelor and master of applied science degrees. He is an active CFD and High Performance Computing (HPC) consultant. He is well versed in several programming languages, and is skilled in both Finite Element and Finite Volume methods. His research and professional interests include aerodynamics, aero-icing, drifting snow, multiphase flows, and wind engineering, to name only a few. Ziad is a polyglot, with an extensive multi-cultural background.

Declaration

Parts of the work presented in this thesis have been published in articles listed below.

Selected Publications

[1] Z. Boutanios, H. Jasak. Viscous treatment of the snow phase in Eulerian-Eulerian simulations of drifting snow. In *The 14th International Conference on Wind Engineering*, Porto Alegre, Brazil, June 21–26 2015.

[2] Z. Boutanios, H. Jasak. Improvements of the viscous treatment of the snow phase in two-way coupled simulations of drifting snow Eulerian-Eulerian. In *The 8th International Conference on Snow Engineering*, Nantes, France, June 14–16 2016.

[3] Z. Boutanios, H. Jasak. Two-way coupled eulerian-eulerian simulations of a viscous drifting snow phase with turbulent drag. In J. Nóbrega, H. Jasak, editors, *OpenFOAM$^®$ – Selected papers of the 11th workshop*, Guimarães, Portugal, 26–30 June 2016. Springer International Publishing AG.

[4] Z. Boutanios, H. Jasak. Two-way coupled Eulerian-Eulerian simulations of drifting snow with viscous treatment of the snow phase. *Journal of Wind Engineering and Industrial Aerodynamics*, 169:67–76, 2017. doi: 10.1016/j.jweia.2017.07.006.

[5] Z. Boutanios, H. Jasak. Two-way coupled Euler-Euler simulations of particle-laden flows. In *The 7th International Conference on Snow Engineering*, Seoul, South-Korea, June 18–22 2018.